

Marikken L. Sundnes

Some Fluorescent Ligands for Studying Amyloid Uptake in Human Cell Models

Master's thesis in Applied Physics and Mathematics

Supervisor: Mikael Lindgren

Co-supervisor: Priyanka Swaminathan, Per Hammarström (LiU)

June 2023

Marikken L. Sundnes

Some Fluorescent Ligands for Studying Amyloid Uptake in Human Cell Models

Master's thesis in Applied Physics and Mathematics

Supervisor: Mikael Lindgren

Co-supervisor: Priyanka Swaminathan, Per Hammarström (LiU)

June 2023

Norwegian University of Science and Technology

Faculty of Natural Sciences

Department of Physics



Norwegian University of
Science and Technology

Preface

This thesis is the final work and completion of a degree of Master of Science in Applied Physics and Mathematics at the Norwegian University of Science and Technology in spring 2023. The thesis is produced over 20 weeks, from January to June 2023, and the workload corresponds to 30 credits. It also builds on the work performed by the author in the preparatory specialization project in fall 2022.

First of all, I would like to give a big thank you to my supervisor Mikael Lindgren for being immensely supportive and always going above and beyond his duties as supervisor to help my thesis become as great as possible. I am very grateful to his positive and encouraging attitude that kept the stress at bay even with a closely impending deadline.

I am also very thankful to my co-supervisor, PhD student Priyanka Swaminathan, who patiently guided me in the cell culturing and preparation of cells for experiments, collaborated with me on the CLSM and FLIM experiments, as well as cultured one of the cell lines studied in this thesis. She has been a great support and discussion partner throughout the semester.

I would also like to thank Odrun Arna Gederaas, for giving advice on the cell model experiments, being available for our weekly discussions throughout the semester and for guiding me with regards to scientific writing. Astrid Bjørkøy was also a great help, through teaching me the use of the FLIM and always being available for fine-tuning the instruments and for resolving any troubles we had. Additionally, I would like to thank Sylvie Lelu, who gave me the training for use of the cell lab, and was available for weekly discussions and advice on the cell experiments throughout the semester.

I am also thankful to Prof. Peter Nilsson and coworkers at the Department of Physics, Chemistry and Biology at Linköping University (LiU) for organizing an engaging and educational research stay at LiU in February 2023, and providing the TTR and fluorescent amyloid ligands studied in this thesis.

Finally, I give a big thank you to the MOSBRI team, who sponsored my research visit to LiU and invited me to present my work at the MOSBRI 2023 Scientific Conference in Zaragoza.

Abstract

There is an increasing prevalence of pathologies characterized by amyloidosis, where proteins misfold into toxic insoluble aggregates known as amyloids. One such misfolding protein is the transport protein Transthyretin (TTR), which can cause pathologies such as cardiac amyloidosis and Familial Amyloid Polyneuropathy (FAP). Early detection of these amyloid aggregates is of great importance for furthering the understanding of the mechanics underlying protein aggregation diseases and developing therapeutic strategies.

Novel fluorescent amyloid probes are investigated as potentially powerful tools for *in vivo* amyloid detection. In this thesis, the binding of several fluorescent amyloid probes to Amyloid Transthyretin (ATTR) is studied with a particular focus on the three amyloid ligands X34, HS335, and HS336. The aim was to characterize the photophysical properties of these amyloid ligands, as well as investigate the ligand binding sites on both native and amyloid Wild-Type Transthyretin (WT-TTR) through binding curve studies and a Fluorescence Resonance Energy Transfer (FRET) study performed with X34.

The photophysical data laid the groundwork for cell model studies, where ATTR was introduced to the HEK-293 and SH-SY5Y cell lines and stained using the amyloid ligands. The interaction of each of the three ligands with ATTR in both cell lines was investigated in detail and compared with the results of the photophysical study.

The two-site model for ligand binding to native WT-TTR was corroborated by the FRET study as well as by the binding curve for X34, with implications for the binding of the amyloid ligands to ATTR in cells due to the difference in affinity for these binding sites. A standard protocol for ATTR transfection was developed, including parameters such as suggested incubation time and optimal ligand and ATTR concentration. The results indicate that the ATTR fibrils successfully entered the cells using this protocol, as there were significant changes in either emission, fluorescence lifetime, or both for the amyloid ligands upon the addition of ATTR to the cells. It is assumed that this protocol can be generalized for use with other types of amyloid proteins, and will be of use for future studies on amyloid interaction with human cell lines.

Sammendrag

Det er økende forekomst av patologier kjennetegnet av amyloidose, der proteiner feilfoldes til giftige, uløselige aggregater kjent som amyloider. Et slikt misfoldende protein er transportproteinet Transthyretin (TTR), som kan forårsake patologier som hjerteamyloidose og Familiær Amyloid Polyneuropati (FAP). Tidlig påvisning av disse amyloid-aggregatene er av stor betydning for å fremme forståelsen av mekanikken bak protein-aggregeringssykdommer og for å utvikle terapeutiske strategier.

Nye fluorescerende amyloid-prober blir undersøkt som potensielt kraftige verktøy for *in vivo* amyloid-deteksjon. I denne oppgaven studeres bindingen av flere fluorescerende amyloid-prober til Amyloid Transthyretin (ATTR) med et spesielt fokus på de tre amyloid-ligandene X34, HS335 og HS336. Målet var å karakterisere de fotofysiske egenskapene til disse amyloid-ligandene, samt undersøke ligand-bindingssetene på både nativ og amyloid Vill-Type Transthyretin (WT-TTR) gjennom bindingskurvestudier og en fluorescens resonansenergioverføring-studie (FRET) utført med X34.

De fotofysiske dataene la grunnlaget for cellemodell-studier, der ATTR ble introdusert til HEK-293- og SH-SY5Y-cellelinjene og farget ved bruk av amyloid-ligandene. Interaksjonen mellom hver av de tre ligandene med ATTR i begge cellelinjene ble undersøkt i detalj og sammenlignet med resultatene fra den fotofysiske studien.

To-setemodellen for ligandbinding til nativ WT-TTR ble støttet av FRET-studien så vel som av bindingskurven for X34, med implikasjoner for bindingen av amyloid-ligandene til ATTR i celler på grunn av forskjellen i affinitet for disse bindingssetene. En standardprotokoll for ATTR-transfeksjon ble utviklet, med foreslåtte parametre som inkubasjonstid og optimale ligand- og ATTR-konsentrasjoner. Resultatene indikerer at ATTR-fibrillene entret cellene ved hjelp av denne protokollen, ettersom det var betydelige endringer i enten emisjon, fluorescens-levetid eller begge for amyloid-ligandene ved tilsetning av ATTR til cellene. Det antas at denne protokollen kan generaliseres for bruk med andre typer amyloid-proteiner, og vil være nyttig for fremtidige studier på amyloid-interaksjon med menneskelige cellelinjer.

Contents

Preface	iii
Abstract	v
Sammendrag	vii
Contents	ix
Acronyms	xiii
1 Introduction	1
1.1 Motivation	1
1.2 Objectives	2
1.3 Approach	2
1.4 Limitations	3
2 Theory and Background	5
2.1 Cell Biology	5
2.1.1 Cell Cultivation	5
2.1.2 SH-SY5Y Cell Line	8
2.1.3 HEK-293 Cell Line	8
2.1.4 Amyloid Fibrils	9
2.1.5 Transthyretin (TTR)	9
2.1.6 Insulin	11
2.1.7 Ligand Binding and Binding Constants	12
2.2 Photophysics	13
2.2.1 Fluorescence	13
2.2.2 Quantum Yield (QY)	14
2.2.3 Fluorescence Lifetime and Time-Correlated Single Photon Counting (TCSPC)	14
2.2.4 Solvent Effects and Quenching	15
2.2.5 Plate Reader Spectroscopy	17
2.2.6 Fluorescence Resonance Energy Transfer (FRET)	17
2.3 Microscopy	18
2.3.1 Fluorescence Lifetime Imaging Microscopy (FLIM)	18
3 Materials and Methods	21
3.1 Fluorescent Amyloid Ligands	21
3.2 Cell Cultivation	23
3.3 Photophysics	24

3.3.1	Quantum Yield (QY)	24
3.3.2	Fluorescence Lifetime	26
3.3.3	Plate Reader Spectroscopy	26
3.3.4	Photophysical Properties of X34 Bound to Insulin and ATTR Fibrils	27
3.3.5	Fluorescence Resonance Energy Transfer (FRET)	27
3.4	Microscopy	28
3.4.1	Sample Preparation for CLSM and FLIM	28
3.4.2	Confocal Laser Scanning Microscopy (CLSM)	31
3.4.3	Fluorescence Lifetime Imaging Microscopy (FLIM)	31
4	Results	33
4.1	Photophysics	33
4.1.1	Tecan Microplate Reader	33
4.1.2	Quantum Yield	37
4.1.3	Fluorescence Lifetime	40
4.1.4	Photophysical Properties of X34 Bound to Insulin and ATTR Fibrils	42
4.1.5	Fluorescence Resonance Energy Transfer (FRET)	43
4.2	Confocal Laser Scanning Microscopy (CLSM)	47
4.2.1	Comparing Insulin and ATTR Fibrils	48
4.2.2	Testing Various Incubation Times for ATTR Fibrils	53
4.2.3	Comparing X34/ATTR in Two Cell Models	56
4.2.4	Comparing HS335/ATTR in Two Cell Models	59
4.2.5	Comparing HS336/ATTR in Two Cell Models	64
5	Discussion	69
5.1	Photophysics	69
5.1.1	Microplate Reader Measurements	69
5.1.2	Absorptive and Emissive Properties	71
5.1.3	Quantum Yield (QY)	73
5.1.4	Fluorescence Lifetime	73
5.1.5	Photophysical Properties of X34 Bound to Insulin and ATTR Fibrils	74
5.1.6	Fluorescence Resonance Energy Transfer (FRET)	74
5.2	Confocal Laser Scanning Microscopy (CLSM)	76
5.2.1	Comparing Insulin and ATTR Fibrils	76
5.2.2	ATTR Incubation Time	77
5.2.3	Comparison of X34/ATTR in Two Cell Models	78
5.2.4	Comparison of HS335/ATTR in Two Cell Models	78
5.2.5	Comparison of HS336/ATTR in Two Cell Models	79
5.3	Discussion of the TTR Two-Site Model in Relation to the Cell Model Studies	80
6	Conclusions and Suggested Future Studies	81
	Bibliography	85
A	Additional Ligands Screened as Potential Amyloid Probes	93

B Spectra for Quantum Yield (QY) Calculations	99
C Additional lifetime decays from TCSPC	101
D Deciding Regions of Interest (ROI) for CLSM and FLIM	103

Acronyms

α -syn α -synuclein.

A β Amyloid- β .

AD Alzheimer's Disease.

APDs Avalanche Photodiodes.

ATTR Amyloid Transthyretin.

BBB Blood-Brain Barrier.

BF Brightfield.

BSL Biosafety Level.

BTB 2,1,3-Benzothiadiazole.

BTDSB Benzothiadiazole Stilbene.

BTBVT Bi-Thiophene-Vinyl-Benzothiazole.

C-153 Coumarin 153.

CHCl₃ Chloroform.

CLSM Confocal Laser Scanning Microscopy.

CM CellMask Deep Red.

CR Congo Red.

DAS6 Decay Analysis Software 6.

DMSO Dimethyl Sulfoxide.

DRAQ5 Deep Red Fluorescing Anthraquinone Nr.5.

EDTA Ethylenediaminetetraacetic Acid.

EMEM Eagle's Minimum Essential Medium.

EtOH Ethanol.

F-12 Nutrient Mixture F-12.

FAC Familial Amyloid Cardiomyopathies.

FAP Familial Amyloid Polyneuropathy.

FBS Fetal Bovine Serum.

FLIM Fluorescence Lifetime Imaging Microscopy.

FRET Fluorescence Resonance Energy Transfer.

h-FTAA Heptamer Formyl Thiophene Acetic Acid.

HEK-293 Human Embryonic Kidney 293.

hx-FTAA Hexamer Formyl Thiophene Acetic Acid.

INS Amyloid Insulin.

IRF Instrument Response Function.

LAS X Leica Application Suite X.

LCO Luminescent Conjugated Oligothiophene.

LiU Linköping University.

LT LysoTracker Deep Red.

MeCN Acetonitrile.

MeOH Methanol.

MOSBRI Molecular-Scale Biophysics Research Infrastructure.

NFTs Neurofibrillary Tangles.

NTNU Norwegian University of Science and Technology.

p-FTAA Pentamer Formyl Thiophene Acetic Acid.

PBS Phosphate-Buffered Saline.

PD Parkinson's disease.

PD-PAM Parkinsons Disease Prodromal Animal Model.

PMT Photomultiplier Tube.

PrOH Propan-1-ol.

ProLinC Protein folding and Ligand Interaction Core.

QY Quantum Yield.

ROI Region of Interest.

SH-SY5Y See explanation in section 2.1.2..

SPAD Single-Photon Avalanche Diodes.

TCSPC Time-Correlated Single Photon Counting.

THF Tetrahydrofuran.

ThT Thioflavin-T.

Trp Tryptophan.

TTR Transthyretin.

Tyr Tyrosine.

WLL White Light Laser.

WT-TTR Wild-Type Transthyretin.

Chapter 1

Introduction

1.1 Motivation

The prevalence of neurodegenerative diseases is steadily growing in line with the rapid aging of the world's population, placing a growing burden on healthcare systems worldwide. Finding causes, treatments and cures for these diseases is crucial, as effective treatments are currently lacking. [1, 2] Many such neurodegenerative diseases are characterized by amyloidosis, where specific misfolded proteins assemble into insoluble aggregates known as amyloids, leading to progressive neuron degeneration. [3] Some examples of neurodegenerative diseases where such abnormal protein aggregation is present is Alzheimer's Disease (AD) and Parkinson's disease (PD), but amyloid aggregation can also cause diseases of peripheral tissue, like in Familial Amyloid Polyneuropathy (FAP). [2] Each of these diseases are linked to the misfolding of specific precursor proteins, Amyloid- β ($A\beta$) and Tau protein for AD, α -synuclein (α -syn) for PD and Transthyretin (TTR) for FAP. [3–5] The development of molecular ligands able to distinguish these misfolded proteins from their native forms is essential to improve diagnostics and facilitate treatment development. [6]

Historically, Thioflavin-T (ThT) and Congo Red have been the golden standard for *in vitro* and *ex vivo* amyloid staining. These probes stain β -pleated sheet secondary protein structures, which are commonly found in amyloid deposits, and are considered general amyloid stains. [7, 8] However, their *in vivo* applications are limited by neither of them being able to cross the Blood-Brain Barrier (BBB). [9, 10] In addition, Congo Red contains highly toxic components and is thus doubly disadvantageous for *in vivo* usage. [7] Development of novel fluorescent ligands is hence necessary to attempt to detect amyloids *in vivo* and be able to diagnose their associated diseases at a much earlier stage than is currently possible.

This project is an initiating part of the EU-wide collaboration called Parkinsons

Disease Prodromal Animal Model (PD-PAM)¹, whose aim is characterization of early indicators of nervous system dysfunction in gut-first and brain-first animal models of PD. [11] For this purpose, novel fluorescent amyloid ligands were developed, targeting protein aggregates having an extensive cross β -pleated sheet conformation and sufficient structural regularity. [6] Many of these ligands are reported to cross the blood-brain barrier and can thus be used for *in vivo* amyloid detection. [12, 13] The ligands are synthesized by researchers at Linköping University (LiU), whom this project was performed in close collaboration with.

1.2 Objectives

The overall aim of this project was to establish an Amyloid Transthyretin (ATTR) based cell model using the HEK-293 and SH-SY5Y cell lines, and detect the amyloid fibrils using novel fluorescent amyloid ligands, as well as characterize the bonding between the fibrils and ligands. This was carried out through four main objectives:

- Photophysical study of some novel fluorescent amyloid ligands, including their absorptive and emissive properties, quantum yields (QY) and fluorescence lifetimes.
- Photophysical study of the binding of some fluorescent amyloid ligands to both native and amyloid forms of Wild-Type Transthyretin (WT-TTR), including Fluorescence Resonance Energy Transfer (FRET), binding curves and fluorescence lifetimes.
- Establish a standard protocol for transfection of ATTR fibrils into human cells, using the HEK-293 and SH-SY5Y cell lines, and a protocol for staining them using fluorescent amyloid ligands. This included finding the optimal incubation time, ATTR concentration, ligand concentration etc.
- Spectroscopic imaging of cell models with ATTR and fluorescent amyloid ligands, performed via Confocal Laser Scanning Microscopy (CLSM) and Fluorescence Lifetime Imaging Microscopy (FLIM).

1.3 Approach

As a first step, a study of the change in emissive properties upon binding ATTR fibrils was conducted on a number of standard and novel amyloid ligands. Three were chosen for further study: X34, HS335 and HS336. An in-depth photophysical study was performed on these three ligands, in order to give reference data for comparison with staining of the ATTR cell model.

The binding of X34 and HS336 to both ATTR fibrils and native WT-TTR tetramers was further characterized by using binding curves formed from spectral data, as well as a FRET study performed with X34. The FRET studies were attempted due

¹Prodromal denotes the period where early symptoms may present and indicate the onset of a disease, before more diagnostically specific symptoms develop.

to a spectral overlap of the intrinsic fluorescence of Tryptophan (Trp) in the TTR molecules and the absorbance of X34, giving an opportunity to see the occurrence of FRET. A spectroscopic comparison was also performed on the binding of X34 to ATTR and amyloid insulin fibrils, to see if there was a difference in the interaction of the ligand with different types of amyloid fibrils.

An ATTR based cell model was established using the HEK-293 and SH-SY5Y cell lines seeded with *in vitro* ATTR. Suitable incubation times and concentration of fibrils and ligands were found through a series of CLSM experiments with close analysis and comparison of the results.

For the spectroscopic imaging of the cell models, a wealth of data was collected from each sample, including confocal images, emission spectra, fluorescence lifetime images and fluorescence lifetimes. Commercial stains were also used for easier visualization of cells and for determining co-localization with the stained ATTR fibrils. A comparison of amyloid insulin and ATTR fibrils in buffer and in HEK-293 cells was also performed to see any potential changes in behavior of the ligands or cells.

It is likely that the developed protocol for ATTR transfection and staining can be generalized for use with other amyloid proteins in human cell lines, and that the photophysical results can be used as a reference for future work with the fluorescent amyloid ligands.

1.4 Limitations

This Master project is first and foremost a trial project for using human cell lines for testing of amyloid fibrils and detecting them by using novel fluorescent amyloid ligands. A significant limitation with this project was the fact that work on amyloid fibrils can be dangerous. Thus, lack of access to proper lab facilities necessary for handling infectious amyloids, and lack of proper training for such work were constraints when choosing what amyloid protein to work with. Transthyretin (TTR) was chosen because of its favorable physical properties and characteristics, like its small size, well-characterized structure, excellent solubility and conformational stability, as well as its non-infectious qualities. [14] TTR amyloid fibrils are not infectious upon contact and can be handled safely in a Biosafety Level 1 (BSL-1) lab, while i.e. α -synuclein (α -syn), the amyloid protein associated with PD, has prion-like characteristics and requires BSL-3.

Another significant limitation of this Master project was time. There were many promising amyloid ligands, and due to the time-constraint, only the most promising ones were chosen for study in this project. For the same reason, only WT-TTR was chosen for use in the cell model, and not any of the mutant TTR types. The native and amyloid forms of WT-TTR will henceforth be referred to as WT-TTR tetramers and ATTR fibrils, respectively.

As cell work with ATTR and fluorescent amyloid ligands is also new, there was no set protocol for protein transfection or staining, and thus much of the work involved investigating the response of the cell lines to added ATTR fibrils and amyloid probes, and attempting to figure out a "standard" protocol for concentration of fibrils, concentration of amyloid ligands and incubation time, as well as other essential parameters that would emerge during experiments. Cell work is also very time-consuming, which is why the author only cultivated one cell line, while the SH-SY5Y cells were provided by PhD student Priyanka Swaminathan.

Chapter 2

Theory and Background

Some new methodologies used in the Master's thesis are introduced here. For theory and background of commonly used spectroscopy and microscopy, it is referred to the preparatory specialization project performed by the author in the fall of 2022. [15]

2.1 Cell Biology

2.1.1 Cell Cultivation

The division of normal cell lines is usually limited by a genetically determined event called senescence, where after a limited number of divisions, the cells lose their ability to proliferate. However, through a process called transformation, some cell lines can become immortal, acquiring the ability to divide indefinitely. This can either occur spontaneously or be chemically or virally induced. Such immortal cell lines are called continuous cell lines, and they are particularly useful in cell culturing. [16]

Cell culturing refers to laboratory methods that enable the growth of eukaryotic or prokaryotic cells in physiological conditions. [17] There are two main types of cell cultures, adherent and suspension cultures. In an adherent culture, the cells grow in a single monolayer attached to an artificial substrate. Adherent cultures require periodic subculturing and their growth is limited by the area of the substrate. On the other hand, a suspension culture will float around in 3 dimensions and is not limited to only one layer. [18] Adherent cells usually display spiked or polygonal morphologies, while cells grown in suspension generally adopt spherical shapes. [17]. For this project, the relevant cells are human adherent cells, and thus the theory will focus on these but could also be relevant for other types of cells.

One of the major problems for maintaining a cell culture *in vitro* is the risk of microbiological infections. Bacteria and other infectious agents are toxic to

eukaryotic cells and can lead to abnormal experimental results and eventually cell death. An important pre-requisite for successful cell work is therefore asepsis, the creation of a microenvironment free of undesirable pathogenic microorganisms, i.e. bacteria and viruses. All cell culture work therefore needs to be performed in a dedicated area, i.e. within a sterile bench specifically reserved for cell culturing. [17]

In addition to asepsis, a cell line also needs suitable growth conditions specifically adapted to the type of cell. Two factors are crucial for the creation of a favorable environment for maximum cell growth. The first is the use of a CO₂ incubator (5% CO₂), which ensures optimal temperature, humidity, oxygen and carbondioxide levels for the chosen cell type. Most human and mammalian cell lines are incubated at 36–37°C. The second important factor is the chosen cell culture medium and the added supplements. In addition to providing the cells with a steady supply of nutrients such as carbohydrates, amino acids, vitamins and minerals, the cell medium also needs to contain components that control physicochemical properties such as pH and cellular osmotic pressure. The pH level for most human and mammalian cell lines should be kept at a physiological pH level of 7.2–7.4. Fetal Bovine Serum (FBS) is commonly added to cell media, and provides cells with growth factors and hormones, as well as acting as a carrier for lipids and enzymes. However, as FBS is an animal-derived factor it is an undefined component and may vary between batches. It could therefore affect experimental results, which should be taken into account when planning cell experiments. It is possible to replace the cell medium with reduced-serum or serum-free medium, which relies on formulations that reduce or replace serum with more defined components. However these could increase oxidative stress for the cells since many of the anti-oxidation properties of serum are missing, and the health of the cells therefore needs to be closely monitored. [17, 19]

Confluency is an important term in cell culture biology, and refers to the percentage of the surface of a culture dish that is covered by adherent cells. Over time, cells cultured *in vitro* will deplete nutrients supplied in the medium, release toxic metabolites and grow in number. In order to maintain a healthy cell culture, a new culture of cells with a subset of the original culture is created and supplied with fresh cell medium. This process is referred to as cell subculturing and is usually performed when the growth of adherent cells reaches around 80% confluency. Subculturing requires detaching cells from the surface of the cell culture vessel, usually performed via the addition of Trypsin, a proteolytic enzyme that breaks down the proteins that allow the cells to adhere to a surface, leading to their dissociation from the cell culture vessel. The state of detachment can be monitored using a light microscope, and tapping of the culture vessels should dislodge any remaining adherent cells. [17] After detaching the cells, Trypsin needs to be inhibited in order to not damage the cells. If left for too long, Trypsin will begin cleaving the cell surface proteins, which will affect the further growth of the cells. The inhibition is usually performed by adding growth medium

containing FBS. In order to completely remove the Trypsin from the cell medium, ensuring no damage to the cells even if the Trypsin is not properly inhibited, the cells can also be centrifuged until all cell material is aggregated in a single cell pellet. After centrifugation, the supernatant is removed and the precipitate containing all the cells is dissolved in fresh, Trypsin-free medium.

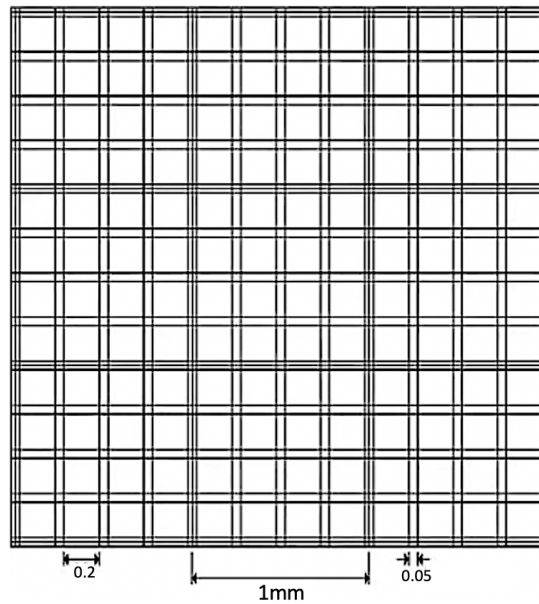


Figure 2.1: The layout of a Bürker chamber commonly used for cell counting; obtained from Fisher Scientific's official website. [20]

In order to make a cell suspension with known concentration, the cells need to be counted. This is performed using a Bürker chamber. A Bürker chamber is a glass plate with nine 1 mm^2 squares, each divided into sixteen group squares (figure 2.1). The chamber depth is 0.1 mm , giving each of the nine squares a volume of $0.1 \text{ }\mu\text{L}$. Before centrifugation, a small amount of single cell suspension ($\sim 20 \text{ }\mu\text{L}$) is pipetted onto the Bürker chamber until the surface is covered, with a cover glass ensuring even distribution. Cells are manually counted from three different squares placed diagonally to avoid inaccuracies due to uneven accumulation of cells on the Bürker chamber. Typically $25 - 75$ cells are counted per square, and the average of the number of cells counted per square will give the number of cells per $0.1 \text{ }\mu\text{L}$. To calculate the total amount of cells, the following formula is used:

$$C_T = C_{\text{Avg}} \cdot V_T \cdot 10^4, \quad (2.1)$$

where C_T is the total number of cells, C_{Avg} the average number of cells counted per area, and V_T the total volume of the cell suspension. C_{Avg} is multiplied by 10^4 to get the average number of cells per 1 mL , and then multiplied by V_T , the total cell suspension volume in mL , in order to get the total amount of cells.

2.1.2 SH-SY5Y Cell Line

The SH-SY5Y cell line is a non-patient-specific human cell line, generated from human-derived neuroblastoma cells and established in 1970. [21] The name SH-SY5Y is not an abbreviation, but rather the alphanumerical term for a cell line derived from the thrice-subcloned SK-N-SH cell line, first to SH-SY, then to SH-SY5, and finally to SH-SY5Y. [22] It is frequently chosen because of its human origin, catecholaminergic neuronal¹ properties, and ease of maintenance, and is widely used as an *in vitro* model in many areas of neuroscience, i.e. research on Alzheimers and Parkinsons disease among others. [24] Human catecholaminergic neuroblastoma cells resemble immature sympathetic neuroblasts in culture, and upon differentiation, will express the characteristic proteins associated with dopaminergic neurons, including tyrosine hydroxylase (TH) and dopamine transporter (DAT). [21, 25] In short, this means that SH-SY5Y cells can be differentiated to a more mature neuron-like phenotype that is characterized by neuronal markers. [22]

SH-SY5Y cell cultures include both adherent and floating cells, both of which are viable, however most reported studies only utilize the adherent cells and discard the floating cells when washing with Phosphate-Buffered Saline (PBS) and adding new growth medium. [22]

2.1.3 HEK-293 Cell Line

The Human Embryonic Kidney 293 (HEK-293) cell line is one common cell line used for research purposes. It was established in 1973 by transforming human embryonic kidney cells with sheared adenovirus type 5 DNA. [26, 27] The cell line is popular due to its ease of maintenance, robustness, high transfectivity, rapid growth rate, and ability to grow in a suspension serum-free culture. [28]

The HEK-293 cells are widely used for i.e. analyzing effects of drugs on sodium channels and the interactions between different proteins, as well as to produce proteins. The cells exhibit an epithelial cell morphology and they are adherent in culture. Typically, they appear less circular in morphology than other common cell lines, and they are somewhat granular. HEK-293 cells are also unusual, in that they are hypotriploid, meaning that they contain less than three times the number of chromosomes of a haploid human gamete.² Each HEK-293 cell contains two or more copies of each chromosome, with a modal chromosome number of 64, compared to 46 in a normal human diploid cell. [26]

¹Catecholaminergic neurons are neurons that communicate using one of two neurotransmitters: Dopamine (dopaminergic) or norepinephrine (noradrenergic). [23]

²Haploid refers to the presence of a single set of chromosomes in an organism's cells, contrary to diploid cells that have two sets of chromosomes. A gamete is the reproductive cell of an animal or plant. [29]

2.1.4 Amyloid Fibrils

Amyloid fibrils are insoluble protein aggregates found in a wide range of protein-misfolding diseases, including Alzheimer's disease, prion diseases, and several types of systemic amyloidosis. They are known to be cytotoxic, although the details behind the cell death mechanisms remain unclear. [30] Due to the insoluble nature of amyloids preventing the use of many biochemical tools, amyloid dyes have served as a dominant method of amyloid investigation since the method was first described in 1853. [8] Congo Red and Thioflavin-T (ThT) have historically been the golden standard for *in vitro* and *ex vivo* amyloid staining. These are fluorescent probes that stain amyloid deposits, and they are considered general amyloid stains. [7, 8]

Amyloid fibrils share a number of common structural features, despite being composed of different proteins that vary widely in amino acid sequence, native structure and physiological activity. [31, 32] They are characterized by a long, generally unbranched ribbon-like morphology, and amyloidogenic peptides and proteins share a characteristic cross- β -sheet structure in which adjacent β -sheets are held together by repetitive hydrogen-bonding that extends the length of the fibrils. [8, 32, 33]

Proteins can grow into amyloid fibrils regardless of the nature of their normal folding patterns, but one of the few patterns shared among amyloidogenic protein regions is the scarcity of proline residues. This is likely due to prolines strong disfavor of β -sheet structure, which is the dominant secondary structural feature of amyloid fibrils. Most amyloid proteins also contain a significant amount of hydrophobic residues, contributing to their insoluble nature. [31]

2.1.5 Transthyretin (TTR)

Transthyretin (TTR) is a 55kDa homo-tetrameric protein made up of 127 amino acids in each subunit. [34] Each TTR protein is comprised of four identical such subunits, making it a tetrameric protein. These four subunits each contain two antiparallel, four-stranded β -sheets that pack together to form the hydrophobic core of the protein. [5, 35] This hydrophobic core contains two ligand binding sites. [36]

TTR is one of the 20 proteins currently known to cause human amyloidosis. Wild-Type Transthyretin (WT-TTR) misfolds and aggregates into amyloid fibrils in elderly individuals, mainly manifesting as cardiac amyloidosis. [5, 34] Mutant TTR can also cause amyloidosis, being closely related with the occurrence of hereditary TTR amyloidosis like Familial Amyloid Polyneuropathy (FAP) and Familial Amyloid Cardiomyopathies (FAC). [5] TTR mutations are inherited dominantly and cause production of a destabilized tetrameric TTR protein, elevating the risk for amyloidosis. [34] Cardiac amyloidosis affects an estimated 25% of the population aged more than 80 years, while FAP affects approximately

1 in 100 000 persons. [14]

A proposed treatment for TTR amyloidosis involves drugs that bind to the ligand binding sites on the native TTR tetramer, stabilizing the structure of the tetramers to inhibit dissociation that give rise to toxic monomers, oligomers and insoluble amyloid fibers. [5, 37] The mechanisms of ligand binding to these two sites are poorly understood, but several studies indicate the presence of a main binding site with clear ligand affinity and a second minor site with a much lower ligand affinity, as well as negatively cooperative binding between the two. [38, 39] For mutant TTR protein amyloidosis, two additional treatment options exist: Liver transplantation, in order to reduce the production of mutant TTR protein, and reduction of mutant TTR protein expression through targeted gene silencing. [5]

Native tetrameric TTR is non-amyloidogenic, and needs to be dissociated into a monomeric intermediate before being capable of amyloid formation. [40] Native TTR tetramers are most stable under physiological conditions, pH 7.4 and 37°C, and may dissociate and undergo conformational changes under mild denaturing conditions, i.e. acidic pH, followed by self-assembly of the alternatively folded monomers into insoluble amyloid fibers. At physiological concentrations, tetrameric TTR remains associated and incapable of amyloid fibril formation from pH 7 to pH 5, but will dissociate to a monomer in a pH- and concentration-dependent process below pH 5. [35] For creation of fibrils *in vitro* for research purposes, lower temperatures and pH are often used to accelerate denaturation of the tetramer and subsequent fibril formation. Acidic media have been demonstrated to promote fibrillation of native TTR *in vitro* on a convenient laboratory time scale of 72 hours. [41]

Refolding kinetics data show that, in the absence of denaturant, the amyloid forms of both WT-TTR and mutant TTR will refold into their native tetrameric forms with a high yield. [42] To keep the TTR fibrils stable, they therefore need to be kept at low pH and low temperatures to avoid dissolution and refolding into the native state. Mutant TTR has been observed to refold at a much slower rate than WT-TTR. If refolding *in vivo* follows the same kinetic mechanisms, this points to a significantly increased probability of formation of mutant TTR amyloid fibrils *in vivo* compared to WT-TTR amyloid fibrils. [36]

Tryptophan (Trp) is a naturally occurring amino acid known to emit intrinsic fluorescence that can be measured by fluorescence spectroscopy to study protein structure and function. [43] As TTR is a Trp-rich molecule, this intrinsic fluorescence can be measured in order to follow the conformational changes of TTR. [44] There are two Trp residues in each of the four identical subunits of a WT-TTR tetramer. [36] These Trp molecules have excitation wavelength at 280 nm and emit fluorescence between 300–420nm. Changes in the fluorescence spectrum or a shift in the maximum fluorescence peak can be used to study structural changes of TTR, such as denaturation and amyloid formation. [43, 45]

Researchers at LiU and NTNU have previously studied the effect of native and

amyloidic TTR conformations on the SH-SY5Y cells, described in a publication by Sörgjerd et al. in 2008. [46] Early TTR oligomers proved highly cytotoxic and induced apoptosis after 48h of incubation, while cells exposed to more mature fibrils (>24h of fibrillation) showed similar morphology to the control cells. [46] The amyloid formation process was followed using the widely used Thioflavin-T (ThT) fluorescence, a standard assay that has shortcomings when it comes to fluorescence microscopy, as it also interacts with other biomolecules such as DNA. [47] ThT also has a short excitation wavelength, at 349 nm, which complicates its use in i.e. Confocal Laser Scanning Microscopy (CLSM). [48] It is here anticipated that the results could be improved using more recently developed fluorescent amyloid ligands, as they have the potential to detect and distinguish amyloid polymorphism. [46]

2.1.6 Insulin

Insulin is a 5.81kDa hormone composed of 51 amino acids, forming two polypeptide chains composed of 21 and 30 residues, linked together by two disulfide bonds. Insulin is important for the control of glucose metabolism and diabetes treatment. [49] Amyloidic insulin balls may form at the insulin-injection site in patients with diabetes after repeated injection at the same sites, causing poor glycemic control due to impaired insulin absorption. [50] Studies have shown that these insulin balls have varying levels of cytotoxicity, implying amyloid polymorphism. [49]

Insulin is a well-known and extensively studied model protein for amyloid fibril studies, known to form two types of morphologically differing amyloids under different solvent conditions; flexible filaments are formed in the presence of a reducing agent and rigid linear fibrils from intact insulin. [30, 50, 51] The cytotoxicity of the insulin filaments has been found to be remarkably lower than that of the insulin fibrils, a finding that suggests a correlation between cell toxicity of amyloids and their morphology. [30] These insulin filaments and fibrils can be a good model system for understanding the underlying mechanisms of amyloid toxicity, as they are produced from the same polypeptide and their different toxicities are thus decided by their structural differences. [30, 51]

The structural polymorphism of insulin amyloid aggregates has previously been shown to be differentiated by the specific fluorescent amyloid probes Pentamer Formyl Thiophene Acetic Acid (p-FTAA) and benzostyryl capped benzothiadiazole 2,1,3-Benzothiadiazole 21 (BTD21). p-FTAA detects the cytotoxic insulin fibrils, while BTD21 detects the less ordered, non-toxic insulin filaments. [50] Using fluorescent amyloid ligands, the cell binding of non-toxic filamentous amyloids of insulin has also been found to be less efficient than that of toxic fibrillar amyloids; suggesting a correlation between amyloid cytotoxicity and cell affinity. [51]

2.1.7 Ligand Binding and Binding Constants

A characteristic property of nearly all proteins is their ability to bind specifically to another molecule. Ligand binding is generally explained in terms of the equilibrium constant K_d for the protein-ligand complex dissociation. [52]

The equilibrium equation for formation of a protein-ligand complex for a single binding site is defined as



where $[L]$ and $[P]$ are the concentrations of free ligand and protein, respectively, while $[PL]$ is the concentration of the protein-ligand complex. Using this equation, the dissociation equilibrium constant K_d can be defined as:

$$K_d = \frac{k_{\text{off}}}{k_{\text{on}}} = \frac{[P][L]}{[PL]}, \quad (2.3)$$

where k_{on} is the rate constant of association and k_{off} the rate constant of dissociation. The unit for K_d is M. [53] Two different protein-ligand complexes may have the same dissociation constant K_d , but different values for k_{on} and k_{off} . [54]

When 50% of the proteins are bound to ligands, $[P] = [PL]$, giving $K_d = [L]$. A high K_d means that a large concentration of ligand is required to bind 50% of the proteins, indicating that the ligand and protein have low affinity for one another. On the other hand, a low K_d value means that the ligand has high affinity for the protein and fewer molecules of the ligand are required to bind 50% of the proteins. [53]

The equation for K_d is complicated by the presence of more than one binding site. For proteins with two ligand binding sites, an additional equilibrium equation is required:



This equation is described by a second dissociation constant, $K_{d,2}$, giving two dissociation constants defined as:

$$K_{d,1} = \frac{[P][L]}{[PL]}, K_{d,2} = \frac{[L][PL]}{[PL_2]}. \quad (2.5)$$

This complicates calculation of the dissociation constant compared to proteins with only one ligand binding site, and each additional binding site will complicate the calculations further. [55]

2.2 Photophysics

For extensive theory on fluorescence, spectroscopy and Time-Correlated Single Photon Counting (TCSPC) see the authors specialization project from fall 2022. [15] A condensed description on these topics will be presented here to give some basic understanding of some key concepts.

2.2.1 Fluorescence

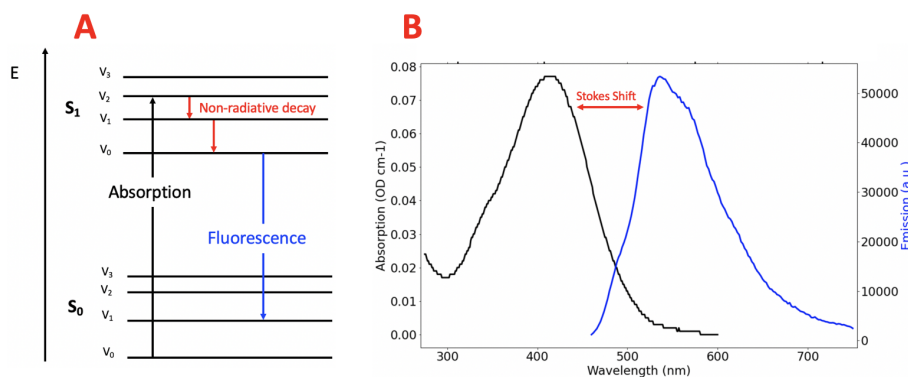


Figure 2.2: Illustration of some key concepts in fluorescence, (A) a Jablonski diagram showing the energy levels of a molecule, with S_0 denoting the ground state and S_1 an excited singlet state, and (B) the absorption and emission spectra of a fluorophore separated by a Stokes shift.

Fluorescence is a phenomenon caused by molecules absorbing photons and being excited from the ground state to a higher energy state, releasing photons upon return to the ground state. Fluorescence is specifically the emission of photons from an excited singlet state, as illustrated by the Jablonski diagram in figure 2.2A. S_0 denotes the ground state, while S_1 and higher are excited singlet states. Each of the energy states also have a number of vibrational sub-levels. [56]

The absorbance and fluorescence emission of a fluorophore can be measured with a spectrophotometer and fluorophotometer, respectively, giving a set of spectra as shown in figure 2.2B. The absorption spectrum gives the change in absorbance of a fluorophore as a function of the excitation wavelength, while the emission spectrum shows the change in fluorescence intensity as a function of the emission wavelength. Emission typically occurs at lower energies and longer wavelengths than absorption, due to the rapid decay of the fluorophore to the lowest of the vibrational excited states, see figure 2.2A. This is called vibrational relaxation, and the energy will be transformed into kinetic energy, causing a shift between the wavelengths of absorption and emission called the Stokes shift. [56] Alternatively to measuring the absorption spectrum, the excitation spectrum of a fluorophore can be measured, showing the change in fluorescence intensity as a function of the excitation wavelength.

Absorbance is defined by Beer-Lamberts law as

$$A(\lambda) = \epsilon(\lambda) \cdot l \cdot c, \quad (2.6)$$

where ϵ is the molar extinction coefficient, l is the path length of the light corresponding to the width of the chosen cuvette, and c is the concentration of the substance. The molar extinction coefficient is a characteristic that determines how strongly a substance absorbs light at a particular wavelength, and is affected by the choice of solvent. [57]

2.2.2 Quantum Yield (QY)

The quantum yield of a fluorophore is the number of emitted photons relative to the absorbed photons, defined as

$$Q = \frac{\Gamma}{\Gamma + k_{nr}}, \quad (2.7)$$

where Γ is the radiative emission and k_{nr} the non-radiative emission. The quantum yield will be close to unity if the non-radiative emission is much smaller than the radiative emission, $k_{nr} \ll \Gamma$, meaning that all the absorbed photons are released as photons rather than as non-radiative energy. However, because of Stokes losses, the energy yield of fluorescence will always be smaller than unity. [56]

2.2.3 Fluorescence Lifetime and Time-Correlated Single Photon Counting (TCSPC)

The fluorescence lifetime of a fluorophore is the time available for the fluorophore to interact with or diffuse in its environment, and is defined by the average time the molecule spends in the excited state prior to return to the ground state. It is typically in the range of 1 – 10 ns at room temperature. The lifetime can give additional information about the environment of the fluorophore, i.e. solvent effects, aggregation and interactions with macromolecules. [56] Spectral analyses are thus often performed in parallel with lifetime measurements in order to get a more comprehensive understanding of the behavior of the fluorophore.

Time-Correlated Single Photon Counting (TCSPC) is a common technique for fluorescence lifetime measurements. The principle is the detection of single photons and the measurement of their arrival times in respect to a reference signal, usually the light source. [15] The result is an intensity decay that can be fitted to a single exponential expression:

$$I(t) = I_0 \exp(-t/\tau), \quad (2.8)$$

where I_0 is the initial intensity of the fluorophore at time zero, and τ is the fluorescence lifetime. [56] Thus, by fitting the decay to a single exponential, the

lifetime can be read directly from the found expression, without need for further calculations. [15]

Some fluorophores display decays too complex to be described by a single exponential, and are instead fitted to the multiexponential model. The total decay is then assumed to be a sum of single exponential decays, each with their own lifetime. The expression is then:

$$I(t) = \sum_i \alpha_i \exp(-t/\tau_i), \quad (2.9)$$

where $\sum_i \alpha_i$ is normalized to unity.

For a double exponential decay, the intensity averaged lifetime, $\bar{\tau}$, can be calculated by the following equation:

$$\bar{\tau} = \frac{\alpha_1 \tau_1^2 + \alpha_2 \tau_2^2}{\alpha_1 \tau_1 + \alpha_2 \tau_2}. \quad (2.10)$$

Here, $\alpha_i \tau_i$ represents the number of emitted photons for each component. [56]

2.2.4 Solvent Effects and Quenching

The emission properties of fluorophores are affected by solvent polarity and the local environment to a great extent. The most obvious effect of solvent polarity is the Stokes shift, see figure 2.2, where excess vibrational energy is lost to the solvent. [56]

Solvatochromism is the phenomenon observed when the color due to a solute is different when that solute is dissolved in different solvents. [58] It affects polar fluorophores by stabilizing either the excited or ground state more than the other, due to a difference in dipole moment between the two states. If the excited state has a larger dipole moment than the ground state, the solvent dipoles can reorient and relax after excitation, which lowers the energy of the state, resulting in emissions of lower energy. This effect becomes larger with increased solvent polarity. [56]

There are two types of solvatochromism, positive and negative. For positive solvatochromism, the excited state of the fluorophore is more polar than the ground state. Thus, when the solvent is more polar, there will be a smaller energy difference between the excited and ground state, and the fluorescence spectrum will show a red-shift. For less polar solvents, the fluorescence spectrum will show a blue-shift. This is the most common type of solvatochromism, and is therefore commonly referred to as *normal solvatochromism*. These fluorophores will also gain an increased Stokes shift for polar solvents, and usually also shorter lifetimes and lower QY. [58]

The less common type is negative solvatochromism, where the fluorophore has a ground state that is more polar than the excited state. Contrary to normal

solvatochromism, the fluorescence spectrum will become blue-shifted with more polar solvents, and red-shifted for less polar solvents. This is referred to as *anomalous solvatochromism*. [58]

Fluorescence quenching refers to any process that decreases the fluorescence intensity of a sample. The phenomenon can be caused by a variety of molecular interactions, including excited-state reactions, energy transfer, and collisional quenching. [56]

Quenching is divided into two main categories: dynamic and static quenching. Dynamic quenching is caused by collisional encounters between the fluorophore and quencher, while static quenching is due to complex formation. Both types require molecular contact between the fluorophore and quencher. [56] There is also intrinsic quenching, where the fluorophore is the only solute and quenching is caused by the solvent, with the extent of quenching decided by the solvent polarity and temperature.

Dynamic fluorescence quenching can be described by the Stern-Volmer equation:

$$\frac{F_0}{F} = 1 + k_q \tau_0 [Q] = 1 + K_D [Q], \quad (2.11)$$

where F_0 and F are the fluorescence intensities in the absence and presence of the quencher, respectively. k_q is the bimolecular quenching constant, τ_0 is the lifetime of the fluorophore in the absence of the quencher, and $[Q]$ is the concentration of quencher. K_D is the Stern-Volmer quenching constant, given by $K_D = k_q \tau_0$. [56]

The Stern-Volmer quenching constant (K_D) informs the sensitivity of the fluorophore to a quencher. A fluorophore buried in a macromolecule will usually be inaccessible to water soluble quenchers, giving a low value for K_D , while free fluorophores in solution or on the surface of a biomolecule will give larger values of K_D . The bimolecular quenching constant (k_q), also reflects the efficiency of quenching or the accessibility of the fluorophores to the quencher. Diffusion-controlled quenching will typically yield values of k_q near $1 \cdot 10^{10} \text{M}^{-1} \text{s}^{-1}$. Values smaller than this diffusion-controlled value can result from low quenching efficiency or shielding of the fluorophore, while values of k_q larger than the diffusion-controlled limit usually indicate some type of binding interaction. [56]

Quenching data can be presented graphically in a Stern-Volmer quenching plot, where the relative fluorescence intensity F_0/F is plotted against the quenching concentration $[Q]$. For dynamic quenching, F_0/F is expected to be linearly dependent on the concentration of quencher. Fitting the data to a linear equation will thus yield a slope equal to the Stern-Volmer quenching constant, K_D and an intercept of 1 on the y-axis. Such a linear Stern-Volmer plot generally indicates that there is only one type of fluorophores in the solution, and that they are easily accessible to the quencher. [56]

However, dynamic quenching is not proven by the observation of a linear Stern-Volmer plot, as static quenching will also result in linear plots. Nevertheless,

an important characteristic of dynamic quenching is the equivalent decrease in fluorescence intensity and lifetime with addition of the quencher. [56] The two forms of quenching can therefore be distinguished by lifetime measurements, as the following equation is only true for dynamic quenching:

$$\frac{F_0}{F} = \frac{\tau_0}{\tau}. \quad (2.12)$$

Here, τ_0 is the lifetime of the fluorophore in absence of the quencher, while τ is the lifetime in the presence of the quencher. Thus, if the quenching data and lifetime data give the same Stern-Volmer constant when fitted to a linear equation, it points to the quenching being dynamic. [56]

2.2.5 Plate Reader Spectroscopy

A microplate reader is an instrument used to measure the spectroscopic properties of small sample volumes (20 – 200 μ L). Separating the samples into individual wells in a microplate makes it possible to complete measurements without needing to switch between samples, making a microplate reader useful for minimizing operational time and saving reagent costs. Microplate readers can measure a number of different spectroscopic properties, including absorbance, fluorescence intensity and luminescence. The light signal is registered by a detector, typically a Photomultiplier Tube (PMT). The PMT converts the photons into electricity, which is then quantified by the microplate reader. [59]

The light is typically provided by a broadband xenon flashlamp, and samples can be excited at specific wavelengths through the use of a specific excitation filter or monochromator. In order to increase sensitivity and specificity, filters or monochromators can also be employed on the emission side. These are usually placed between the sample and the detector. The wavelength range of the microplate reader is thus decided by the optical system and its chosen filters, combined with the PMT. [59]

In this Master's thesis, a Tecan plate reader at the Protein folding and Ligand Interaction Core (ProLinC) facility at Linköping University (LiU) was used to study the binding between fluorescent markers and various protein aggregates. This was performed during a research stay at LiU in February 2023.

2.2.6 Fluorescence Resonance Energy Transfer (FRET)

Fluorescence Resonance Energy Transfer (FRET) is a distance-dependent physical process where energy is transferred non-radiatively from an excited molecular fluorophore functioning as the donor, to another fluorophore referred to as the acceptor. The energy is transferred via intermolecular long-range dipole-dipole coupling, which requires a spectral overlap between the emission spectrum of the donor and the absorption spectrum of the acceptor as well as a distance between

the two molecules typically below 10 nm. [60] The rate of energy transfer depends upon the extent of spectral overlap, the quantum yield of the donor, the relative orientation of the donor and acceptor transition dipoles, and the distance between the donor and acceptor molecules. [56] If FRET occurs, the donor fluorescence will be quenched and the acceptor fluorescence will be sensitized or increased. [60] FRET can be used to monitor distances between proteins, protein–protein interactions and protein conformational changes in live biological samples. [56, 61]

In this Master’s thesis, FRET experiments were used to discern whether there is FRET occurring for WT-TTR molecules bound to fluorescent amyloid ligands. Moreover, whether there is a difference in the FRET sensitivity between WT-TTR tetramers and ATTR fibrils. The purpose here was to check if the fibrils are stable or if they re-fold back into tetramers upon a raise in pH to 7.4.

2.3 Microscopy

Theory on Brightfield (BF) microscopy, fluorescence microscopy and Confocal Laser Scanning Microscopy (CLSM) was described in the authors specialization project from fall 2022, where these techniques were used to investigate the interaction of three Luminescent Conjugated Oligothiophenes (LCOs) with HEK-293 cells. [15] The techniques are applied in the same manner in this Master’s thesis, with the addition of ATTR to the cell model being the only major change, see section 3.4 for details.

2.3.1 Fluorescence Lifetime Imaging Microscopy (FLIM)

Fluorescence Lifetime Imaging Microscopy (FLIM) is a microscopy technique that utilizes the differing lifetimes of the fluorophores in the sample to create contrast, rather than the differences in their emission spectra as in regular fluorescence microscopy. The technique is based on Time-Correlated Single Photon Counting (TCSPC), described briefly in section 2.2.3 and in detail in the authors specialization project. [15] TCSPC is a sensitive, accurate and precise method of measuring photon arrival times after an excitation pulse. The technique has a large dynamic range, and requires only a low illumination intensity. [62] TCSPC gives a histogram of photon arrival times that represent the intensity decay of the sample, which can then be tail-fitted to an n-th exponential equation to find the estimated fluorescence lifetime of the sample. [56]

FLIM has high specificity and sensitivity, is non-destructive and can image live samples in a minimally invasive manner. [62] The fluorescence lifetime of a fluorophore depends on the local micro-environment of the sample, making FLIM useful for studying the environment of the fluorophore, i.e. concentration of oxygen, pH, or protein-protein interactions. [63] FLIM also has the advantage of being able to discriminate spectrally overlapping fluorophores that would

appear equal when using intensity-based fluorescence microscopy. [64] The lifetime is also independent of concentration of the fluorophore, photobleaching and excitation intensity, among others, making it a more robust technique than other fluorescence-based imaging. [65] Contrary to fluorescence intensity, lifetime is an absolute measurement that can be repeated across numerous device configurations after accounting for the Instrument Response Function (IRF) of that device, making FLIM experiments reproducible and comparable between different instrumentation configurations. [64]

FLIM is widely used in combination with FRET imaging in order to improve the accuracy of FRET. Intensity-based FRET can be susceptible to changes in the concentration of fluorophore, while the fluorescence lifetime is independent of the fluorophore concentration, allowing the FLIM-FRET method to give accurate measurements despite concentration changes. The advantage of FLIM over regular TCSPC lifetime measurements is that TCSPC will give an averaged lifetime over the whole sample, while for FLIM the sample is visualized and an ROI of the specific molecules of interest, here the donor fluorophore, can be selected. This improves the accuracy of the measured lifetime. [66] The use of FLIM also enables FRET imaging in cells. [56]

Single-Photon Avalanche Diodes (SPAD) photodetectors can increase the speed of FLIM measurements. These are a type of Avalanche Photodiodes (APDs), which are photodiodes based on a p-n junction, and do not require vacuum or voltages in the kV range like i.e. Photomultiplier Tube (PMT) detectors. A photodiode is a diode³ with a depletion region largely devoid of mobile charge carriers, but upon photon absorption an electron-hole pair is created. Application of an electric field, called *reverse bias*, allows the electrons to travel to the cathode, and the holes to the anode, creating a flow of current from the absorption of photons in the depletion region. [62] An avalanche photodiode operates with a higher reverse voltage, giving a stronger electric field that allows avalanche multiplication of the charge carriers formed upon photon absorption. This avalanche effect allows the gain of the photodiode to be enhanced several times to provide a high range of sensitivity. [67]

SPADs are APDs that are operated with a reverse voltage above the breakdown voltage of a typical APD, referred to as *Geiger mode*, which is particularly useful for single-photon detection. Upon photon absorption, an electron avalanche is initiated, which reduces the reverse bias below the breakdown voltage and eventually stops the avalanche. [62] The main advantages of SPAD are the picosecond temporal resolution and single-photon sensitivity, making it an efficient tool for time-resolved imaging like FLIM. [68] SPADs and APDs can also have larger quantum efficiencies than i.e. PMTs, up to about 80%. [62]

³A diode is an electronic component that allows current to flow through it in one direction, but not the other.

Chapter 3

Materials and Methods

3.1 Fluorescent Amyloid Ligands

Three different amyloid ligands were investigated as fluorescent probes in this project: X34, HS335, and HS336. Their structures are shown in figure 3.1, and some background information about each of these probes will be presented in this section. The amyloid ligands HS-68, HS-84 and h-FTAA were extensively described in the preparatory specialization project and will thus not be discussed here. [15]

X34 is an amyloid ligand that has been proven to efficiently stain various amyloid deposits in AD brains. It is a lipophilic, highly fluorescent derivative of Congo Red (CR). [7] CR is a standard amyloid probe that has been in use for decades, and it is still one of the major methods used to detect the structure of amyloids in protein aggregates. [69] The probe stains β -pleated sheet secondary protein structures, regardless of their primary amino acid structures. β -pleated sheet structures are commonly found in amyloid deposits, and CR will therefore stain a variety of amyloid deposits composed of proteins with very different primary amino acid sequences. [7] Structurally, it is an azo dye¹ that contains naphthalenesulfonic acid groups, which are both generally highly toxic, making it disadvantageous for *in vivo* applications. [7]

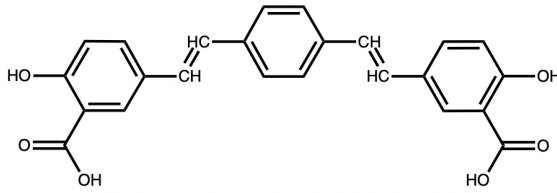
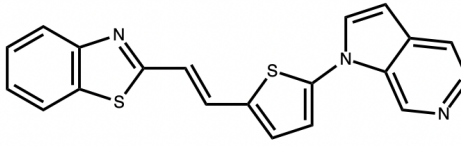
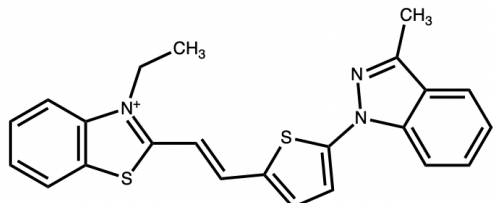
In X34, the naphthalenesulfonic acid groups are replaced by salicylic acids, and the azo groups are replaced by carbon-to-carbon double bonds. [7] This makes X34 more suitable for *in vivo* applications, and the change to carbons also has the added advantage of making X34 highly fluorescent upon association with amyloids. The salicylic groups also add lipophilic properties, which gives X34 the ability to enter the brain to a greater extent than CR. These properties both contribute to X34 being a potential *in vivo* probe for amyloid deposits. [71] Like CR, X34 stains β -pleated sheet secondary structures, regardless of the primary amino acid sequence of the amyloid protein. In addition to binding β -pleated

¹Azo dyes are synthetic, organic dyes that contain an azo group (-N=N-). [70]

sheet protein configurations of A β , it has been shown to also stain amyloid deposits in systemic amyloidosis, suggesting that X34 is a general amyloid probe. [7]

X34 is soluble at low millimolar concentrations in aqueous solution at basic or neutral pH, and is very soluble in organic solvents, i.e. DMSO. [7] The ligand X34 has additional functions as a molecular intermediary for the development of new amyloid probes. By replacing the central benzene unit of X34, the probe has been synthesized into derivatives that have been shown to retain the amyloid binding properties of X34, while also gaining new fluorescent properties. [72] One such derivative is BTDSB, see appendix A for more information on this stain.

Table 3.1: Structure of X34, HS335 and HS336, drawn using ChemDraw. Structures of HS335 and HS336 were provided by Linköping University (LiU).

Name	Structure	Ref
X34		[7]
HS335		LiU
HS336		LiU

HS335 and HS336 both belong to a new class of thiophene-based ligands that are afforded by merging Luminescent Conjugated Oligothiophenes (LCOs) with heterocyclic motifs from other types of amyloid ligands. LCOs are ultrasensitive fluorescent dyes that bind and spectrally distinguish different types of amyloid aggregates. [73] [74] Their general characteristics were described in the author's specialization project, and will not be given here. [15] In contrast to LCOs, the new class of thiophene-based ligands have shown selectivity towards distinct protein aggregates, such as Tau amyloid deposits in AD, as well as different binding modes and photophysical properties compared to LCOs. [75]

3.2 Cell Cultivation

For use in this project, the author cultivated a HEK-293 cell line, while PhD student Priyanka Swaminathan cultivated both a HEK-293 cell line and a SH-SY5Y cell line. These cell lines require largely the same procedure of cell cultivation, which will be described in detail here.

When cultivating a cell line, two procedures have to be performed regularly, in intervals dependent on factors like the cell type, growth speed, etc. These two procedures are cell subculturing and cell growth medium change. The cell lines were subcultured twice a week depending on their confluence, with the schedule adjusted to the individual needs of each week and to the rate of growth of the cells. Cell growth medium was changed as needed. The HEK-293 cells were grown in T75 cell culture flasks, which have a surface area of 75 cm², and the SH-SY5Y cells grown in parallel in two T25 cell culture flasks, with a surface area of 25 cm². Before cell subculturing, the degree of confluency of the cells was determined via BF microscopy, and the subculturing was proceeded with if the cells covered at least ~ 80% of the flask surface.

When subculturing the cell lines, the procedure was as follows:

1. Growth medium, Phosphate-Buffered Saline (PBS) and Trypsin/EDTA were pre-heated in a 37 °C water bath. The growth medium used for the HEK-293 cells was Eagle's Minimum Essential Medium (EMEM) medium with L-Glutamine (2 mM) and supplemented Fetal Bovine Serum (FBS) (10%). The growth medium used for the SH-SY5Y cells was a 1:1 mixture of EMEM with L-glutamine (2 mM) and Nutrient Mixture F-12 (F-12) medium, supplemented with FBS (10%).
2. Old medium was removed from the cell flask and discarded.
3. Cell monolayer was washed gently using 5 mL PBS. The PBS was then removed and discarded.
4. 2 mL of Trypsin/EDTA was added to detach the cell monolayer from the cell flask. The cell flask was placed at 37 °C for 2-3 minutes.
5. Cells were observed in a microscope to ensure proper detachment.
6. 8 mL of growth medium was added to the cell flask, with gentle re-suspensions to ensure a homogeneous solution.
7. Cell suspension was transferred to a sterile centrifuge tube.
8. A small amount of cell suspension was taken from the centrifuge tube (~ 20 µL) and added to the Bürker chamber. The cells were counted, and the total number of cells was calculated.
9. Cells in the centrifuge tube were centrifuged at 1500 rpm (378 g) for 5 minutes. (Kendro Megafuge 1.0, Osterode, Germany)
10. The supernatant was removed from the centrifugation tube and discarded.
11. Growth medium of a volume giving a 1mill/mL concentration of cells was added to the centrifugation tube and re-suspended for a homogeneous

solution.

12. 13 mL of fresh growth medium was added to a new T75 cell flask for the HEK-293 cells, or 5 mL medium to two T25 flasks for the SH-SY5Y cells.
13. The necessary number of cells was added to the cell flask, generally $1 \cdot 10^6$ for HEK-293 cells, and $5 \cdot 10^5$ to each flask for SH-SY5Y cells.
14. The new cell flasks were placed in the incubator (37°C , 5% CO_2).

When changing the cell medium, the procedure was as follows:

1. Growth medium was preheated to 37°C in a water bath.
2. Old growth medium was removed from the cell flask and discarded.
3. 13 mL of fresh growth medium was added to the cell flask for HEK-293 cells, and 5 mL for SH-SY5Y.
4. The cell flask was placed in the incubator (37°C , 5% CO_2).

3.3 Photophysics

The procedures for measuring absorption and emission spectroscopy, quantum yield, and fluorescence lifetime are described in greater detail the author's specialization project from fall 2022. [15]

3.3.1 Quantum Yield (QY)

Absorption and emission spectroscopy was performed using a UV/Visible double beam spectrophotometer (Shimadzu UV-1601PC, Kyoto, Japan) and fluorophotometer (Horiba PTI QuantaMaster 8075-22, Kyoto, Japan), respectively. For Quantum Yield (QY) measurements, the absorption and emission spectra were measured at three concentrations. The concentrations can be chosen arbitrarily, but ideally they should be evenly spaced and the measured absorbance be kept below 0.15 ODcm^{-1} , in order to avoid re-absorption and quenching effects. Concentrations giving higher absorbance can be used as well as long as the data points still fit with the linear relation between maximum absorbance and total fluorescence emission of the lower concentrations, see figure 3.1. The molar extinction coefficient (ϵ) was calculated for each ligand in all solvents, using equation (2.6) at the maximum absorbance at the highest measured concentration, with a path length of 10 mm for all samples.

As shown in figure 3.1, the maximum absorption was plotted against the total fluorescence intensity for all three concentrations and fitted to a linear function, giving a linear slope equal to the relative QY of the sample. The same procedure was performed on a reference with a known quantum yield, as absolute QY is difficult to measure accurately. Comparing the relative QY of the sample to both the relative and absolute QY of the reference, the absolute QY of the sample was

calculated using the following equation:

$$Q_x = S_x \cdot \frac{Q_r}{S_r} \cdot \frac{\eta_x^2}{\eta_r^2}, \quad (3.1)$$

where S_x , S_r and Q_x , Q_r are the relative and absolute QY of the sample and reference, respectively. The η_x and η_r are refractive indexes of the solvents and can be found tabulated in table 3.2. The fluorophore Coumarin 153 (C-153) was used as a reference in this project, with a known QY of $54.4\% \pm 2.8\%$ in EtOH, explained by Rurack and Spieles (2011). [76] See appendix B for spectra and plots used for QY calculations.

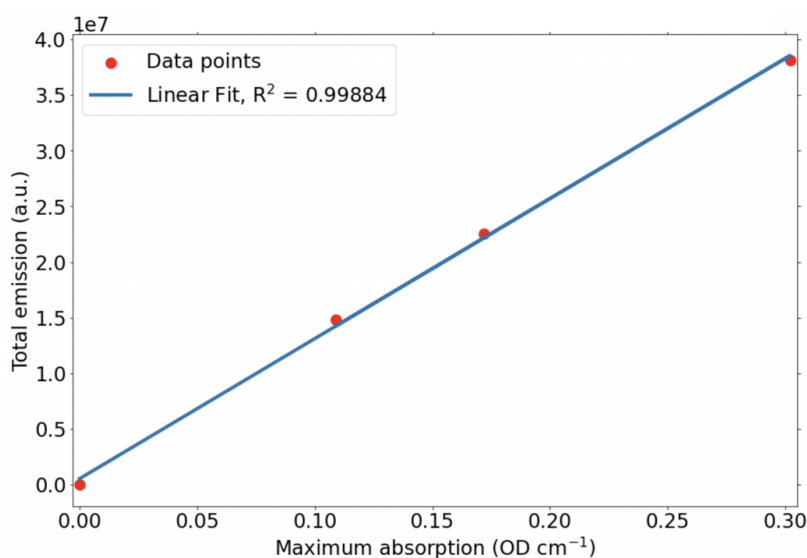


Figure 3.1: Example of the linear relation between the maximum absorbance and total fluorescence emission for a fluorophore, used in QY calculations. Concentrations giving higher absorbance than 0.15 ODcm^{-1} can be included as long as they still fit with the relation of the lower concentrations.

Table 3.2: Refractive indexes of the solvents used in the photophysics experiments.

Solvent	Refractive index	Reference
MeOH	1.326	[77]
EtOH	1.359	[77]
PBS	1.33	[78]
MeCN	1.344	[77]
CHCl ₃	1.446	[77]
DMSO	1.479	[77]
PrOH	1.386	[77]
THF	1.407	[77]

3.3.2 Fluorescence Lifetime

The fluorescence lifetimes of the samples were measured with the TCSPC technique, using a Picosecond photon detection module (Horiba TBX-04, Kyoto, Japan). With the software Decay Analysis Software 6 (DAS6), the intensity decay was fitted to either a single or double exponential expression, depending on the complexity of the decay. For single exponential equations, the lifetime was found directly from the equation, while double exponential lifetimes were calculated as an average of the two values using equation (2.9).

3.3.3 Plate Reader Spectroscopy

The following section was performed at the Protein folding and Ligand Interaction Core (ProLinC) facility at Linköping University (LiU) in February 2023.

A microplate reader provided by ProLinC at LiU (Tecan Infinite M1000 Pro, Salzburg, Austria) was used for the plate reader spectroscopy. It is a multifunctional monochromator-based microplate reader that can record absorption and emission spectra, as well as more advanced fluorescence and luminescence scans. It can measure any standard microplate, ranging from 6 to 1536-well formats. [79] For both the plate reader experiments, a 96 well plate (12x8) was prepared, with 100 μ L of sample solution for each well.

Amyloid Probe Investigation

The first plate reader experiment was an investigation of various standard and novel amyloid probes, to see which would be viable for Amyloid Transthyretin (ATTR) detection. Six wells were prepared for each amyloid probe. Three samples were prepared for pH 7.4, one with probe only, one with ATTR fibrils and probe, and one blank sample to measure the contribution from the solvent. The same three combinations were prepared for pH 2.0.

The six samples were prepared as follows:

- **ATTR samples:** 80 μ L of dilution buffer and 20 μ L ATTR fibrils. Then 3.3 μ L of probe was added. For pH 7.4, PBS was used instead of dilution buffer.
- **Probe-only samples:** 100 μ L dilution buffer and 3.3 μ L probe. For pH 7.4, PBS was used instead of dilution buffer.
- **Blank samples:** 100 μ L dilution buffer for pH 2 and 80 μ L PBS and 20 μ L dilution buffer for pH 7.4.

Each well was excited at 5 different wavelengths, 373 nm (400–620nm), 405 nm (450 – 620nm), 450 nm (470 – 700nm), 480 nm (500 – 700nm) and 535 nm (550 – 750nm), with corresponding measurements of emission wavelengths in parentheses. Excitation and emission slits of 5 nm were used, and a gain of 150.

The same measurements were repeated 24 h later using the same samples to see their evolution over time.

The emission at each excitation wavelength was then plotted using the Python programming language.

X34 and HS336 Binding Curves

It was decided to perform additional measurements on X34 and HS336 in order to create binding curves for the binding of the ligands to WT-TTR tetramers compared to ATTR fibrils.

For HS336, a 96 well plate was once again prepared, with two rows containing 0.5 μM WT-TTR tetramers, two containing 0.5 μM ATTR fibrils and two having only PBS. Each row contained 11 different concentrations of HS336, ranging from 0 nM to 4000 nM.

A 96 well plate was also used for X34, with three rows containing 0.5 μM WT-TTR tetramers, three containing 0.5 μM ATTR fibrils and two having only PBS. Each row contained 10 different concentrations of X34, ranging from 0 nM to 2500 nM.

All wells with HS336 were excited at 535 nm and emission was measured from 550–750nm. For X34, all wells were excited at 373 nm and emission was measured from 400 – 620nm. Once again, excitation and emission slits of 5 nm were used, and a gain of 150. The average total intensity of emission from each sample was then plotted as a function of the added concentration of ligand in Python. For HS336, the measurements were repeated after 24 h to see if there were any changes in the binding over time.

3.3.4 Photophysical Properties of X34 Bound to Insulin and ATTR Fibrils

Three samples were made for the photophysical comparison of ATTR and insulin fibrils, 5 μM X34 with 7.1 μM ATTR fibrils, 5 μM X34 with 7.1 μM insulin fibrils, and 5 μM X34 alone, all in PBS. The excitation and emission spectra were measured for each sample, as well as their fluorescent lifetimes.

3.3.5 Fluorescence Resonance Energy Transfer (FRET)

Since the absorption of X34 overlaps well with the emission of Tryptophan (Trp), Fluorescence Resonance Energy Transfer (FRET) measurement was attempted. This also gave an opportunity to see if there were differences between FRET in native tetrameric WT-TTR and ATTR fibrils. FRET analysis was carried out using a combination of absorption spectroscopy and emission spectroscopy, both of which are extensively described in the preparatory specialization project. [15] First, two samples were prepared containing PBS and 0.5 μM of WT-TTR tetramers and ATTR fibrils, respectively. Both absorption and emission of each of the samples

were measured, as well as the background spectra in only PBS. Absorption was measured from 250 – 650nm, while the emission spectra were excited at 278 nm and collected from 290 – 550nm. Then, X34 was added to each of the samples in concentrational intervals, and the absorption and emission spectra measured for each step, until the concentration where the intensity of emission from X34 stopped increasing. The final concentration of X34 was 2 μ M and 4 μ M for tetramers and fibrils, respectively. It was necessary to add a higher concentration of X34 to the fibrils as the emission kept increasing with concentration long after it had stabilized for lower concentrations in the tetramers.

A Stern-Volmer plot was made for both the WT-TTR tetramers and the ATTR fibrils, and the Stern-Volmer quenching constants and bimolecular quenching constants calculated from the plots. The standard errors of the bimolecular quenching constants were calculated using equation (3.2), which was derived from Gauss error propagation, see the preparatory specialization project from fall 2022 for details. [15]

$$\Delta k_q = k_q \sqrt{\left(\frac{\Delta K_D}{K_D}\right)^2 + \left(\frac{\Delta \tau_0}{\tau_0}\right)^2}. \quad (3.2)$$

Here, k_q is the bimolecular quenching constant, K_D the Stern-Volmer quenching constant and τ_0 the lifetime of the fluorophore without the presence of the quencher. Δ denotes the standard error of each of these variables. A similar expression was used for the fluorescence intensity.

3.4 Microscopy

3.4.1 Sample Preparation for CLSM and FLIM

A general staining procedure used for amyloid probes and commercial stains was described in the preparatory specialization project and will not be detailed here. [15] However, all staining involving transfection of ATTR fibrils into cells is new to the Master's thesis, and a general procedure for this can thus be found in this section.

Several imaging sessions were performed using CLSM and FLIM, and the following protocol is the general procedure used to add ATTR fibrils to the cells and stain them. The wavelengths used for excitation and detection of the amyloid probes were found from the photophysics experiments, and are presented in table 3.3. Two different cell lines were used for the CLSM and FLIM experiments, HEK-293 cells and SH-SY5Y cells, with marginally different preparatory protocols.

In addition to the three amyloid probes, three commercial stains were also used to stain various organelles in the cells, for comparison with the localization of the amyloid probes and ATTR fibrils. Each of these stains required a different

Table 3.3: Wavelengths giving maximum absorption and emission in PBS for the three amyloid probes, as found from the photophysics experiments. The excitation wavelength for CLSM was chosen to be as close to the maximum absorption wavelength as possible, and the emission was measured in a ~ 100 nm range around the max emission wavelength.

Dye	Max. Abs. (nm)	Max. Em. (nm)	Ex. wavelength used (nm)
X34	364	505	405
HS335	447	555	405
HS336	462	599	470

amount of incubation time to stain the cells, see table 3.4 for the times provided by the manufacturer, as well as their targets, recommended concentrations and suitable excitation and emission wavelengths. CellMask Deep Red (CM), Deep Red Fluorescing Anthraquinone Nr.5 (DRAQ5) and LysoTracker Deep Red (LT) were all chosen for their far-red emission ranges, as they are far enough from the emission ranges of the amyloid probes to not interfere with their imaging. LT did not stain any of the cells well and photobleached very quickly, and was thus only attempted for one experiment before being rejected for use as a co-stain.

Table 3.4: Suitable excitation and emission wavelengths, as well as suggested incubation times and concentrations by the manufacturer, for the commercial dyes used in CLSM imaging, as provided by the manufacturer.

Dye	Target	Ex. (nm)	Em. (nm)	Incub.	Conc.	Ref
CM Deep Red	Cell membrane	649	699	5 min	1X (1000X stock)	[80]
DRAQ5	Cell nucleus	647	681	5 min	5 – 20 μ M	[81]
LT Deep Red	Lysosomes	647	668	2 h	50nM	[82]

The cells were prepared in an ibidi 8 well for each imaging (figure 3.2), and an example of the layout is displayed in table 3.5 .

Table 3.5: Representative layout of an ibidi 8 well used for imaging the cells. The bottom row here serves as the controls to the cells with added ATTR fibrils in the top row. Concentration of ATTR was varied between 2 – 7 μ M, while ligand concentration was varied between 1 – 7 μ M.

Well 1	Well 2	Well 3	Well 4
SH-SY5Y, HS336 ATTR	SH-SY5Y, X34 ATTR	SH-SY5Y, HS336, ATTR, DRAQ5	SH-SY5Y, X34 ATTR, DRAQ5
Well 5	Well 6	Well 7	Well 8
PBS, HS336, ATTR	SH-SY5Y, HS336	PBS, X34, ATTR	SH-SY5Y, X34

The fibril transfection and staining process was carried out as follows:

1. 15000 cells were seeded into each well in the 8-well ibidi plate. The cells

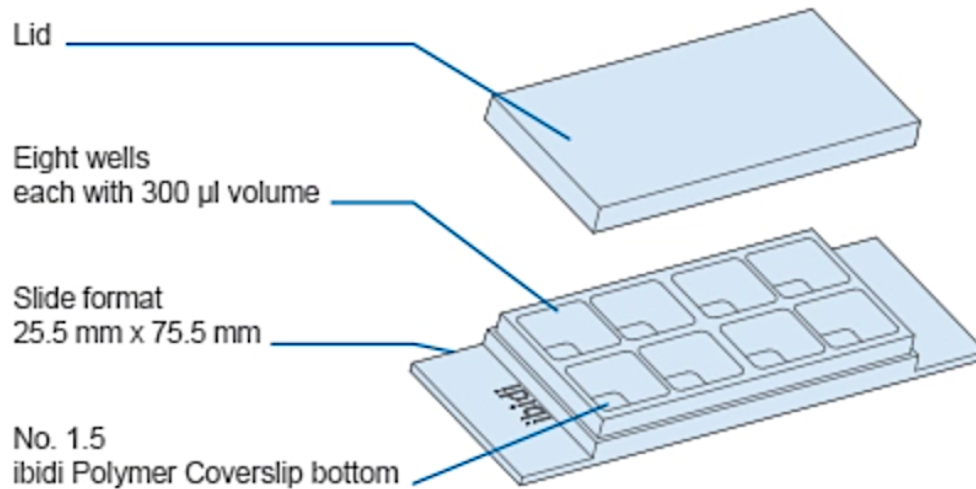


Figure 3.2: The make-up of the ibidi 8 well used in cell imaging, obtained from ibidi's official website. [83]

- were placed in the incubator (37°C, 5% CO₂).
2. After the cells had sufficiently adhered to the wells (usually 5-6 hours), the medium was changed to a serum-free medium. For HEK-293 cells, EMEM medium was used, and for SH-SY5Y EMEM + F-12 (1:1) medium.
 3. The ATTR fibrils and chosen fluorescent amyloid ligands were introduced to the cells. Concentrations of 2 – 7µM of ATTR fibrils and 1 – 7µM of fluorescent amyloid ligands were used, depending on the experiment.
 4. The cells were placed in the incubator (37°C, 5% CO₂), for varying lengths of time depending on the experiment.
 5. In the morning of the day of imaging, the procedure was dependent on the type of commercial stain used.
 - a. For CM and DRAQ5, the cell medium was first removed and discarded. The cells were washed once (100 µL, PBS) and PBS (200 µL) added to each well. Then, the chosen commercial stains were added to their respective wells and incubated for their specified amount of time and recommended concentration, see table 3.4.
 - b. For LT, the stain was added directly to the cell medium in each well. The stain was then incubated for the specified amount of time at the recommended concentration, see table 3.4. After incubation, the cells were washed once (PBS, 100 µL) and PBS (200 µL) was added to each well.
 6. The cells were imaged using a confocal microscope (Leica SP8 SMD/MP Confocal Microscope, Mannheim, Germany).

3.4.2 Confocal Laser Scanning Microscopy (CLSM)

After staining, the cells were imaged using Confocal Laser Scanning Microscopy (CLSM). To minimize photobleaching by the laser, Brightfield (BF) and fluorescence microscopy were used to locate an area with a sufficient number of cells before switching to CLSM. After switching to CLSM, a 405 nm laser was used to excite X34 and HS335, while HS336 and the commercial stains were excited by a White Light Laser (WLL), at the excitation wavelengths outlined in table 3.3 and 3.4, respectively. The probes X34 and HS335 both have their absorption maxima far outside of the range of the WLL (470–670nm), and thus had to be excited with the 405 nm laser. The signal was detected at the respective emission wavelengths of each stain, also summarized in table 3.3 and 3.4. All wells were imaged using the 63x water lens. The microscope was run and the images were processed with the Leica Application Suite X (LAS X) software, using the default setting of 8-bit sampling. When capturing images, the software-recommended number of pixels for the particular area and zoom was used, with a scan speed of 100Hz. The pinhole size was 1 Airy unit, and the gain and laser intensity was adjusted for each scan to have as high intensity as possible without over-saturation of any areas.

Emission scans were also performed using the LAS X software. Excitation was kept at the same wavelength as for imaging for each of the amyloid ligands, and the emission range was set to start 10 nm after the excitation wavelength and continue until around 50 nm past the normal emission range for the ligand. The number of steps was set to be between 35 and 40, using a resolution of 512x512 at a scan rate of 600 Hz. After a completed emission scan, a Region of Interest (ROI) was chosen and the emission spectrum exported to Python. An emission spectrum from the background would also be exported and subtracted from the emission of the ROI. Intensity of emission is not an absolute measurement, so to compare emission scans from two different experiment days, the scans would first be normalized to 1 (See figure 4.24).

3.4.3 Fluorescence Lifetime Imaging Microscopy (FLIM)

Fluorescence Lifetime Imaging Microscopy (FLIM) experiments were performed in parallel with the CLSM experiments, as they utilize many of the same light sources and scanners. However, the software used for FLIM acquisition is SymPhoTime 64 rather than the LAS X. After locating and imaging an area of interest using CLSM, FLIM was performed on the same area. FLIM uses a Single-Photon Avalanche Diodes (SPAD) detector in order to improve the speed of detection. The settings changed for FLIM imaging were opening the pinhole to maximum size, giving an optical section of 5.005 μm , and lowering the scan resolution to 256x256. The scan rate was kept the same at 100Hz. Each FLIM scan was run until the total number of counts collected from each pixel reached 1000.

Each FLIM image will have two corresponding color bars, a grayscale bar showing

the intensity in number of counts and a full-color bar showing the lifetime in ns. The default range given by the program for each individual sample was used for both of these bars.

After the acquisition was complete, a double exponential tail-fit was performed on the decay to find the fluorescence lifetime and the data was exported to Python for plotting and further processing.

Chapter 4

Results

The results are presented in two main sections. (4.1 and 4.2) Section 4.1 contains the photophysics results, starting with the screening of potential amyloid ligands. Then, the photophysical study of the three chosen amyloid ligands, X34, HS335 and HS336, is detailed, including their absorptive and emissive properties, quantum yields (QY) and fluorescence lifetimes. Finally, the binding of native WT-TTR tetramers and ATTR fibrils to the ligand X34 is studied through Fluorescence Resonance Energy Transfer (FRET) and fluorescence decay measurements.

Section 4.2 details the spectroscopic study of the ATTR based cell models, showing the interaction of fibrils with the two cell lines HEK-293 and SH-SY5Y and the three fluorescent amyloid ligands via CLSM and FLIM images. Emission spectra and fluorescence lifetimes of the ligands in cells are also included for comparison to the results from the photophysics study.

4.1 Photophysics

4.1.1 Tecan Microplate Reader

Screening of Potential Amyloid Ligands

Out of the eight fluorescent amyloid ligands, three probes were chosen to continue with, because of their promising results. These were X34, HS335 and HS336, and their emission spectra with and without ATTR fibrils at pH 2 and 7.4 are shown in figure 4.1, 4.2 and 4.3, respectively. The excitation wavelength giving the highest emission was chosen for each probe, and each measurement was made directly after sample preparation and once again 24 h later. Since the same settings (slits, gain, etc.) were used for all samples, see section 3.3.3, the measured emission intensity can be compared across samples. The selection criteria were to have a high intensity at pH 7.4 and a large difference between the intensity from the probes bound to the ATTR fibrils and the probes by themselves. The probe bTVBT-

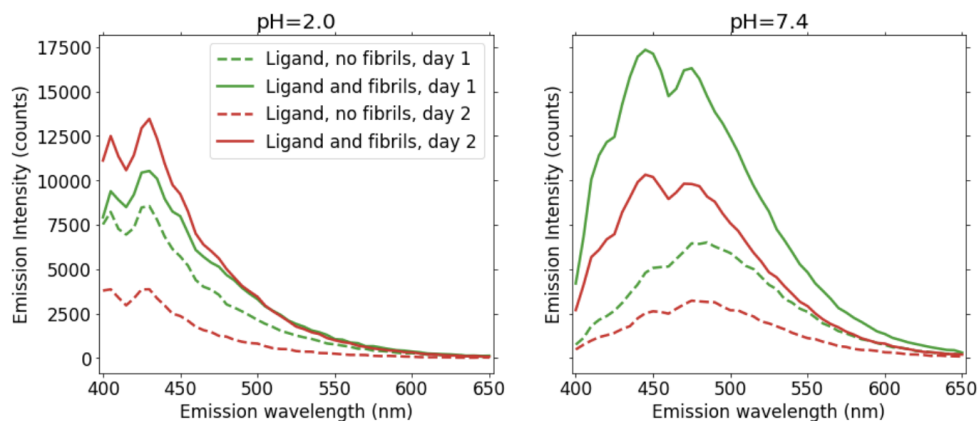


Figure 4.1: Emission spectra of X34 at pH 2 and 7.4, measured using a Tecan microplate reader immediately after sample preparation and once again 24 h later. ($\lambda_{\text{ex}} = 373 \text{ nm}$) The various samples are indicated by the inset in the left panel. All spectra were baseline corrected by data with buffer only. See section 3.3.3 for sample composition.

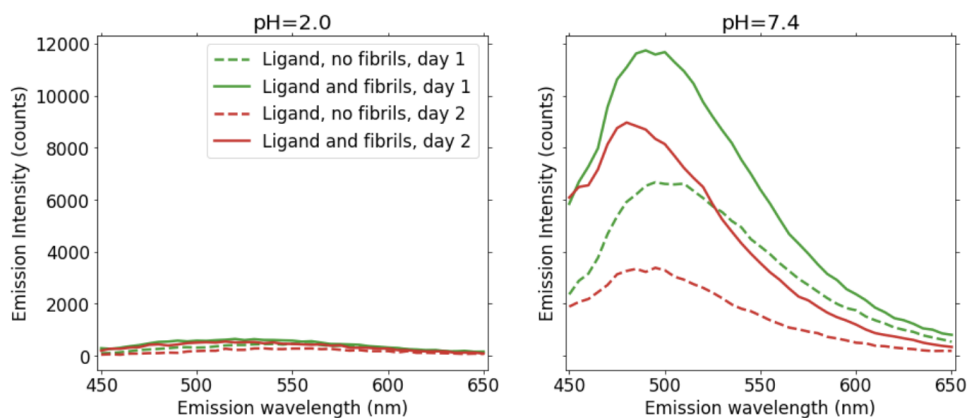


Figure 4.2: Emission spectra of HS335 at pH 2 and 7.4, measured using a Tecan microplate reader immediately after sample preparation and once again 24 h later. ($\lambda_{\text{ex}} = 405 \text{ nm}$) The various samples are indicated by the inset in the left panel. All spectra were baseline corrected by data with buffer only. See section 3.3.3 for sample composition.

Tyr was deemed to be a potential backup probe, and the probe ThT was suitable for comparison due to being a standard amyloid ligand. The remaining probes were rejected due to too small difference between the intensity of free ligand in solution and ligand bound to ATTR fibrils. The spectra of the probes not chosen to proceed with are shown in appendix A.

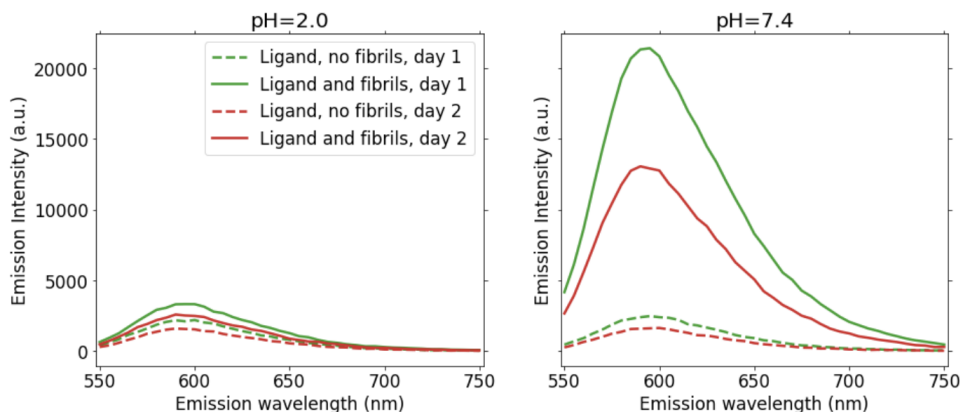


Figure 4.3: Emission spectra of HS336 at pH 2 and 7.4, measured using a Tecan microplate reader immediately after sample preparation and once again 24 h later. ($\lambda_{\text{ex}} = 535 \text{ nm}$) The various samples are indicated by the inset in the left panel. All spectra were baseline corrected by data with buffer only. See section 3.3.3 for sample composition.

Plate Reader Binding Curves

The ligands X34 and HS336 were chosen for further investigation. The binding curves of HS336 alone and bound to WT-TTR tetramers and ATTR fibrils are shown in figure 4.4, giving the total intensity of emission as a function of ligand concentration. Two identical samples were made for each TTR type as well as the blank, and the binding curve gives the average of the total intensity of emission for the two samples. The intensity is highest for all concentrations for HS336 with ATTR fibrils for both day 1 and 2, with HS336 with the WT-TTR tetramers having a slightly lower intensity. The emission of HS336 alone shows a significantly lower intensity than when bound to TTR. The binding curves of the ATTR fibrils on day 1 and 2 both show a substantial peak in intensity around 1000 nM, before adopting a more linear rising trend, closer to that of tetramers and blank samples, at higher concentrations. As all the samples exhibit a similar linear trend, this is likely an increase in emission by an increasing concentration of free HS336 in solution, rather than the added HS336 binding to ATTR or WT-TTR.

The binding curves of X34 bound to ATTR and WT-TTR are shown in figure 4.5. Three identical samples were made for each TTR type as well as two identical samples for the blank, and the binding curve gives the average of the total intensity of emission for these samples. Unlike HS336, the intensity from X34 bound to the native tetramers is higher than the intensity of ATTR between $\sim 100 - 1000 \text{ nM}$. This decrease in the intensity of X34 bound to WT-TTR can be explained by the two ligand binding sites on each WT-TTR tetramer. Upon binding of a second X34 molecule to a WT-TTR molecule, X34 will experience self-quenching and the total intensity will decrease as more TTR molecules bind a second X34 molecule. The

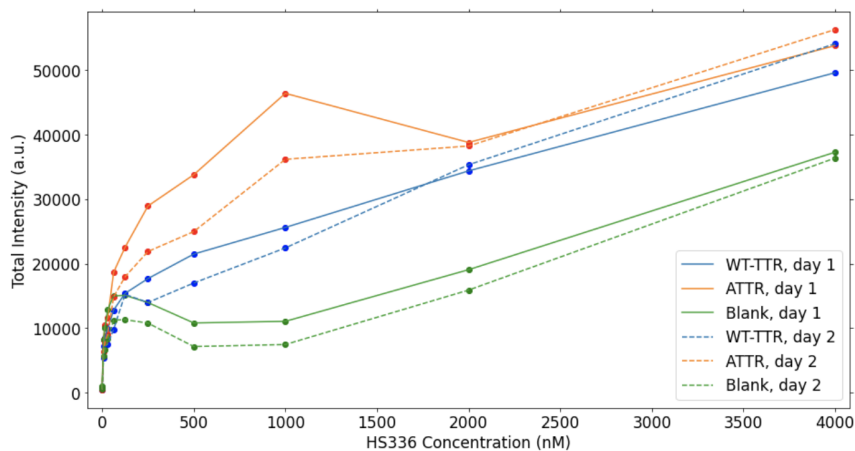


Figure 4.4: Binding curve of HS336, plotted as concentration of HS336 against total intensity for WT-TTR tetramers ($0.5 \mu\text{M}$), ATTR fibrils ($0.5 \mu\text{M}$) and blank samples. ($\lambda_{\text{ex}} = 535 \text{ nm}$, $\lambda_{\text{em}} = 550 - 750 \text{ nm}$) Similarly to the general probe investigations using the plate reader, results were collected on the day of sample preparation and 24 h later.

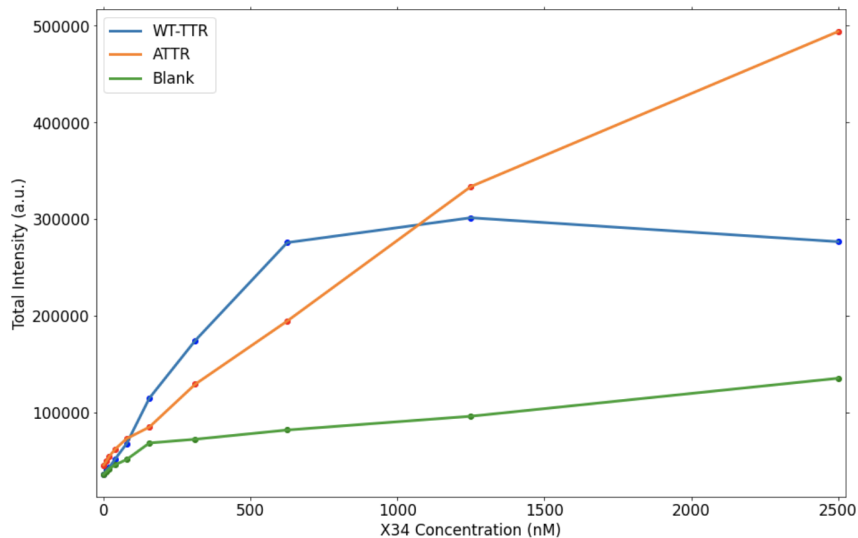


Figure 4.5: Binding curve of X34, plotted as concentration of X34 against total intensity for WT-TTR tetramers ($0.5 \mu\text{M}$), ATTR fibrils ($0.5 \mu\text{M}$) and blank samples. ($\lambda_{\text{ex}} = 373 \text{ nm}$, $\lambda_{\text{em}} = 400 - 620 \text{ nm}$) Only one measurement was performed on X34, directly after sample preparation.

binding sites of ATTR are less understood, but there is likely to be self-quenching also here if any X34 molecules bind close to each other, in analogy with the WT-TTR tetramer. The binding of X34 to ATTR and WT-TTR and the quenching dynamics of these processes are further explored in the FRET experiments, see

section 4.1.5.

4.1.2 Quantum Yield

Absorption and emission spectra of X34 in various solvents are displayed in figure 4.6 and the measured absorption and emission maxima are summarized in table 4.1. Chloroform and THF gave short Stokes shifts compared to the rest of the solvents, while PBS and MeCN imposed longer shifts. DMSO gave X34 a clear red-shift compared to the other solvents, while THF and CHCl_3 resolved a distinct blue-shifted double-peak in their emission spectra. The molar extinction coefficients are also tabulated in table 4.1, and are relatively close in value for all solvents.

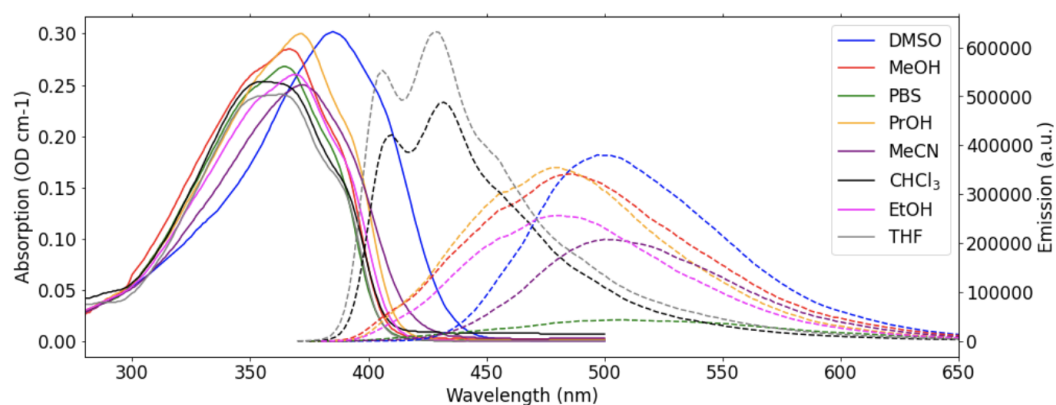


Figure 4.6: Absorption and emission spectra of X34 in eight different solvents. The wavelength giving the maximum absorption was used as the excitation wavelength for the emission spectra, see table 4.1. Absorption spectra are solid lines, while the emission spectra are the dotted lines in corresponding colors. Concentration was $5 \mu\text{M}$ of X34 for all eight solvents. Four of the solvents stand out from the other four. PBS stands out in that it gives a much lower emission compared to the other solvents, DMSO gives a clear red-shift in both absorption and emission, and both THF and CHCl_3 give a distinct double-peak for emission.

As some solvents have similar properties as judged from the results, four solvents were selected for more detailed studies with HS335 and HS336.

- MeOH, EtOH and PrOH give quite similar absorption and emission graphs, and thus only MeOH was chosen for further use.
- CHCl_3 and THF give a similar double-peaked emission, and hence only CHCl_3 was chosen for further experiments.
- PBS is interesting both because of the low intensity of emission it gives X34 and because of its pH of 7.4, making it similar to the cellular environment.
- DMSO is interesting because of the clear red-shift it gives X34.

To summarize, $\text{CHCl}_3/\text{THF} \rightarrow \text{CHCl}_3$, $\text{PBS} \rightarrow \text{PBS}$, $\text{MeOH}/\text{EtOH}/\text{PrOH} \rightarrow \text{MeOH}$,

Table 4.1: Absorption and emission maxima, as well as Stokes shifts and extinction coefficients (ϵ) for X34 in various solvents, sorted from shortest to longest wavelength for the absorption maximum.

Solvent	Abs. Max. (nm)	Em. Max. (nm)	Stokes Shift (nm)	ϵ ($M^{-1}cm^{-1}$)
$CHCl_3$	353	432	79	50600
THF	362	428	66	48200
PBS	364	505	141	53600
EtOH	368	480	112	52000
MeOH	368	485	117	57000
PrOH	371	479	108	60000
MeCN	371	500	129	50000
DMSO	385	497	112	60400

MeCN/DMSO \rightarrow DMSO.

Absorption and emission spectra of HS335 and HS336 are shown in figure 4.7 and 4.8, respectively. Their absorption and emission maxima, as well as Stokes shifts, are summarized in table 4.2 and 4.3, respectively. None of the spectra have the double-peaked emission shown for X34 in $CHCl_3$ and THF. The absorption spectrum of HS335 in PBS stands out from all the other spectra, and could indicate that HS335 has not dissolved well in PBS. For HS335, DMSO gives a slight red-shift, like with X34, but less distinct, and does not seem red-shifted for HS336. For HS336, PBS seems to give a blue-shifted absorption spectrum, while $CHCl_3$ gives a red-shift in absorption. This points to HS336 exhibiting anomalous solvatochromism, as described in section 2.2.4, where the fluorophore will experience a red-shift for less polar solvents and a blue-shift for more polar solvents, caused by the ground state being more polar than the excited state. The molar extinction coefficients of HS335 and HS336 are also summarized in table 4.2 and 4.3. The values for HS335 are significantly higher than those calculated for X34, and both HS335 and HS336 show larger variations in coefficients between different solvents than X34. For HS335, PBS gives a much lower extinction coefficient, likely a consequence of the unusual absorption spectrum of HS335 in PBS. HS336 has a slightly higher extinction coefficient in DMSO compared to in PBS and MeOH, and a significantly higher value in $CHCl_3$.

The quantum yields of X34, HS335 and HS336 in various solvents are summarized in table 4.4. For X34, there is a large variation in magnitude of quantum yield between solvents, with the lowest being 4.9% for PBS, while THF gives the highest QY: 43.5%. HS335 and HS336 both seem to have a smaller variation in QY between solvents, ranging from 0.2% to 3.2%. HS335 has its highest QY in PBS at 1.4%, while HS336 has its highest QY in DMSO at 3.2%. There seems to be a correlation between the length of the Stokes shift and size of the QY for X34, with THF and $CHCl_3$ giving the shortest Stokes shifts and highest QYs. At pH 2.0, QY is further decreased to be below 1% for all three probes, in accordance with the plate reader

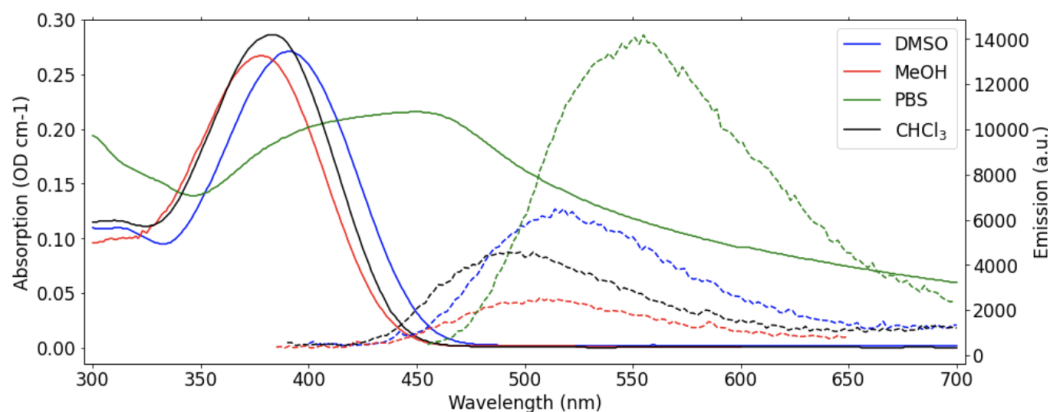


Figure 4.7: Absorption and emission spectra of HS335 in four different solvents, chosen for their interesting results with X34. The wavelength giving the maximum absorption was used as excitation wavelength for the emission spectra, see table 4.2. The absorption in PBS has a very different shape compared to the other solvents, possibly indicating that HS335 has not dissolved well. It also gives the highest intensity of emission, in stark contrast to X34 having its lowest intensity of emission in PBS. DMSO once again shows a red-shift, but less distinct than for X34. CHCl_3 does not give a double-peaked emission like for X34. Concentration of HS335 is $1.67 \mu\text{M}$ for all solvents except PBS ($2.5 \mu\text{M}$).

Table 4.2: Absorption and emission maxima for HS335 in various solvents, sorted from shortest to longest wavelength for the absorption maximum. PBS gives an absorption maximum at much longer wavelength than the other solvents, and a much smaller molar extinction coefficient.

Solvent	Abs. Max. (nm)	Em. Max. (nm)	Stokes Shift (nm)	ϵ ($\text{M}^{-1}\text{cm}^{-1}$)
MeOH	377	507	130	159900
CHCl_3	381	504	123	171200
DMSO	390	518	128	162300
PBS	447	555	108	86400

Table 4.3: Absorption and emission maxima for HS336 in various solvents, sorted from shortest to longest wavelength for the absorption maximum. PBS has an absorption maximum at much shorter wavelength than the other solvents.

Solvent	Abs. Max. (nm)	Em. Max. (nm)	Stokes Shift (nm)	ϵ ($\text{M}^{-1}\text{cm}^{-1}$)
PBS	462	599	137	59600
MeOH	498	600	102	64000
DMSO	499	608	109	84100
CHCl_3	537	602	65	103600

results in figures 4.1-4.3. In these cases, the errors are relatively large.

Representative spectra and plots for calculating QY are presented in appendix B.

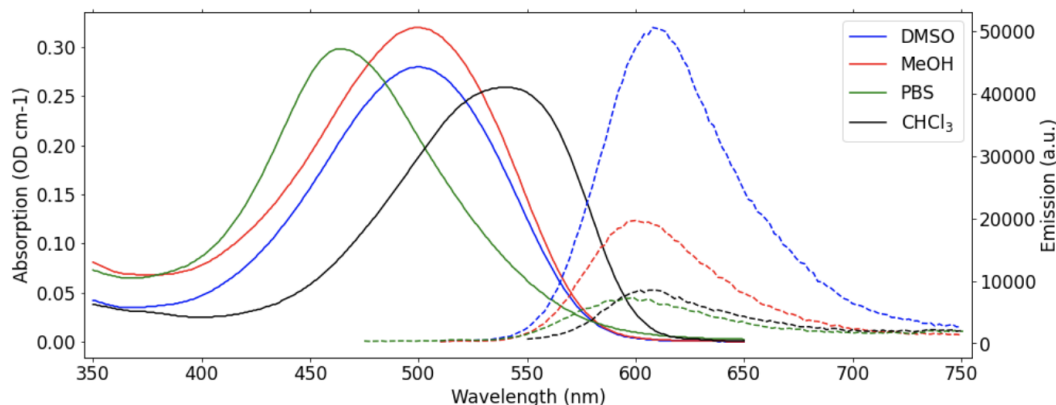


Figure 4.8: Absorption and emission spectra of HS336 in four different solvents, chosen for their interesting results with X34. The wavelength giving the maximum absorption was used as excitation wavelength for the emission spectra, see table 4.3. PBS gives a blue-shifted absorption curve, while CHCl_3 gives a red-shifted curve. PBS seems to have a slight blue-shift in emission as well, compared to the other three solvents. CHCl_3 does not give a double-peaked emission like for X34. Concentration of HS336 is $5 \mu\text{M}$ for MeOH and PBS, $3.33 \mu\text{M}$ for DMSO and $2.5 \mu\text{M}$ for CHCl_3 .

Table 4.4: Quantum yield for X34, HS335 and HS336 in various solvents. X34 has a higher QY in all solvents than HS335 and HS336.

Solvent	X34 (%)	HS335 (%)	HS336 (%)
MeOH	27.9 ± 2.11	0.2 ± 0.04	0.9 ± 0.10
PBS	4.9 ± 0.58	1.4 ± 0.55	0.4 ± 0.13
CHCl_3	33.9 ± 2.61	0.5 ± 0.08	0.6 ± 0.08
DMSO	30.9 ± 2.16	0.7 ± 0.11	3.2 ± 0.35
MeCN	17.6 ± 1.37	-	-
EtOH	22.6 ± 1.54	-	-
THF	43.5 ± 4.29	-	-
PrOH	27.1 ± 1.97	-	-
pH 2.0	0.1 ± 0.01	0.1 ± 0.01	0.6 ± 0.08

For procedure, see Rurack and Spieles (2011). [76]

4.1.3 Fluorescence Lifetime

The fluorescence decay times in solvents were investigated with the Time-Correlated Single Photon Counting (TCSPC) technique, see section 2.2.3. The lifetimes of X34, HS335 and HS336 in various solvents, all fitted to single exponential equations, are presented in table 4.5. For X34, CHCl_3 and THF gave considerably longer lifetimes than the other solvents, and PBS gave the shortest lifetime. This indicates a correlation between magnitude of the QY and length of

the fluorescence lifetime for X34, given that THF and CHCl_3 also gave the largest QY for X34, whereas PBS the smallest.

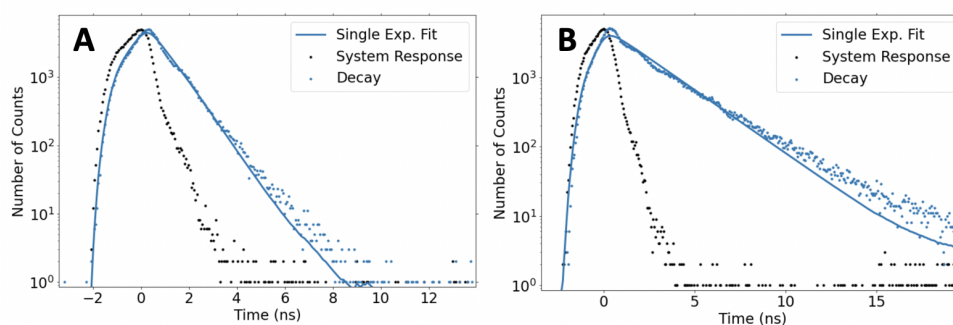


Figure 4.9: The fluorescence lifetime of X34 in (A) MeOH ($\lambda_{\text{ex}} = 373\text{nm}$, $\lambda_{\text{em}} = 490\text{nm}$) and (B) CHCl_3 ($\lambda_{\text{ex}} = 373\text{nm}$, $\lambda_{\text{em}} = 432\text{nm}$), both fitted to a single exponential equation. The lifetime is considerably longer in CHCl_3 .

The visual difference between long and short lifetimes is demonstrated by X34 in CHCl_3 and MeOH in figure 4.9. PBS also gives the shortest lifetime for HS336, while for HS335 it gives a much longer lifetime than all the other solvents. HS335 has very short lifetimes in other solvents, with CHCl_3 being the shortest at only $20\text{ps} \pm 17$. This is a very large error for such a short lifetime, likely due to the resolution limit of the instrument being around 100 ps. HS336 has slightly longer lifetimes than HS335, however they are still in the 100 ps range and thus close to the limit of the instrument. Overall, both HS335 and HS336 have considerably shorter lifetimes than X34 for all solvents, except for HS335 in PBS. See appendix C for selected additional lifetime decay plots.

Table 4.5: Fluorescence lifetime for X34, HS335 and HS336 in various solvents, calculated as single exponential fit. X34 has much longer lifetimes than HS335 and HS336 for all solvents, except for HS335 in PBS. CHCl_3 and THF give X34 particularly long lifetimes.

Solvent	X34 (ps)	HS335 (ps)	HS336 (ps)
PBS	260 ± 22	770 ± 19	100 ± 12
MeOH	560 ± 8	40 ± 24	110 ± 7
DMSO	880 ± 8	80 ± 20	160 ± 10
CHCl_3	2360 ± 23	20 ± 17	150 ± 23
EtOH	720 ± 11	-	-
MeCN	740 ± 7	-	-
PrOH	760 ± 9	-	-
THF	1920 ± 15	-	-

4.1.4 Photophysical Properties of X34 Bound to Insulin and ATTR Fibrils

A photophysical study was performed on X34 bound to both insulin and ATTR fibrils, as insulin fibrils are one of the most intensively studied amyloid-forming proteins and can function as a comparison to the ATTR fibrils. Excitation and emission spectra were collected for 5 μM X34 bound to 7.1 μM of both fibril types in PBS, as well as spectra of X34 in PBS. These are displayed in figure 4.10. The intensity increases significantly for both spectra when bound to both fibril types compared to in solution, as well as showing a slight shortening of the Stokes shift for both fibril types.

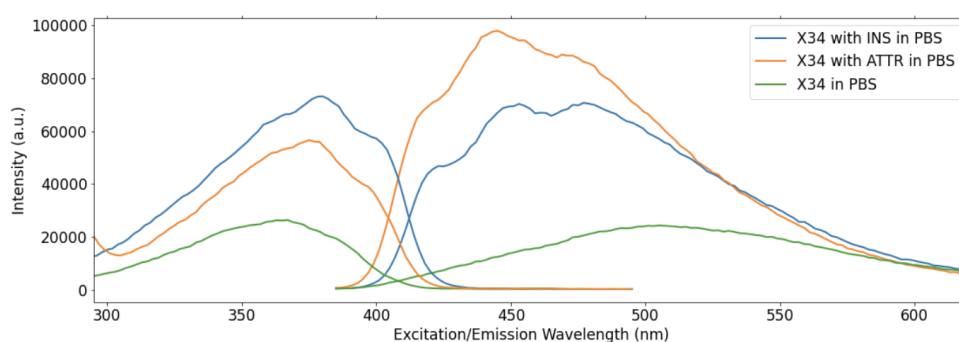


Figure 4.10: Excitation and emission spectra of 5 μM X34 in PBS, alone and bound to 7.1 μM ATTR and insulin fibrils. The intensity of emission of X34 increases significantly with both insulin fibrils and ATTR fibrils, however the intensity of emission from X34 bound to ATTR fibrils is distinctly larger. (Excitation scan: ($\lambda_{\text{ex}} = 295 - 495\text{nm}$, $\lambda_{\text{em}} = 505\text{nm}$) for ATTR and blank, ($\lambda_{\text{ex}} = 270 - 470\text{nm}$, $\lambda_{\text{em}} = 480\text{nm}$) for insulin) (Emission scan: ($\lambda_{\text{ex}} = 373\text{nm}$, $\lambda_{\text{em}} = 485 - 785\text{nm}$). As the emitted light in the excitation scan of ATTR was measured at $\lambda_{\text{em}} = 505\text{nm}$, where the emission of ATTR is much lower than the maximum emission, the measured excitation spectrum is likely falsely low.

The fluorescence lifetimes of X34 bound to insulin and ATTR fibrils in PBS were also measured, see figure 4.11. There was a significant increase in the lifetime of X34 when bound to both ATTR and insulin compared to in solution, see table 4.6. The lifetime is longest when bound to ATTR fibrils.

Table 4.6: Fluorescence lifetimes of X34 alone and with ATTR and insulin fibrils in PBS. The lifetime becomes considerably longer with the addition of both fibril types, but the lifetime is longest when bound to ATTR.

Sample	Lifetime (ps)
X34	260 ± 22
X34 + ATTR	1520 ± 15
X34 + Insulin	1210 ± 3

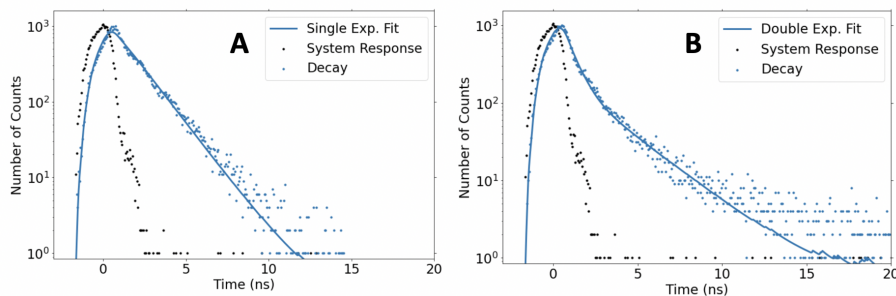


Figure 4.11: The fluorescence lifetime of X34 with (A) ATTR ($\lambda_{\text{ex}} = 373\text{nm}$, $\lambda_{\text{em}} = 450\text{nm}$) and (B) insulin fibrils ($\lambda_{\text{ex}} = 373\text{nm}$, $\lambda_{\text{em}} = 490\text{nm}$), both in PBS. X34 bound to insulin fibrils was fitted to a double exponential expression as it could not be fitted well to a single exponential expression, while X34 bound to ATTR fit well with a single exponential expression.

4.1.5 Fluorescence Resonance Energy Transfer (FRET)

Fluorescence Resonance Energy Transfer (FRET) experiments were performed to see if there were differences between the FRET in native WT-TTR tetramers and ATTR fibrils. There was such a difference, indicating that the ATTR fibrils are still amyloidic and have not re-folded back into native tetramers upon exposure to room temperature and a raise in pH to 7.4, see section 2.1.5.

The FRET spectra of X34 bound to WT-TTR tetramers and ATTR fibrils are shown in figure 4.12. The first peak of the absorption spectra corresponds to the absorbance of Tryptophan (Trp) in the TTR ($\lambda_{\text{abs}} \sim 280\text{nm}$), and it is fairly constant with the addition of X34 for both tetramers and fibrils. The second absorption peak corresponds to the absorption of X34 ($\lambda_{\text{abs}} \sim 365\text{nm}$), both in solution and bound to TTR, and thus increases with increasing concentration of the ligand. The first emission peak corresponds to the fluorescence of Trp in the TTR molecules ($\lambda_{\text{em}} \sim 330\text{nm}$), while the second broader emission band corresponds to the fluorescence of X34 bound to TTR ($\lambda_{\text{em}} \sim 440 - 480\text{nm}$), and their intensity decreases and increases with addition of X34, respectively. The Trp-fluorescence of the TTR is thus quenched with the addition of X34.

The fluorescence of X34 bound to TTR eventually reaches a maximum at around $0.4\mu\text{M}$ for tetramers, and around $3.5\mu\text{M}$ for fibrils. The Trp-fluorescence has $\lambda_{\text{em,max}} \sim 335\text{nm}$ for the ATTR fibrils and $\lambda_{\text{em,max}} \sim 330\text{nm}$ for the WT-TTR tetramers, while X34 has an emission maximum at $\lambda_{\text{em,max}} \sim 440\text{nm}$ when bound to ATTR fibrils and at $\lambda_{\text{em,max}} \sim 470\text{nm}$ when bound to WT-TTR tetramers, a significant difference. Similar spectral shifts were observed for the plate reader data of figure 4.5 (spectra not shown).

The lifetimes of Trp in WT-TTR tetramers and ATTR fibrils alone and with the addition of two concentrations of X34 are summarized in table 4.7, and their decays in figure 4.13. To better demonstrate that the average lifetime upon

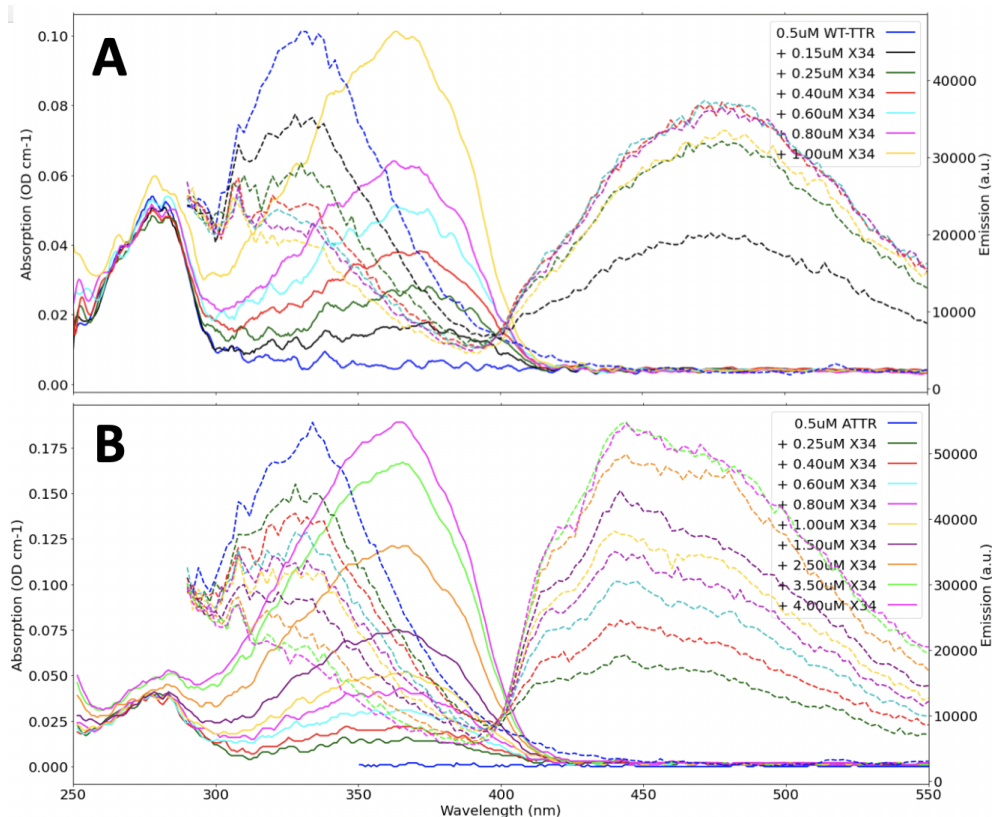


Figure 4.12: Absorption and emission of (A) WT-TTR tetramers and (B) ATTR fibrils, alone and with various concentrations of X34. The colors of the corresponding absorption and emission spectra are the same, with emission signified by a dotted line. $\lambda_{\text{ex}} = 278$ nm for the emission spectra.

Table 4.7: Fluorescence lifetime of WT-TTR tetramers and ATTR fibrils alone and with two concentrations of X34, presented as both the individual lifetime components of the double exponential fit (τ_1 , τ_2) with their relative amplitudes (a_1 , a_2), as well as the average lifetime calculated from these ($\bar{\tau}$). Because of a difference in step size, $0.75 \mu\text{M}$ X34 was added to the tetramers, and $0.8 \mu\text{M}$ X34 to the fibrils. The lifetimes decrease with added concentration of X34.

WT-TTR	τ_1 (ps) (a_1 (%))	τ_2 (ps) (a_2 (%))	$\bar{\tau}$ (ps)
Trp only	3240 ± 19	-	3240 ± 19
+0.75 μM X34	3240 (fixed) (47.10)	980 ± 22 (52.90)	2040 ± 22
+2.0 μM X34	3240 (fixed) (19.63)	1050 ± 16 (80.37)	1480 ± 16
ATTR	τ_1	τ_2	$\bar{\tau}$
Trp only	3280 ± 29	-	3280 ± 29
+ 0.8 μM X34	3280 (fixed) (66.42)	860 ± 22 (33.58)	2470 ± 22
+ 2.0 μM X34	3280 (fixed) (50.59)	930 ± 17 (49.41)	2120 ± 17

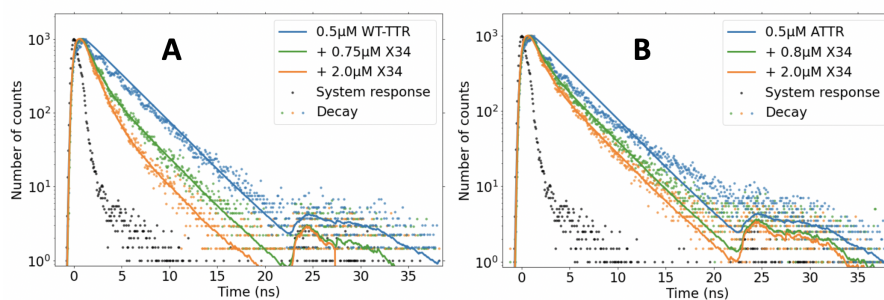


Figure 4.13: (A) The fluorescence lifetime of Trp in 0.5 μM ATTR fibrils alone and with two concentrations of X34, 0.8 μM and 2.0 μM . (B) The fluorescence lifetime of Trp in 0.5 μM WT-TTR tetramers alone and with two concentrations of X34, 0.75 μM and 2.0 μM . The exponential fits were calculated as single exponential decays before addition of X34, and double exponential decays for samples with X34. The lifetimes decrease with addition of higher concentrations of X34. ($\lambda_{\text{ex}} = 278\text{nm}$, $\lambda_{\text{em}} = 340\text{nm}$) The "wiggles" observed for some traces are interference due to a misalignment of the detector system.

addition of X34 will be a weighted average of the unquenched lifetime of Trp and the shortened lifetime of the quenched Trp molecules, the lifetimes are presented as a fixed component equal to the unquenched lifetime and an unfixed component affected by the added concentration of X34. The lifetimes of Trp in WT-TTR tetramers and ATTR fibrils are fairly similar before addition of X34, at $3240\text{ps} \pm 19$ and $3280\text{ps} \pm 29$, respectively. Both lifetimes also decrease with the addition of higher concentrations of X34, but the lifetime change of the ATTR fibrils appears to be smaller.

To investigate the quenching dynamics of the WT-TTR tetramers and ATTR fibrils, Stern-Volmer quenching plots were calculated for the two cases ATTR and WT-TTR, see figure 4.14. The theory behind Stern-Volmer plots were described in section 2.2.4. Each of the samples were fitted to two separate linear functions. Ranges: 0.0–0.8 μM and 1.5–4.0 μM for ATTR, 0.0–0.75 μM and 1.0–2.0 μM for WT-TTR. This produces two better fits than if all the data points for each sample were attempted fitted to the same linear function. Both samples have a significant shift in the slope between these linear functions. The fluorescence lifetimes of each sample were also plotted and are possibly following the same pattern of a shift in linearities as the intensities, however, a more thorough analysis of the lifetimes with more data points is needed to make similar plots.

It is hypothesized that the shift in linearity could be due to the two ligand binding sites on the TTR molecule, see figure 4.15, with the shift between the two functions corresponding to the shift from filling the first binding site to the second. Upon binding of a second X34 molecule, the Trp molecule is already quenched from the first binding event, and thus the decrease in intensity of emission will be smaller, resulting in a linear function with a lower slope. This shift from X34 binding to the

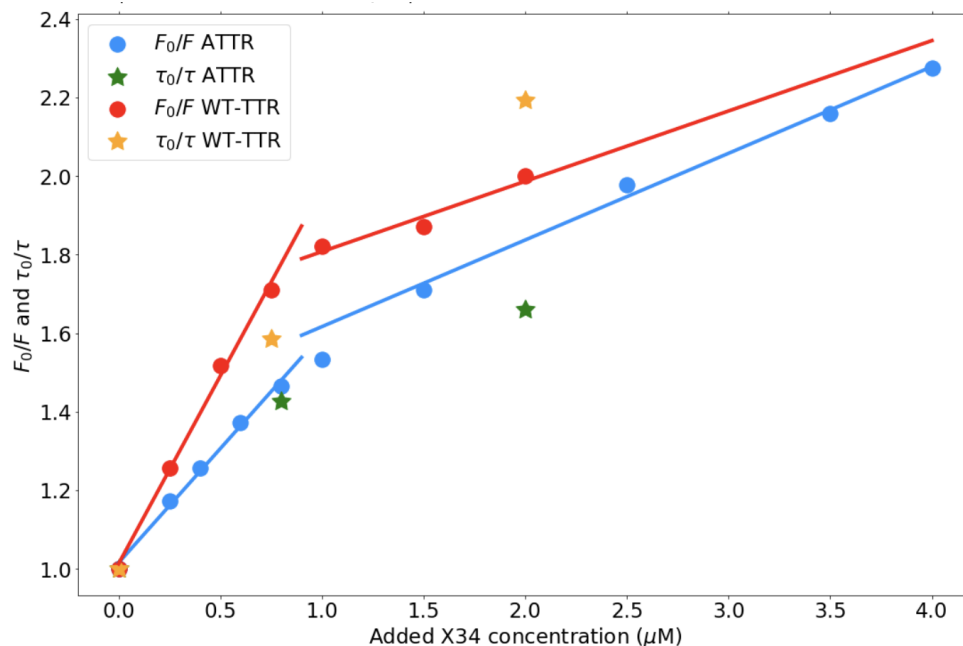


Figure 4.14: Stern-Volmer quenching plot for the quenching of Trp-fluorescence and shortening of the fluorescence lifetime in WT-TTR tetramers and ATTR fibrils with the addition of X34. Each of the samples were fitted to two distinct linear functions, shown in solid lines of corresponding color. The r^2 values of the linear fits are 0.99432/0.99334 and 0.99553/0.93773 for the ATTR and WT-TTR, respectively.

first binding site to the second seems to take place slightly below 1 μM for both ATTR and WT-TTR.

Two bimolecular quenching constants were calculated for each of the samples, corresponding to each of the linear fits, see table 4.8. The tetramers have a significantly higher value for the first process at low ligand concentration, while the bimolecular constant for ATTR is slightly higher for the higher ligand concentration. As k_q is smaller than $1 \cdot 10^{10} \text{M}^{-1} \text{s}^{-1}$ for both samples, there is likely to be either low quenching efficiency or some shielding of the fluorophore, as discussed in section 2.2.4. [56]

Table 4.8: Bimolecular quenching constants (k_{q1} and k_{q2}), calculated from the two linear fits for native WT-TTR tetramers and ATTR fibrils. The tetramers have a significantly higher value for the first process at low ligand concentration, while the bimolecular constant for ATTR is slightly higher for the higher ligand concentration.

TTR type	k_{q1} ($10^7 \text{M}^{-1} \text{s}^{-1}$)	k_{q2} ($10^7 \text{M}^{-1} \text{s}^{-1}$)
WT-TTR Tetramers	29.5 ± 1.40	5.5 ± 1.43
ATTR Fibrils	16.8 ± 0.73	6.4 ± 0.37

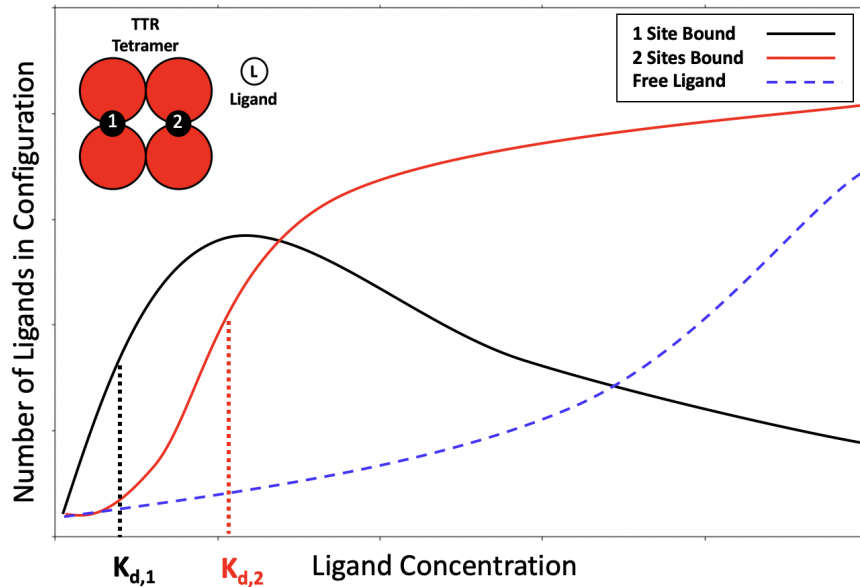


Figure 4.15: A cartoon visualization of a two-site model for tetrameric TTR. Each TTR molecule consists of four subunits, forming two binding sites for protein ligands. As detailed in section 2.1.5, the binding of ligands to these sites is poorly understood, but it is hypothesized that the ligands will first bind to the first binding site, and only begin binding to the second site once the first is close to saturation, with inferable $K_{d,1} < K_{d,2}$. The number of molecules with only one bound ligand will obviously decrease with the increase of molecules with two ligands bound, as shown schematically in the figure.

4.2 Confocal Laser Scanning Microscopy (CLSM)

This section is divided into three parts. Section 4.2.1 contains a comparison of ATTR fibrils to insulin fibrils, performed in order to get visual reference of the ATTR fibrils and compare them to the structure of insulin fibrils, as well as to see whether there are any differences in how the amyloid ligands bind ATTR and insulin fibrils. This comparison was made *in vitro* in PBS and using HEK-293 cells.

The second part, section 4.2.2, details a time-based incubation trial performed with X34 and ATTR fibrils in HEK-293 cells, in order to find the optimal incubation time for use in subsequent experiments.

Finally, sections 4.2.3, 4.2.4 and 4.2.5 contain detailed analyses of X34, HS335 and HS336 in both cell lines with and without ATTR, including CLSM and FLIM images, emission spectra and fluorescence lifetimes.

4.2.1 Comparing Insulin and ATTR Fibrils

Comparison of Insulin and ATTR fibrils in PBS

Before starting the work on introducing the ATTR fibrils to cells, 7 μM ATTR fibrils in PBS were stained using 7 μM HS335 and 7 μM X34 in order to see the staining capabilities of the ligands as well as visualize the structure of the fibrils. Both probes were also added to 7 μM insulin fibrils, in order to have a comparison to amyloid fibrils with a well-characterized structure to see whether the amyloid ligands bind the fibril types in different ways. Insulin is known to be polymorphic, commonly producing amyloids with two main morphologies, flexible filamentous amyloids and structured fibrillar amyloids, see section 2.1.6, as well as Yuzu et al. (2020) for examples of visualization of this polymorphism using fluorescent amyloid ligands. [50]

CLSM images of 7 μM ATTR and insulin fibrils stained with 7 μM X34 or HS335, as well as 7 μM X34 or HS335 in PBS without any fibrils, are shown in figure 4.16. The probe X34 seems to evenly and intensely stain both fibril types, and there is a significant increase in intensity from that of free probe (A) when bound to ATTR (C) and insulin fibrils (E). The even staining makes it possible to compare the two amyloid types. The insulin fibrils used are of the fibrillar type, and compared to these, the ATTR fibrils appear to be a smaller, more filamentous type of amyloids. HS335 also shows a large difference in intensity of emission between free probe (B) and when bound to ATTR (D). The probe appears to stain ATTR fibrils intensely and evenly, while the insulin fibrils (F) appear less efficiently stained apart from a few bright spots. This could be related to the solubility issues for HS335 in PBS seen in the photophysics experiments, see section 4.1.2. Overall, X34 seems to bind more evenly and discern the structure of both fibril types better, while HS335 gives a larger change in intensity of emission upon binding.

The emission spectra of both 7 μM X34 and HS335 corresponding to the images in figure 4.16 are displayed in figure 4.17. HS335 shows a large increase in emission intensity when bound to both ATTR and insulin, and a red-shift when bound to insulin. X34 on the other hand, shows a smaller increase in intensity when bound to ATTR and insulin, but a clear red-shift in emission wavelength for both fibril types. One of the insulin samples gives a great intensity increase for X34, while the other has the same intensity as X34 in PBS.

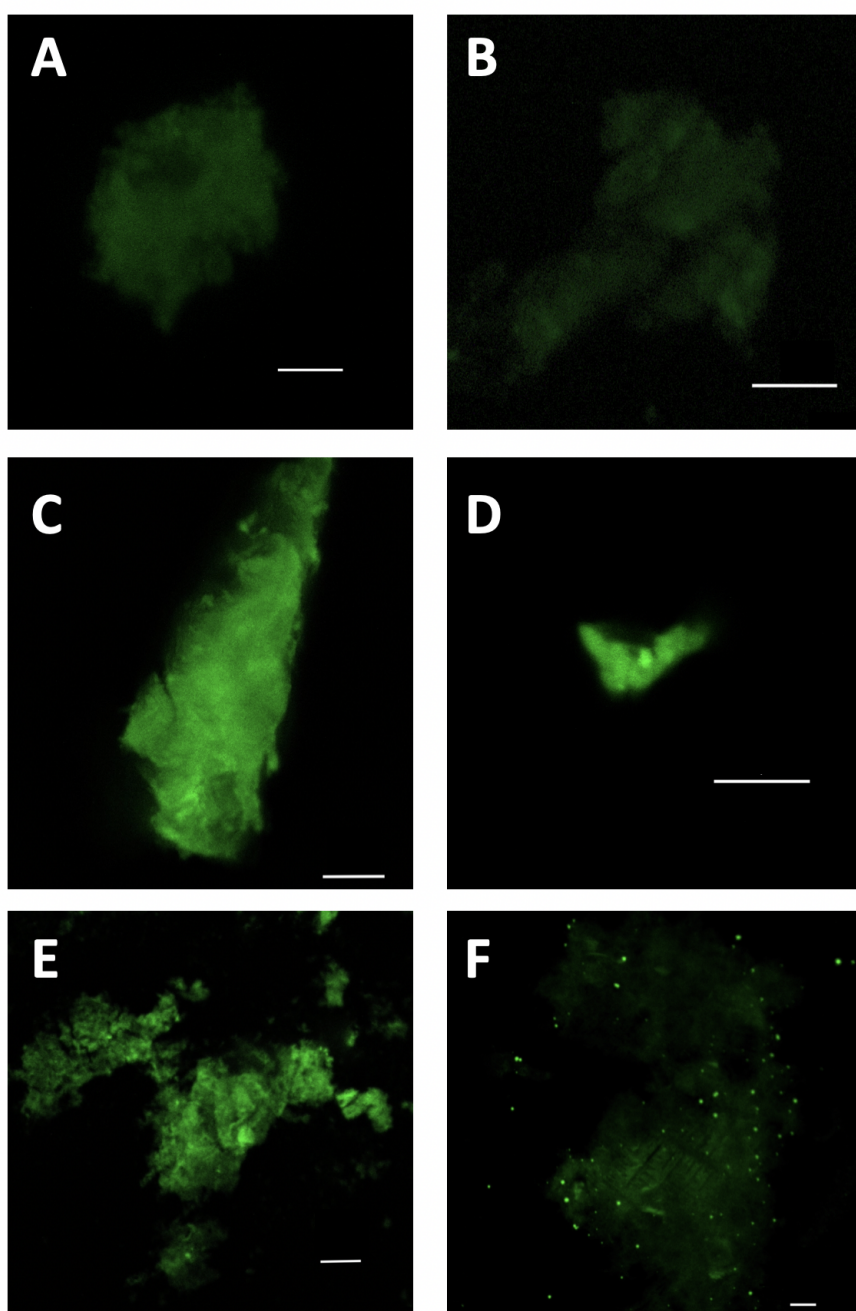


Figure 4.16: (A) X34 in PBS. (B) HS335 in PBS. (C) X34, ATTR in PBS. (D) HS335, ATTR in PBS. (E) X34, INS PBS. (F) HS335, INS in PBS. X34 shows a smaller difference in emission intensity between samples compared to HS335 which is very faint by itself and only stains some parts of the insulin fibrils intensely. Ligand concentrations and fibril concentrations are $7\ \mu\text{M}$ for all samples. Scale bar is $15\ \mu\text{m}$. ($\lambda_{\text{ex}} = 405\text{nm}$, $\lambda_{\text{em}} = 415 - 630\text{nm}$)

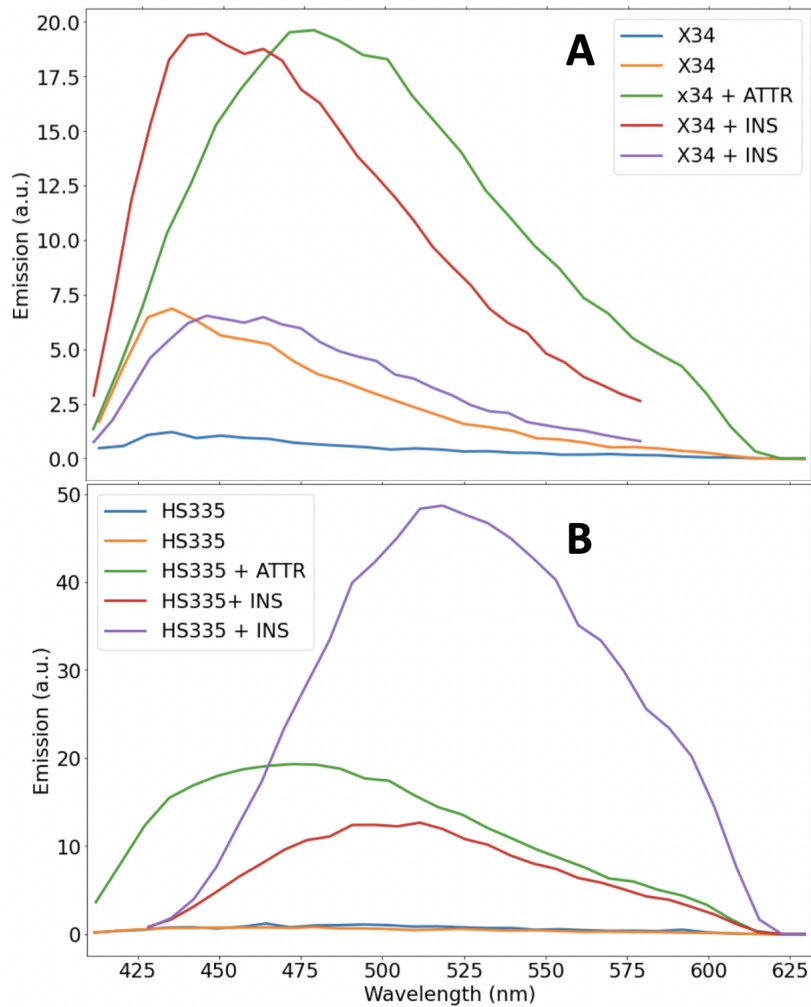


Figure 4.17: Emission of (A) X34 and (B) HS335 in PBS, alone and with ATTR and insulin fibrils. The intensity of emission is greatly increased with the addition of ATTR and insulin for both probes. HS335 is red-shifted when bound to insulin fibrils, while both insulin and ATTR seem to give X34 a slight red-shift. Concentrations are $7\ \mu\text{M}$ for both ligands and fibrils. ($\lambda_{\text{ex}} = 405\text{nm}$)

Insulin and ATTR Fibrils in HEK-293 Cells

After successfully staining both fibril types in PBS, introduction of $7\ \mu\text{M}$ insulin and $7\ \mu\text{M}$ ATTR fibrils to HEK-293 cells was attempted. The cells were incubated overnight using $7\ \mu\text{M}$ X34, as well as stained with 1X concentration of CellMask Deep Red (CM). The latter to stain the cell membrane of the cells for simpler determination of whether the fibrils had entered the cells. A single HEK-293 cell is shown in figure 4.18 using both CLSM and FLIM imaging. The color bars are associated with the FLIM image, with the full-color bar showing the lifetime in ns, see section 3.4.3 for details. The cell seems to contain an ATTR fibril, which

was stained efficiently by X34. By fitting the FLIM data to a double exponential function, see figure 4.20, the fluorescence lifetime was found to be $1430 \text{ ps} \pm 94$. This is a significant increase compared to the lifetime observed for X34 in PBS in section 4.1.3 ($260 \text{ ps} \pm 22$), and slightly shorter than that found for X34 bound to ATTR in PBS in section 4.1.4 ($1520 \text{ ps} \pm 15$).

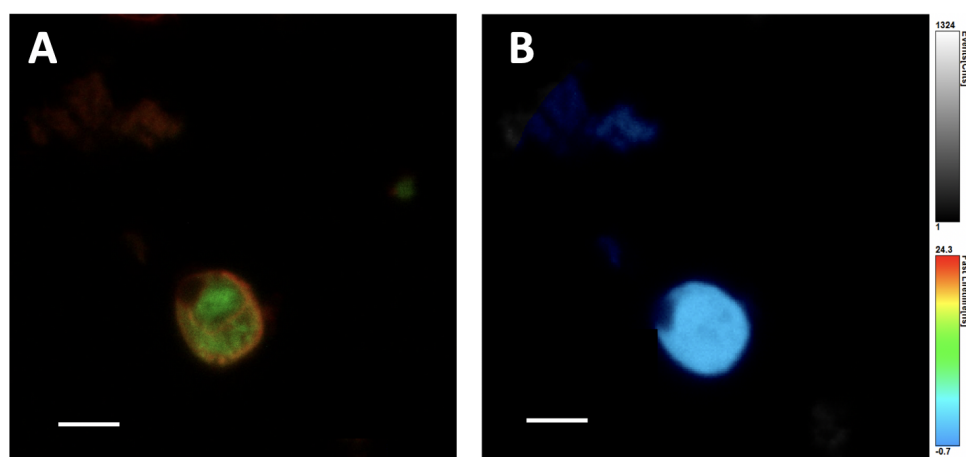


Figure 4.18: (A) CLSM and (B) FLIM imaging zoomed in on a single HEK-293 cell with $7 \mu\text{M}$ ATTR fibrils stained using $7 \mu\text{M}$ X34 (green) and 1X CellMask Deep Red (red). The fibrils seem to have entered the cell. Scale bar is $8 \mu\text{m}$. For details, see the text. ($\lambda_{\text{ex}} = 405\text{nm}$, $\lambda_{\text{em}} = 415 - 630\text{nm}$)

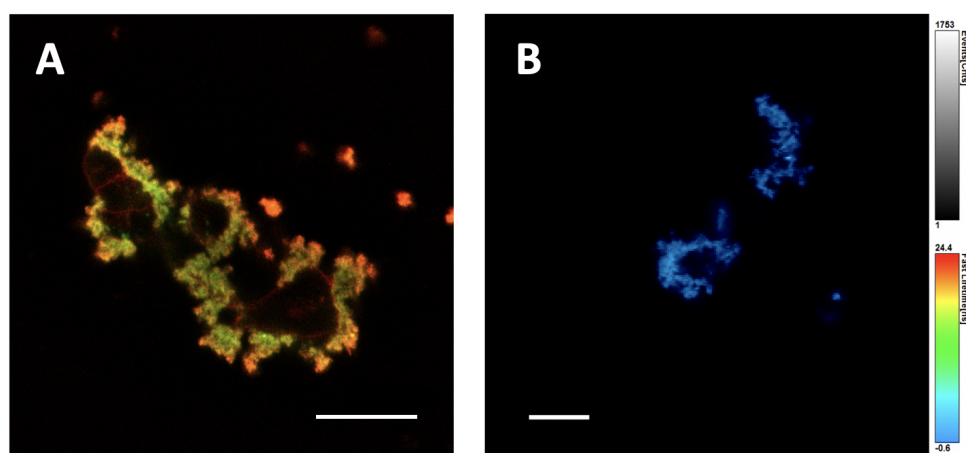


Figure 4.19: (A) CLSM and (B) FLIM imaging of HEK-293 cells with $7 \mu\text{M}$ insulin fibrils, stained using $7 \mu\text{M}$ X34 (green) and 1X CellMask Deep Red (red). The fibrils cluster on the outside of the cells. Scale bar is $30 \mu\text{m}$. For details, see the text. ($\lambda_{\text{ex}} = 405\text{nm}$, $\lambda_{\text{em}} = 415 - 630\text{nm}$)

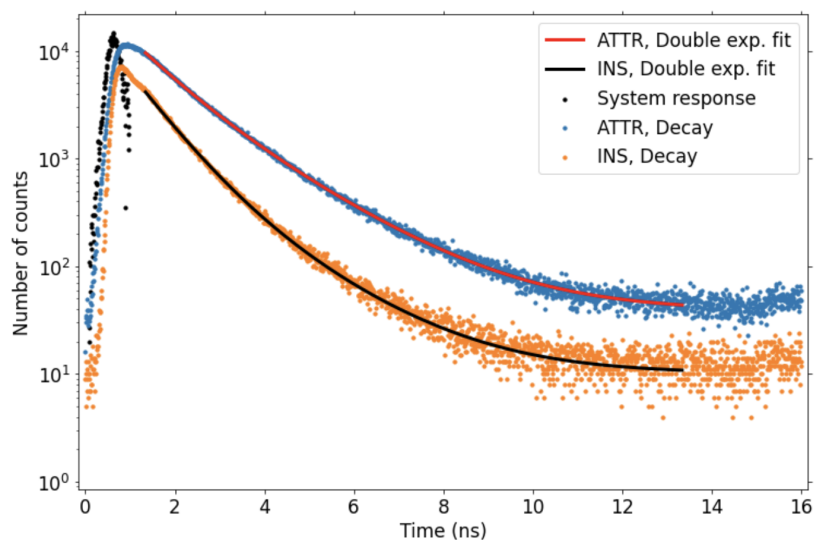


Figure 4.20: An example of the fitting of a double exponential function to the decay measured through FLIM imaging, here showing ATTR and insulin fibrils stained with X34. See text for details.

Figure 4.19 shows HEK-293 cells with $7\ \mu\text{M}$ insulin fibrils, stained with $7\ \mu\text{M}$ X34 and 1X CellMask Deep Red. In contrast to ATTR, the insulin fibrils appear to not enter the cells but instead cluster onto the outside of the cell membrane. This is consistent with the insulin fibrils having a fibrillar morphology, while ATTR has a smaller, more filamentous structure, allowing them to enter the cells more easily than insulin. The insulin fibrils have also been stained well with X34, and interestingly there seems also to be some co-staining with CellMask Deep Red. By fitting the FLIM data to a double exponential function, see figure 4.20, the fluorescence lifetime was found to be $1040\ \text{ps} \pm 50$. This is significantly longer than the lifetime of X34 in solvent found from the photophysics experiments in section 4.1.3 ($260\ \text{ps} \pm 22$), and slightly shorter than that found for X34 bound to insulin fibrils in PBS in section 4.1.4 ($1210\ \text{ps} \pm 3$).

The emission spectra of X34 in cells, alone and with ATTR and insulin fibrils, are shown in figure 4.21. The emission intensity increased when bound to ATTR, and greatly increased when bound to insulin. It is difficult to determine whether there is any shift in emission for either of the fibril types due to the large difference in emission maxima for the two spectra of X34 alone in HEK-293 cells ($\lambda_{\text{em,max}} = 452, 476$), however, the spectra of X34 bound to ATTR within the cells ($\lambda_{\text{em,max}} = 468, 468$) seem red-shifted compared to X34 bound to insulin only ($\lambda_{\text{em,max}} = 445$). It is noted that the resolution of the emission spectra is here $\sim 5.6\ \text{nm}$, much lower than for spectroscopic measurements.

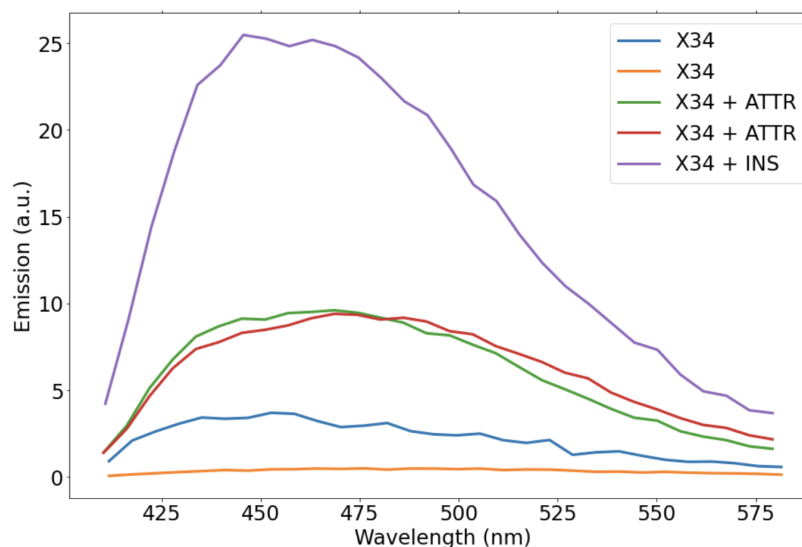


Figure 4.21: Emission spectra of 7 μM X34 in HEK-293 cells, alone and with 7 μM ATTR and insulin fibrils. There is a clear increase in intensity of emission for X34 bound to both fibril types, with a significantly higher intensity from X34 bound to insulin fibrils. There seems to be no clear shift in emission of X34 when bound to the fibrils compared to alone in HEK-293 cells. ($\lambda_{\text{ex}} = 405\text{nm}$)

4.2.2 Testing Various Incubation Times for ATTR Fibrils

After the initial preliminary experiments with the ATTR/HEK-293 system, it was attempted to find the optimal incubation time for transfection of fibrils into HEK-293 cells. The ATTR fibrils (7 μM) and X34 (7 μM) were added to the cells simultaneously and three incubation times were tested, 24 h, 48 h and 72 h. Moreover, 7 μM ATTR fibrils in PBS were also incubated with 7 μM X34 for 24 h, and 7 μM X34 was added to HEK-293 cells without any fibrils for 24 h, as a comparison to the stained fibrils in cells. All cells were also stained with 1X CellMask Deep Red (CM), in order to better determine whether the fibrils had entered the cells. CLSM images of cells after 24 h, 48 h and 72 h of incubation with ATTR and X34, as well as cells incubated with only X34 for 24 h hours, are displayed in figure 4.22.

The ATTR fibrils appear to have entered the cells after only 24 h (A), however the stain is much fainter and more diffuse than after 48 h (B) and 72 h (C). There appears to be fibrils in the cells after both 48 h and 72 h, and the stain has a more granular appearance and a higher intensity than after 24 h. The cells survived all the incubation times, however, they appeared slightly more shriveled and clustered together after 72 h (C), which could point to them reacting negatively to the long exposure to ATTR fibrils and X34. For ease of preparations and to ensure the health of the cells, incubation times are kept around 36 – 48h for subsequent experiments, to reach a higher intensity of staining than after 24 h. For the HEK-

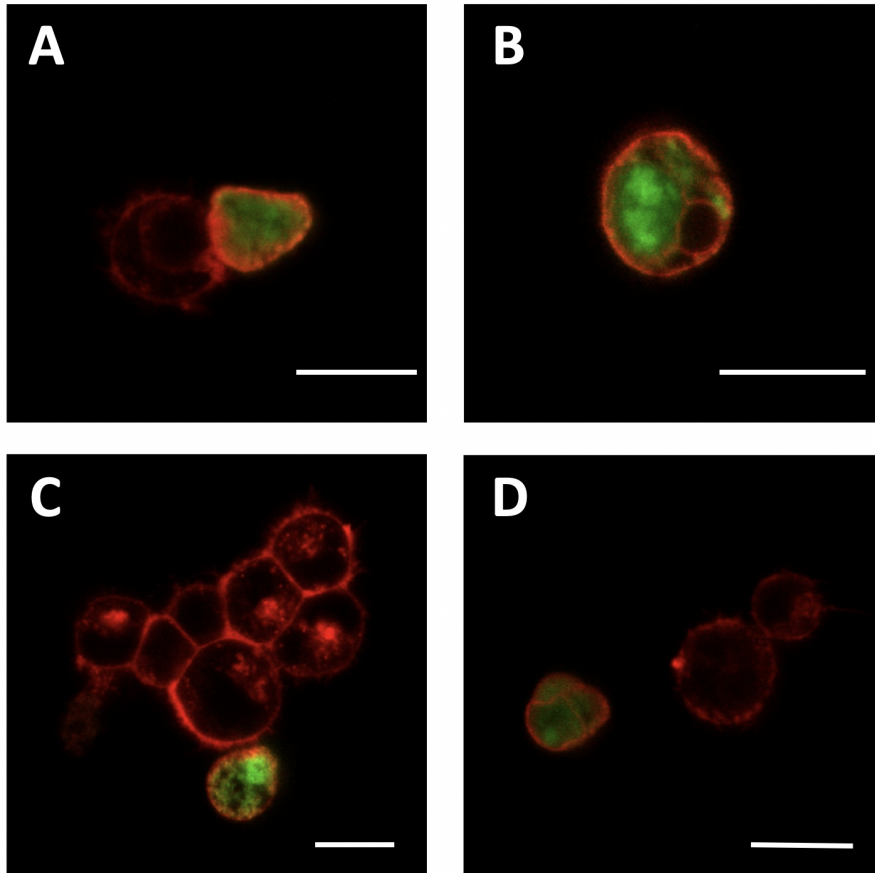


Figure 4.22: HEK-293 cell incubated with $7\mu\text{M}$ ATTR fibrils and $7\mu\text{M}$ X34 (green) for (A) 24 h, (B) 48 h and (C) 72 h, as well as (D) HEK-293 cells incubated with $7\mu\text{M}$ X34 for 24 h hours. All cells were also stained with 1X CellMask Deep Red (red). Scale bar is $15\mu\text{m}$. ($\lambda_{\text{ex}} = 405\text{nm}$, $\lambda_{\text{em}} = 415 - 630\text{nm}$)

293 cells without ATTR (D), X34 seems to enter the cell and stain the cytosol or some organelle in a way that could be mistaken for a fibril having entered the cell. However, the intensity is much lower and the stain has a more diffuse appearance than that of the fibrils inside the cells, making it possible to distinguish normal cells from those containing fibrils.

CLSM and FLIM images of $7\mu\text{M}$ ATTR fibrils in PBS incubated with $7\mu\text{M}$ X34 for 24 h are presented in figure 4.23. The structure of the fibrils is clearly discerned by X34. The lifetime of the fibrils was found fitting the FLIM data to a double exponential equation, giving $1470\text{ps} \pm 128$.

From the various CLSM images, X34 has a clear increase in intensity when bound to ATTR fibrils. In addition, when looking at the normalized emission spectra of X34 bound to ATTR as well as alone in cells, shown in figure 4.24, there is a clear

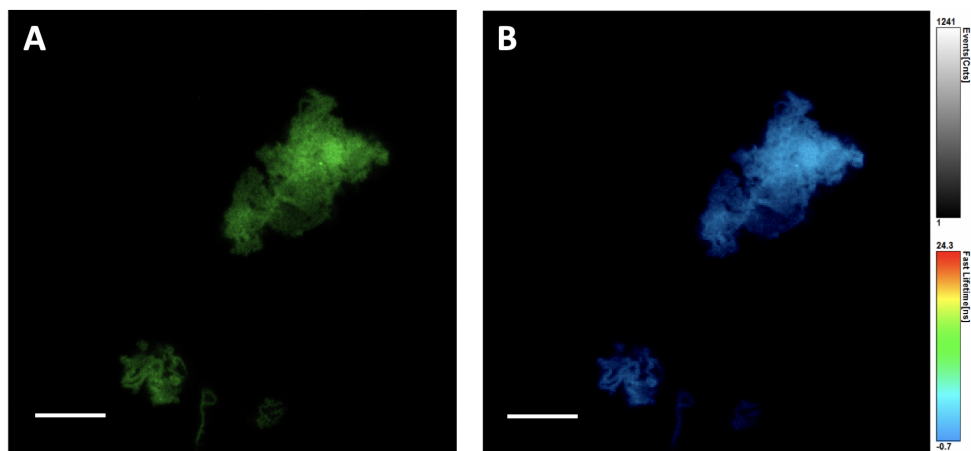


Figure 4.23: (A) CLSM and (B) FLIM imaging of 7 μM ATTR fibrils in PBS, stained with 7 μM X34 for 24 h. Scale bar is 30 μm . ($\lambda_{\text{ex}} = 405\text{nm}$, $\lambda_{\text{em}} = 415 - 630\text{nm}$)

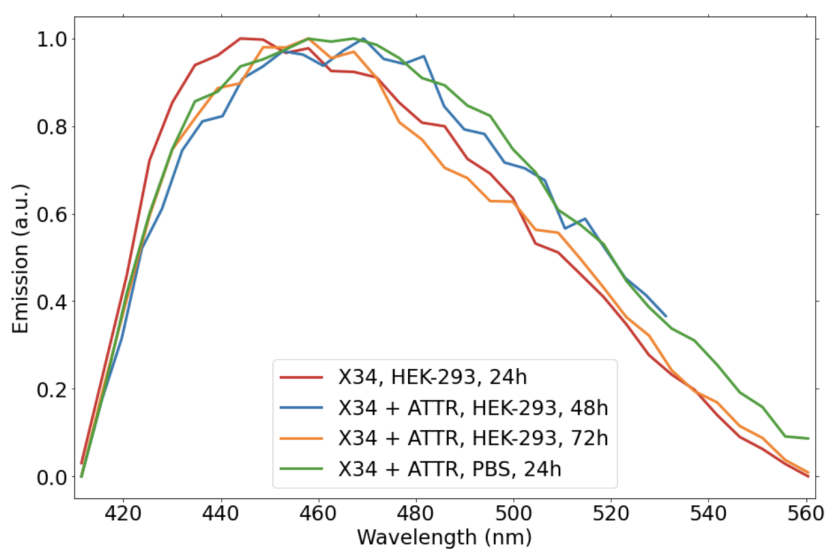


Figure 4.24: Emission spectra of 7 μM X34 in HEK-293 cells, alone and with 7 μM ATTR fibrils, as well as in PBS with 7 μM ATTR fibrils. All spectra were normalized to 1, and there is a clear red-shift in emission of X34 when bound to ATTR fibrils compared to in cells without fibrils. ($\lambda_{\text{ex}} = 405\text{nm}$)

red-shift when bound to the ATTR fibrils.

The fluorescence lifetimes found from using FLIM on the various samples are presented in table 4.9. The lifetimes are all very close in value, with the lifetimes of X34 bound to ATTR being somewhat longer than the lifetime of X34 only in HEK-293 cells.

Table 4.9: Fluorescence lifetimes of 7 μM X34 with 7 μM ATTR fibrils in PBS, as well as HEK-293 cells stained with 7 μM X34 with and without 7 μM ATTR. The lifetimes were found using FLIM and fitting the data to a double exponential equation.

Sample	Lifetime (ps)
X34 + ATTR	1470 ± 128
X34 in HEK-293	1460 ± 80
X34 + ATTR in HEK-293 (48 h)	1520 ± 56
X34 + ATTR in HEK-293 (72 h)	1470 ± 59

4.2.3 Comparing X34/ATTR in Two Cell Models

The ligand X34 in HEK-293 cells has already been studied in the comparison with insulin fibrils and in the ATTR incubation trial, where it was shown that there is a large increase in intensity of X34 with addition of ATTR fibrils, as well as a possible red-shift upon ATTR binding. No significant changes in the fluorescence lifetime was found, likely due to the close resemblance of the lifetime of X34 in HEK-293 cells and X34 bound to fibrils in PBS. In these experiments, a concentration of 7 μM was used for X34, however, ATTR fibrils can also be detected at substantially lower X34 levels. Some additional details from studies of X34 in both HEK-293 and SH-SY5Y cells will be presented here.

ATTR fibrils (7 μM) and X34 (1 μM) were added to HEK-293 and SH-SY5Y cells with 48 h incubation time. The cells were also stained with 2.5 μM DRAQ5. The difference between both cell lines with and without ATTR fibrils are shown in figure 4.25. Both HEK-293 samples (**A** and **B**) show the appearance of diffusely stained cytosol with evenly distributed, brighter spots, but the cells with ATTR fibrils (**B**) appear connected by a mesh-like structure as well, likely the fibrils. It is difficult to visually determine whether the fibrils have entered the cells or are just stuck to the outside of the cell membrane. The cytosol of the SH-SY5Y cells (**C** and **D**) have not been stained by X34, and the cells also lack the evenly distributed, brightly stained spots visible in the HEK-293 cells. However, some smaller artifacts in some of the cells were stained intensely. For SH-SY5Y cells with ATTR fibrils (**D**), a mesh-like structure can be found between the cells as with the HEK-293 cells, however it is much smaller in size. The fibril appears to have entered at least one of the cells (red arrow).

Lower concentrations of ATTR fibrils with 1 μM X34 were also attempted, but none were stained well. The emission of X34 was very faint and the images had to be greatly enhanced to be able to see the stain. Higher concentrations of X34 are likely needed to visualize lower ATTR concentrations, but at the expense of higher background from non-bound X34.

The emission of 7 μM X34 with 7 μM ATTR in HEK-293 cells was detailed in sections 4.2.1 and 4.2.2, showing a large increase in emission intensity upon

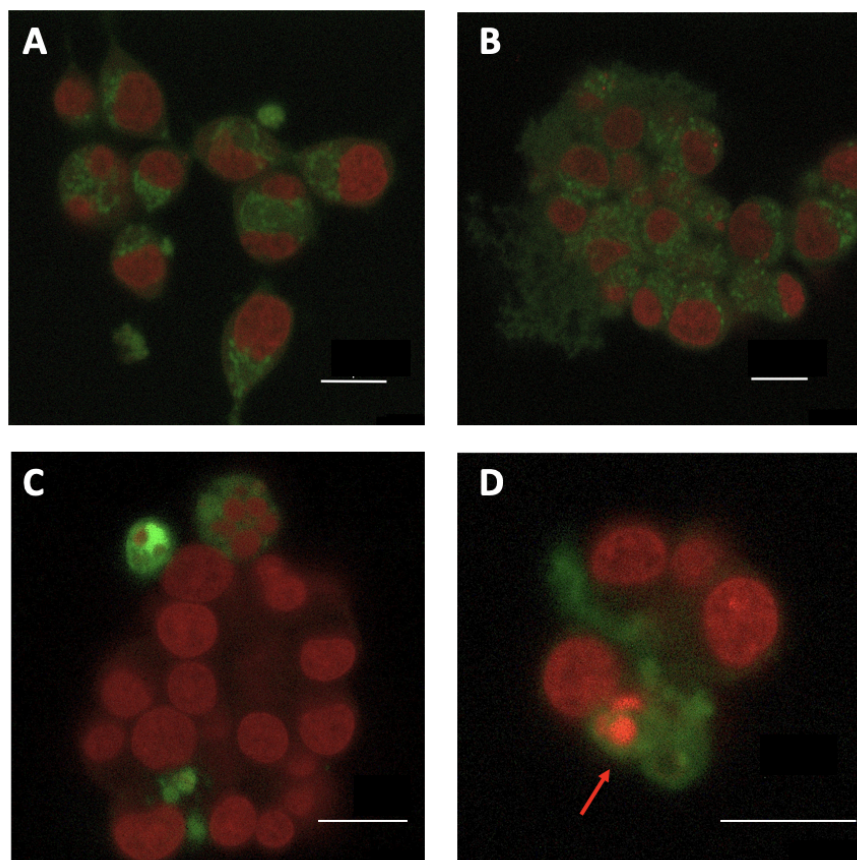


Figure 4.25: (A) HEK-293 cells stained with $1\ \mu\text{M}$ X34 (green) and $2.5\ \mu\text{M}$ DRAQ5 (red). (B) HEK-293 cells with $7\ \mu\text{M}$ ATTR fibrils, stained with $1\ \mu\text{M}$ X34 (green) and $2.5\ \mu\text{M}$ DRAQ5 (red). (C) SH-SY5Y cells stained with $1\ \mu\text{M}$ X34 (green) and $2.5\ \mu\text{M}$ DRAQ5 (red). (D) SH-SY5Y cells with $7\ \mu\text{M}$ ATTR fibrils, stained with $1\ \mu\text{M}$ X34 (green) and $2.5\ \mu\text{M}$ DRAQ5 (red). All images have had their contrast enhanced by the same amount to better show the stains. Scale bar is $16\ \mu\text{m}$. ($\lambda_{\text{ex}} = 405\text{nm}$, $\lambda_{\text{em}} = 415 - 630\text{nm}$)

ATTR binding, as well as a possible red-shift compared to X34 alone in HEK-293 cells. The emission of $7\ \mu\text{M}$ X34 in SH-SY5Y cells with and without $7\ \mu\text{M}$ ATTR is shown in figure 4.26. There is a large increase in intensity between the average intensity from X34 in SH-SY5Y cells without ATTR, and the intensity of an ROI of an ambiguous artifact in the cells with ATTR. However, for emission intensities measured from the ROI of a whole cell or a diffuse area, the intensity is similar to, or even lower than, the emission intensity of X34 in SH-SY5Y cells without ATTR. Intensity of emission of X34 is thus likely to be an unreliable identifier for whether the ATTR fibrils have entered the SH-SY5Y cells or not. See appendix D for further information on deciding on the ROIs for emission and lifetime measurements.

The lifetime of X34 in HEK-293 cells with and without ATTR fibrils was already

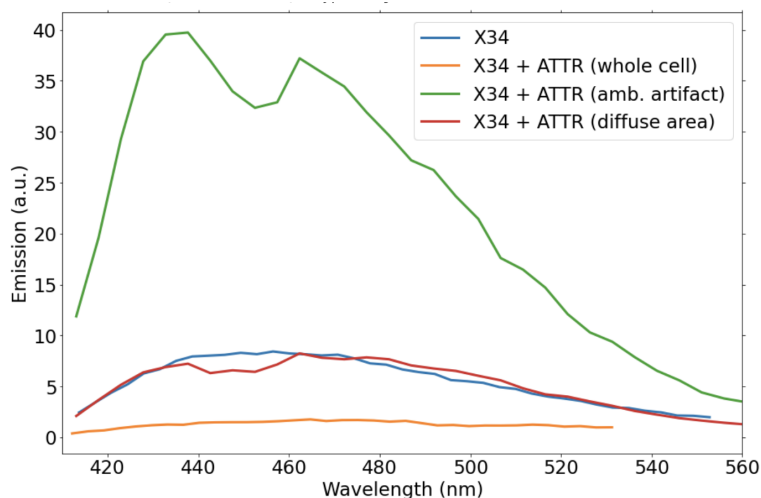


Figure 4.26: Emission of $7 \mu\text{M}$ X34 in SH-SY5Y cells, with and without $7 \mu\text{M}$ ATTR fibrils. There are large differences in the intensity of emission from SH-SY5Y cells with ATTR depending on what ROI is chosen. ($\lambda_{\text{ex}} = 405\text{nm}$)

detailed in section 4.2.2. The lifetimes were very close in value and it was not possible to discern whether a HEK-293 cell contained ATTR or not solely based on the measured lifetimes. The lifetimes of X34 in SH-SY5Y cells with and without ATTR are presented in table 4.10, and FLIM images are shown in figure 4.27. The lifetime of X34 in SH-SY5Y cells without ATTR fibrils is close in value to X34 with ATTR in PBS, as well as to X34 in HEK-293 cells without ATTR ($1460\text{ps} \pm 80$). However, with addition of ATTR to the SH-SY5Y cells, the lifetime of X34 becomes much shorter. One of the three measured lifetimes is almost identical to that of SH-SY5Y cells without fibrils, and is thus likely also a cell without a fibril. The other two are much shorter, indicating that the interaction between ATTR and SH-SY5Y shortens the lifetime of X34 compared to when bound to just one of the two. This suggests that the measured fluorescence lifetime of X34 in a SH-SY5Y cell could be a useful tool for determining the presence of ATTR within the SH-SY5Y cell.

Table 4.10: Fluorescence lifetimes and average lifetimes of $7 \mu\text{M}$ X34 with $7 \mu\text{M}$ ATTR fibrils in PBS, as well as SH-SY5Y cells stained with $1 \mu\text{M}$ and $7 \mu\text{M}$ X34 with and without $7 \mu\text{M}$ ATTR, respectively. The lifetimes were found using FLIM and fitting the data to a double exponential equation. Different concentrations can be compared, as fluorescence lifetime is not affected by fluorophore concentration.

Sample	Lifetime (ps)	Avg. Lifetime (ps)
$7 \mu\text{M}$ X34 + ATTR in PBS	1470 ± 128	1470 ± 128
$1 \mu\text{M}$ X34 in SH-SY5Y	1550 ± 55	1550 ± 55
$7 \mu\text{M}$ X34 + ATTR in SH-SY5Y	690 ± 16	1080 ± 32
$7 \mu\text{M}$ X34 + ATTR in SH-SY5Y	1000 ± 15	
$7 \mu\text{M}$ X34 + ATTR in SH-SY5Y	1550 ± 65	

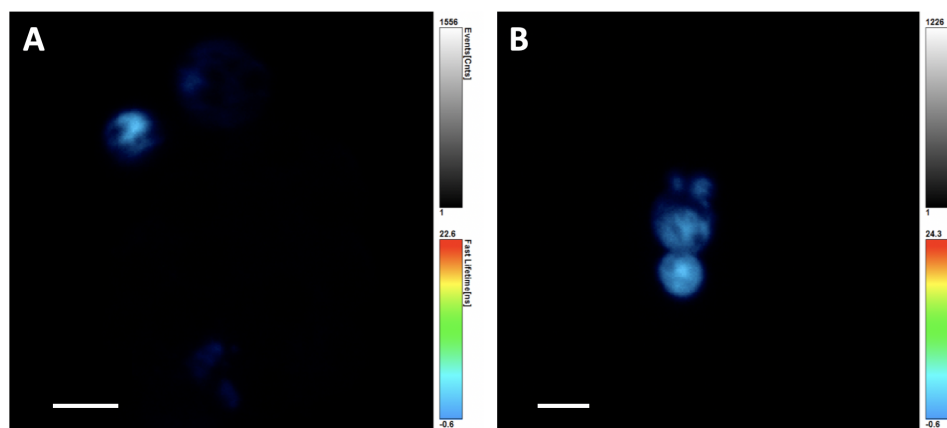


Figure 4.27: FLIM imaging of (A) SH-SY5Y cells stained with 1 μM X34 and 2.5 μM DRAQ5, and (B) SH-SY5Y cells with 7 μM ATTR fibrils, stained with 7 μM X34 and 2.5 μM DRAQ5. Scale bar is 10 μm . Different concentrations can be compared as fluorescence lifetime is not affected by fluorophore concentration. ($\lambda_{\text{ex}} = 405\text{nm}$, $\lambda_{\text{em}} = 415 - 630\text{nm}$)

4.2.4 Comparing HS335/ATTR in Two Cell Models

Various concentrations of ATTR fibrils (4.7 μM , 3.1 μM , 2.0 μM and 0 μM) and 1 μM HS335 were added to HEK-293 cells with 48 h incubation time. The cells were also stained with 2.5 μM DRAQ5. The difference between HEK-293 cells with these concentrations of ATTR are shown in figure 4.28. The cytosol of the HEK-293 cells were stained regardless of the presence of ATTR fibrils, but the intensity is higher for the cells with added 4.7 μM ATTR (B), indicating that ATTR have entered the cells. A few intensely stained spots are also visible in one of the HEK-293 cells with ATTR (red arrow), and further investigations are needed to determine the source. The clear increase in intensity of emission with addition of 4.7 μM ATTR proves that HS335 can discern lower concentrations of ATTR than 7 μM , even at concentrations as low as 1 μM for the ligand. The lower concentrations of ATTR (3.1 μM (C) and 2.0 μM (D)) were also visibly stained by HS335, however, the emission intensity decreases with lower concentrations, and it becomes more difficult to discern whether the ATTR fibrils have entered the cells.

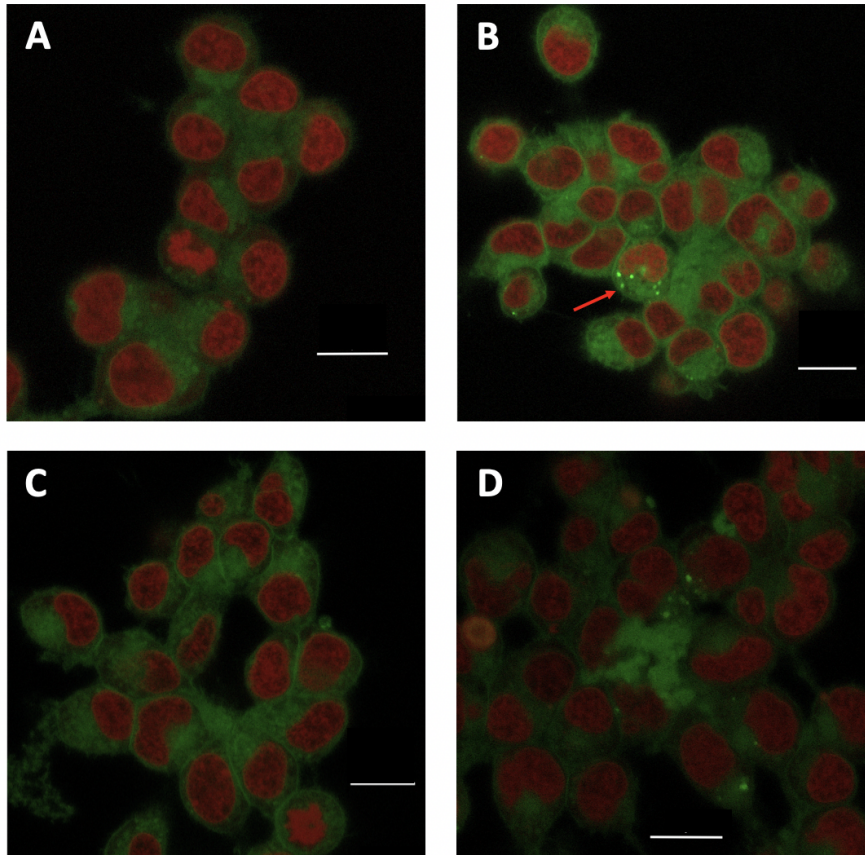


Figure 4.28: CLSM imaging of HEK-293 cells incubated with ATTR/HS335 at different ratios. The concentration of HS335 was held constant ($1\ \mu\text{M}$) and ATTR concentration was varied (A) no ATTR, (B) $4.7\ \mu\text{M}$, (C) $3.1\ \mu\text{M}$, and (D) $2.0\ \mu\text{M}$. All samples were also stained with $2.5\ \mu\text{M}$ DRAQ5 (red). Images have had their contrast enhanced by the same amount to better show the stains. Emission intensity decreases for lower concentrations of ATTR. Scale bar is $16\ \mu\text{m}$. ($\lambda_{\text{ex}} = 405\text{nm}$, $\lambda_{\text{em}} = 415 - 630\text{nm}$)

ATTR fibrils ($7\ \mu\text{M}$) and HS335 ($1\ \mu\text{M}$) were added to SH-SY5Y cells with 48 h incubation time. The cells were also stained with $2.5\ \mu\text{M}$ DRAQ5. The difference between SH-SY5Y cells with and without ATTR fibrils are shown in figure 4.29. Like with the HEK-293 cells, the cytosol of the SH-SY5Y cells was stained by HS335 regardless of the presence of ATTR fibrils, but the intensity is higher for cells with added ATTR (B), indicating that the fibrils have entered the cells. HS335 also seems to have an affinity for some brightly stained spots in the SH-SY5Y cells (red arrows). These spots are stained in the cells with and without ATTR, and are possibly some specific SH-SY5Y morphology. Further studies should be performed to determine the source, as they could be mistaken for ATTR fibrils due to their high intensity.

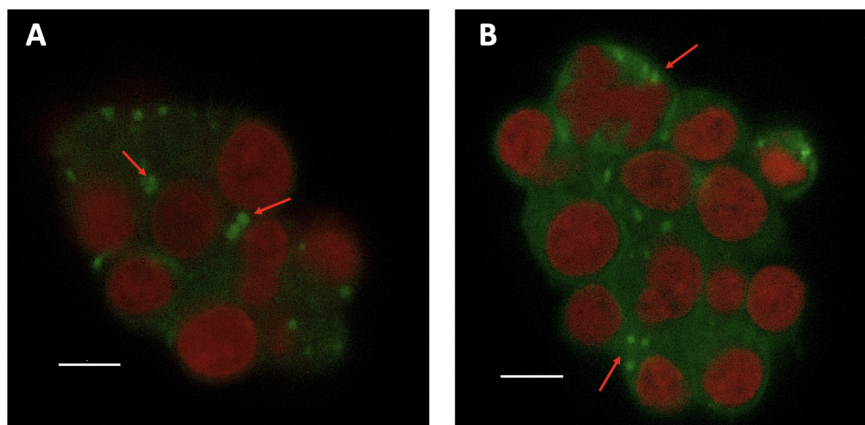


Figure 4.29: CLSM imaging of SH-SY5Y cells stained with $1\ \mu\text{M}$ HS335 (green), (A) without ATTR and (B) with $7\ \mu\text{M}$ ATTR. Both samples were also stained with $2.5\ \mu\text{M}$ DRAQ5 (red). Images have had their contrast enhanced by the same amount to better show the stains. Scale bar is $8\ \mu\text{m}$. ($\lambda_{\text{ex}} = 405\text{nm}$, $\lambda_{\text{em}} = 415 - 630\text{nm}$)

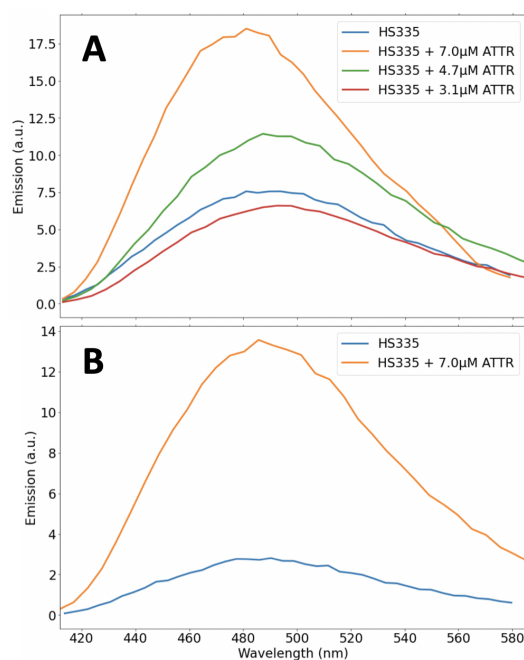


Figure 4.30: Average emission of $1\ \mu\text{M}$ HS335 in (A) HEK-293 cells and (B) SH-SY5Y cells, with various concentrations of ATTR fibrils. There is a large difference in intensity between cells with and without $7\ \mu\text{M}$ ATTR fibrils in both cell lines. This difference decreases with ATTR concentration for HEK-293 cells. ($\lambda_{\text{ex}} = 405\text{nm}$)

The average emission spectra of HS335 in HEK-293 and SH-SY5Y cells with various concentrations of ATTR are shown in figure 4.30. There is a significant difference in intensity between cells with and without $7\ \mu\text{M}$ ATTR fibrils in both cell lines. The emission of HS335 with lower concentrations were also measured in HEK-293 cells, and the intensity decreases with lower concentrations. For $3.1\ \mu\text{M}$ ATTR, the intensity is lower than cells without ATTR fibrils. The intensity of emission of HS335 can thus only be used to detect the presence of ATTR at higher concentrations.

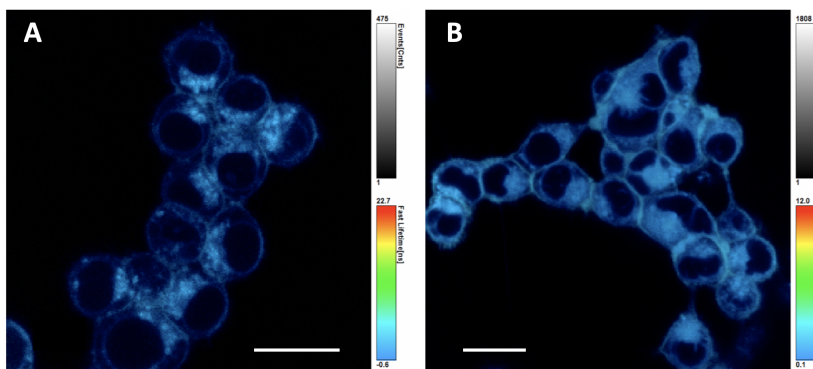


Figure 4.31: FLIM imaging of (A) HEK-293 cells stained with $1\ \mu\text{M}$ HS335 and $2.5\ \mu\text{M}$ DRAQ5, and (B) HEK-293 cells with $3.1\ \mu\text{M}$ ATTR fibrils, stained with $1\ \mu\text{M}$ HS335 and $2.5\ \mu\text{M}$ DRAQ5. Scale bar is $20\ \mu\text{m}$. ($\lambda_{\text{ex}} = 405\text{nm}$, $\lambda_{\text{em}} = 415 - 630\text{nm}$)

Table 4.11: Average fluorescence lifetimes of $1\ \mu\text{M}$ HS335 in HEK-293 cells with various concentrations of ATTR fibrils. Concentrations of ATTR fibrils were between $2 - 7\ \mu\text{M}$, and no obvious relation between concentration of ATTR and length of lifetime was found. The lifetimes were found using FLIM and fitting the data to a double exponential equation.

Sample	τ (ps) (ATTR conc.)	$\bar{\tau}$ (ps)
HS335, HEK-293	1260 ± 3	1370 ± 8
	1290 ± 9	
	1560 ± 11	
HS335 + ATTR, HEK-293	966 ± 11.5 ($2\ \mu\text{M}$)	1150 ± 24
	1130 ± 8 ($2\ \mu\text{M}$)	
	1000 ± 80 ($3.1\ \mu\text{M}$)	
	1230 ± 17 ($3.1\ \mu\text{M}$)	
	1180 ± 15 ($4.7\ \mu\text{M}$)	
	1400 ± 11 ($7\ \mu\text{M}$)	

The fluorescence lifetimes of HS335 in HEK-293 cells with and without ATTR fibrils are summarized in table 4.11, and FLIM images of HEK-293 cells with and without ATTR are shown in figure 4.31. The average lifetime decreases with the

addition of ATTR and could possibly be used to detect the presence of fibrils in cells. However, the difference is not that significant, and there are large variations in the individual lifetimes measured from HEK-293 cells with ATTR, and thus more measurements should be performed to confirm the values.

The fluorescence lifetimes of HS335 in SH-SY5Y cells with and without ATTR fibrils are tabulated in table 4.12. A visual example of the difference between diffuse and bright areas is shown in figure 4.32, and further information on ROI selection can be found in appendix D. The diffuse areas are likely ATTR fibrils located outside the cells, while the bright areas are assumed to be fibrils that have entered the SH-SY5Y cells. The average fluorescence lifetime of HS335 increases with the addition of ATTR, and increases further for ATTR fibrils that have entered the cells. This suggests that the measured lifetime of HS335 in SH-SY5Y cells could be used to accurately determine the presence of ATTR fibrils.

Table 4.12: Average fluorescence lifetimes of 5 μM HS335 in SH-SY5Y cells with and without 7 μM ATTR fibrils. The lifetimes were found using FLIM and fitting the data to a double exponential equation.

Sample	τ (ps)	$\bar{\tau}$ (ps)
HS335, SH-SY5Y	840 ± 4	860 ± 7
	870 ± 9	
HS335 + ATTR, SH-SY5Y (diffuse area)	990 ± 6	990 ± 6
	1000 ± 5	
HS335 + ATTR, SH-SY5Y (bright area)	1110 ± 16	1260 ± 10
	1420 ± 3	

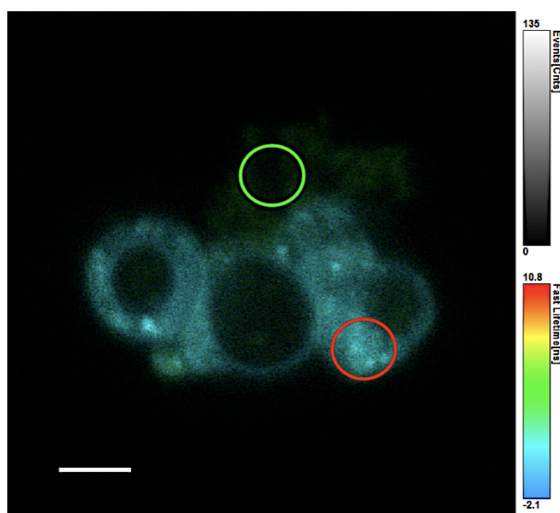


Figure 4.32: Examples of what is meant by diffuse (green) and bright (red) areas when choosing the ROI for lifetime calculations of HS335 after FLIM measurements. Scale bar is 6 μm . ($\lambda_{\text{ex}} = 405\text{nm}$, $\lambda_{\text{em}} = 415 - 630\text{nm}$)

4.2.5 Comparing HS336/ATTR in Two Cell Models

The ligand HS336 (7 μM) was added to SH-SY5Y cells together with ATTR fibrils (7 μM) with an incubation time of 36 h. DRAQ5 (5 μM) was also added to better visualize the cells. CLSM images of the SH-SY5Y cells stained with HS336, with and without ATTR fibrils, are shown in figure 4.33. HS336 seems to have a high affinity for some specific spots in the SH-SY5Y cells (red arrows), both with and without ATTR fibrils, but there is a clear increase in intensity of emission with the addition of ATTR (B).

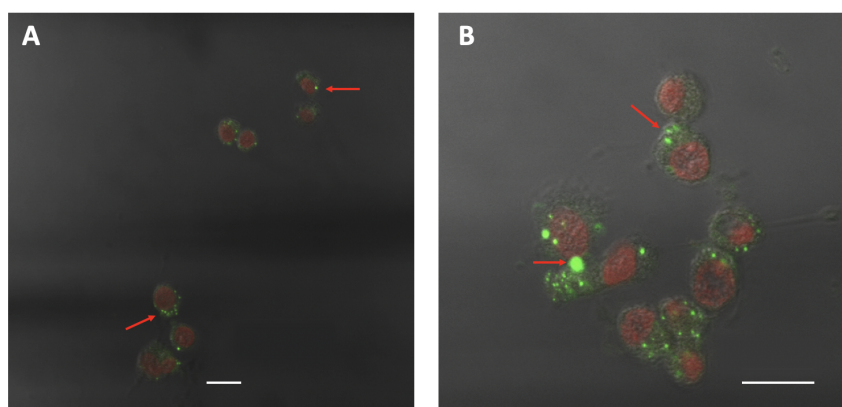


Figure 4.33: CLSM imaging of (A) SH-SY5Y cells stained with 7 μM HS336 (green) and 5 μM DRAQ5 (red), and (B) SH-SY5Y cells with 7 μM ATTR fibrils stained with 7 μM HS336 (green) and 5 μM DRAQ5 (red). An image of the transmitted light was layered over the CLSM images to show the shape of the cells. Scale bar is 16 μm . ($\lambda_{\text{ex}} = 470\text{nm}$, $\lambda_{\text{em}} = 480 - 640\text{nm}$)

Lower concentrations of HS336 were also attempted, with 1 μM and 2 μM of HS336 added to HEK-293 cells with and without 7 μM ATTR fibrils, with an incubation time of 48 h, see figure 4.34. The cells were seeded a full day before adding HS336 and ATTR, allowing them to settle and adhere completely before being exposed to the potential toxicity of ligand and protein. The cells were also stained with 2.5 μM DRAQ5. There is a significant difference in intensity between the two, but the cells are clearly visualized at both concentrations. There are also some intensely stained spots for 2 μM HS336 (red arrow) that will need further investigation. The cells appeared healthier at these concentrations of HS336 than they did in preliminary experiments with higher concentrations. Some cell nuclei were stained very well, while the majority appeared very faint, indicating that higher concentrations of DRAQ5 are needed to stain the cells well. Some cells were also stained with LT, but the stain was faint and photobleached too quickly to be imaged successfully. It was thus rejected for further use in this thesis.

The average emission spectra of HS336 in HEK-293 and SH-SY5Y cells with and without ATTR are presented in figure 4.35. There is a large increase in intensity with ATTR for ROIs inside the cell for both cell lines, while the intensity measured

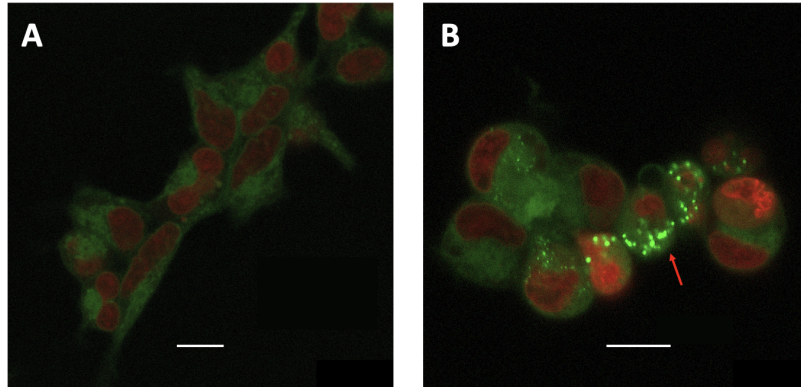


Figure 4.34: CLSM imaging of HEK-293 cells with 7 μM ATTR fibrils, stained with (A) 1 μM and (B) 2 μM HS336. (green) Both samples were also stained with 2.5 μM DRAQ5 (red). Images have had their contrast enhanced by the same amount to better show the stain. Scale bar is 16 μm . ($\lambda_{\text{ex}} = 470\text{nm}$, $\lambda_{\text{em}} = 480 - 640\text{nm}$)

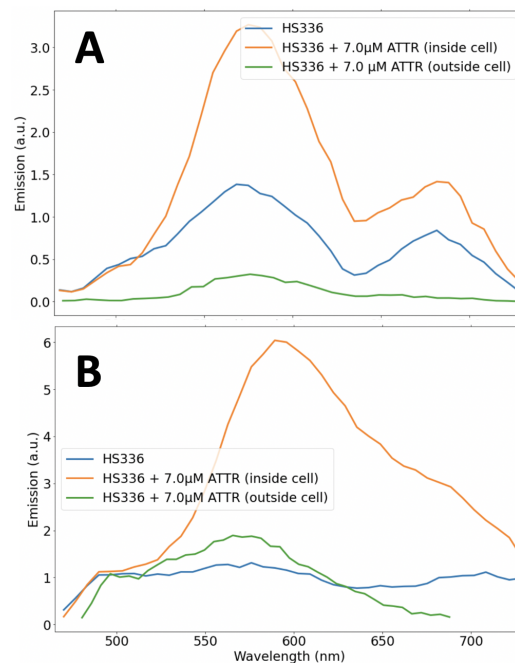


Figure 4.35: Average emission of 7 μM HS336 in (A) HEK-293 cells and (B) SH-SY5Y cells, with and without 7 μM ATTR. There is a large increase in intensity from inside the cells when ATTR is added. ($\lambda_{\text{ex}} = 470\text{nm}$)

for ROIs outside the cell is either lower or equal to the intensity of X34 in cells without fibrils for HEK-293 and SH-SY5Y cells, respectively. The large increase shown for ROIs inside the cells for both cell lines strongly suggests that the fibrils have entered the cells, and that the emission intensity is usable as a measure for

determining this.

FLIM images of HEK-293 cells stained with 7 μM HS336, both with and without 7 μM ATTR fibrils, are shown in figure 4.36, and the average lifetimes are summarized in table 4.13. There is a significant increase in the average lifetime between HS336 alone and with ATTR. Additionally, one of the values measured for HEK-293 cells with ATTR is much lower and closer in value to the lifetime of HS336 in HEK-293 cells without ATTR, possibly suggesting that this lifetime belongs to a cell that the ATTR fibrils have not entered. More measurements will be needed to confirm this, particularly for HEK-293 cells with only HS336, to see the variation of this value between different cells.

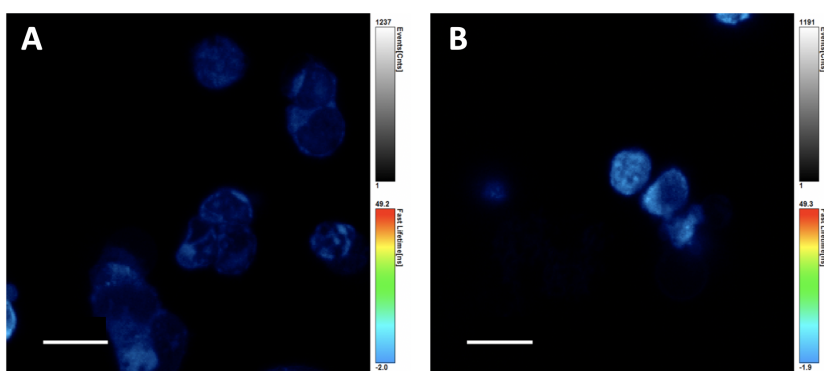


Figure 4.36: FLIM imaging of (A) HEK-293 cells stained with 7 μM HS336 and (B) HEK-293 cells with 7 μM ATTR fibrils stained with 7 μM HS336. Scale bar is 20 μm . ($\lambda_{\text{ex}} = 405\text{nm}$, $\lambda_{\text{em}} = 480 - 640\text{nm}$)

Table 4.13: Average fluorescence lifetimes of 5 μM and 7 μM HS336 in HEK-293 cells with and without 7 μM ATTR fibrils. There is a significant increase in the average lifetime of HS336 between HEK-293 cells with and without ATTR. Different concentrations can be compared due to the independence of the fluorescence lifetime of fluorophore concentration.

Sample	τ (ps) (HS336 conc.)	Avg. Lifetime (ps)
HS336, HEK-293	740 ± 100 (7 μM)	740 ± 100
	680 ± 17 (5 μM)	900 ± 89
HS336 + ATTR, HEK-293	1010 ± 133 (7 μM)	
	1020 ± 116 (7 μM)	

The average fluorescence lifetimes of 5 μM and 7 μM HS336 in SH-SY5Y cells with and without 7 μM ATTR are tabulated in table 4.14, and a FLIM image showing the visual difference between the two types of ROIs in cells with ATTR is shown in figure 4.37. There is a small increase in the average lifetime of HS336 with added ATTR, regardless of the ROI chosen. With only one measured value for HS336 in SH-SY5Y cells without ATTR, and the difference in the average lifetime being smaller than 100 ps, it cannot be regarded as significant and more

measurements are needed to confirm whether the lifetime change upon adding fibrils is consistent. However, when looking more closely at the individual values, they seem to be split between lifetimes that are significantly higher than the lifetime of HS336 in SH-SY5Y cells without ATTR fibrils, and some that are very similar in value to the cell without fibrils. This could potentially indicate that the difference in lifetime is larger for SH-SY5Y cells where the ATTR have entered, and that the shorter lifetimes belong to cells without ATTR. If correct, this would make the fluorescence lifetime of HS336 a useful tool for detection of ATTR in cells, however, more measurements are needed to confirm this.

Table 4.14: Average fluorescence lifetimes of 5 μM and 7 μM HS336 in SH-SY5Y cells with and without 7 μM ATTR fibrils. Fluorescence lifetime is independent of fluorophore concentration, so different concentrations of HS336 can be compared without issue.

Sample	τ (ps) (HS336 conc.)	$\bar{\tau}$ (ps)
HS336, SH-SY5Y	720 ± 31 (7 μM)	720 ± 31
HS336 + ATTR, SH-SY5Y (cell)	900 ± 5 (5 μM)	810 ± 41
	720 ± 77 (7 μM)	
HS336 + ATTR, SH-SY5Y (fib. structure)	920 ± 11 (5 μM)	810 ± 32
	750 ± 12 (7 μM)	
	760 ± 86 (7 μM)	
	820 ± 18 (7 μM)	

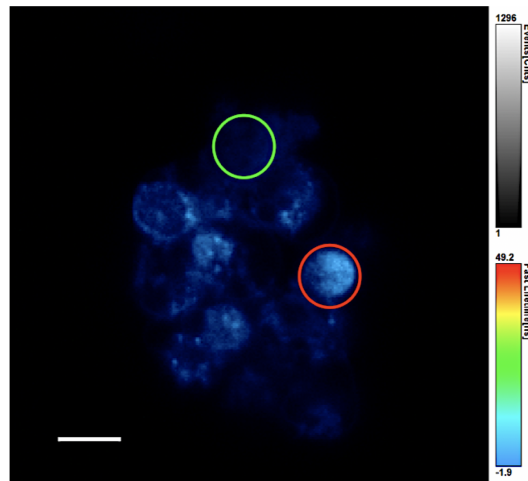


Figure 4.37: Example of the visual difference between a whole cell (red) and a fibrillar structure (green) for 7 μM HS336 with 7 μM ATTR in SH-SY5Y cells when choosing the ROI for lifetime calculations after FLIM measurements. Scale bar is 10 μm . ($\lambda_{\text{ex}} = 405\text{nm}$, $\lambda_{\text{em}} = 480 - 640\text{nm}$)

Chapter 5

Discussion

5.1 Photophysics

Firstly, a spectral screening of promising amyloid probes was performed, and the three ligands X34, HS335 and HS336 chosen for further studies. Photophysical data was collected from each of the ligands, with X34 also used in a Fluorescence Resonance Energy Transfer (FRET) comparison of native Wild-Type Transthyretin (WT-TTR) tetramers and Amyloid Transthyretin (ATTR) fibrils. In this section, all these results are discussed and compared. The photophysical results will also aid in distinguishing "free" probe in buffer from probe bound to ATTR in the cell model experiments, see section 5.2.

5.1.1 Microplate Reader Measurements

Screening of Potential Amyloid Ligands

The probes X34, HS335 and HS336 gave the most promising spectra in the screening of potential amyloid ligands. All three probes gave a high intensity (>10000 counts), and showed large differences in intensity when bound to ATTR compared to in solution, with HS336 having the largest difference in intensity. The ligand X34 could potentially also be used at pH 2.0 as there was a significant difference in intensity here as well, while HS336 displayed a significantly lowered intensity at pH 2.0 and HS335 appeared completely quenched. Both HS335 and HS336 are thus likely not usable at low pHs.

A decrease in intensity for both ligand in solution and ligand bound to ATTR after 24 h was observed for all three ligands. ATTR is more stable at pH 2.0 than at pH 7.4 due to the denaturing conditions of low pH interfering with refolding, and thus there is a chance that the fibrils could refold into native TTR tetramers after 24 h at physiological pH. However, as both spectra decrease in intensity, the change is less likely to be caused by some change in the ATTR fibrils or their binding to the

ligands over time, and more likely to be caused by photobleaching, induced by measuring with five different excitation wavelengths on day 1, as well as normal light exposure during handling of the samples before and after measurement. The change in intensity of X34 at pH 2.0 after 24 h is more interesting as the intensity of X34 bound to ATTR is slightly increased compared to the first measurement, while the intensity of X34 in solution has decreased a comparable amount to the decrease at pH 7.4. This could point to the binding to ATTR fibrils at pH 2.0 being a more prolonged process than at pH 7.4, and that X34 is not yet accommodated into the fibrils on day 1.

There are also clear shifts or changes in the emission spectra of both X34 and HS335 upon binding to fibrils. The emission of X34 appears to be slightly blue-shifted with a more distinct double-peak when bound to ATTR than in buffer. HS335 also appears to have a slightly blue-shifted emission when bound to ATTR, as well as a blue-shift in emission of the samples on day 2 compared to day 1. BTD-2 also appears to be blue-shifted when bound to fibrils compared to in buffer, see appendix A.

It is interesting to compare the spectra of the chosen ligands to those belonging to Thioflavin-T (ThT), which is a standard amyloid ligand. The ligands X34, HS335 and HS336 all have much higher intensities when bound to ATTR at pH 7.4 than ThT, which is promising for their use as amyloid ligands. Like X34, ThT also shows an increase in intensity of emission from probe bound to ATTR after 24 h, however, this increase is much larger for ThT and takes place at pH 7.4. The probe ThT is less useful at pH 2.0 due to its low intensity, however there does seem to be a slight increase in emission intensity from ATTR after 24 h at this pH as well.

Plate Reader Binding Curves

In a binding curve for a fluorescent ligand, higher intensity of emission at lower concentrations indicates that the ligand binds well and thus smaller concentrations are needed to reach high intensities. The binding curves of HS336 to ATTR fibrils and native WT-TTR tetramers display significant differences in intensity of emission, particularly up to 1000 nM concentration of HS336. This difference in intensity is observable down to concentrations as low as 125 nM. The difference is slightly smaller 24 h later, yet still significant. There is a slight decrease in intensity for all three samples after 24 h, likely caused by some photobleaching from repeated measurements and exposure to light during handling of the samples.

Between 2000 nM and 4000 nM, the curves of both HS336 bound to ATTR and native WT-TTR seem to increase at the same rate as HS336 in solution, pointing to both TTR types possibly being saturated with ligand, and the additional increase in intensity being dominated by an increase in free HS336 in the solution, rather than an increase in HS336 bound to TTR. However, more data points between 2000 nM and 4000 nM are required to fully settle this hypothesis.

The binding curves of X34 display many of the characteristics seen for HS336, with the intensity of X34 bound to WT-TTR and ATTR being much higher than the free X34 in solution, and the intensity of ATTR being significantly higher than WT-TTR between 1250 nM and 2500 nM. However, at lower concentrations than 1250 nM, X34 bound to WT-TTR has a higher intensity of emission than ATTR, before the intensity decreases after 1250 nM. This decrease is interesting and could validate the two-site model for ligand binding sites on the WT-TTR tetramer. The ligands prefer binding to the first binding site and thus only one ligand will bind to each molecule initially, leading to a rapid increase in fluorescence intensity of the ligand upon binding. Eventually, the first binding site will fill up and ligands will start binding to the second site, leading to self-quenching and thus lower intensities. Taken together with the FRET measurements, the results indicate that X34 undergoes self-quenching in close proximity to other X34 molecules. (more below, section 5.1.6) The binding sites of ATTR are less characterized, but the increase in intensity becomes notably less steep after 1250 nM, and it is possible that there would eventually be a decrease in intensity for ATTR as well, once the primary binding sites of the fibrils are saturated with X34. The concentrations needed to reach self-quenching of X34 for both WT-TTR and ATTR will also be discussed further in connection to the FRET results (section 5.1.6).

5.1.2 Absorptive and Emissive Properties

Measuring the photophysical properties in a variety of solvents is useful to interpret the molecular characteristics of a fluorophore, based on how they are affected by the solvent environment, and hence a photophysical study was performed in a number of solvents for each of the ligands.

The Stokes shift is one of the most important fundamental spectral properties. Long Stokes shifts are favorable as it makes the fluorophores easier to image due to the smaller overlap between the absorption and emission spectra. The change in the length of the Stokes shift in different solvents can also reveal general characteristics of a fluorophore. All three amyloid ligands have Stokes shifts longer than 100 nm in PBS, meaning they will likely have large Stokes shift in cell experiments as well due to the similarity of PBS to the cell environment, making the ligands easier to image. For many fluorophores, the Stokes shift will increase in more polar solvents, often due to the excited state being more polar than the ground state and consequently being stabilized in a lower energy state with more polar solvents, leading to lower energies and longer wavelengths of emission. Both X34 and HS336 seem to follow this rule, with both having their shortest Stokes shifts in the most non-polar solvents, CHCl_3 and THF, and their longest shift in the most polar solvent, PBS. HS335 has its shortest Stokes shift in PBS and does not seem to have a relation between polarity and length of Stokes shift.

The ligand X34 displays a significant red-shift for both absorption and emission

in DMSO. Both absorption and emission of HS335 are also slightly red-shifted in DMSO, while HS336 seems unaffected. Fluorophores with excited states that are more polar than the ground state will see a red-shift in more polar solvents, which could explain this shift in DMSO for X34 and HS335, as it is a highly polar solvent. However, MeOH, EtOH and PBS are all more polar than DMSO. These solvents should give even larger red-shifts if this was the only reason, and it is therefore likely that the red-shift is affected by other factors in addition to polarity, like DMSO being aprotic while the other three solvents are protic. Though less red-shifted than DMSO, the emission of X34 and HS335 is also more red-shifted in the polar solvents than in the non-polar ones, i.e. CHCl_3 . This is in line with normal solvatochromism.

The ligand X34 exhibits a distinct double-peaked emission in both THF and CHCl_3 . These solvents are both highly non-polar, so X34 is likely affected by the non-polarity somehow. The other ligands are not affected the same way, and have broad single-peaked emission in CHCl_3 .

The solvent that stands out the most for HS335 is PBS, as the ligand has a very broad absorption spectrum unlike any other probes in PBS. This could point to HS335 not being dissolved properly in PBS, leading to it absorbing light across the whole spectrum by e.g. scattering. This could also affect binding to amyloids and behavior within cells.

The ligand HS336 exhibits anomalous solvatochromism, being blue-shifted in PBS and red-shifted in CHCl_3 . This suggests that the ground state of HS336 is more polar than the excited state, which is unusual. Both the other two ligands show normal solvatochromism, if any, and likely have more polar excited states than ground states. Negative solvatochromism was previously observed for another amyloid ligand, bTVBT4, see Todarwal et al. (2021) where it was used to stain Tau amyloids. [84]

X34 shows a small variation in molar extinction coefficient for different solvents, in the range of $48200 - 60400 \text{ M}^{-1}\text{cm}^{-1}$. There is a possible relation between polarity of the solvents and size of the molar extinction coefficient for X34, as THF and CHCl_3 give the lowest values. However, DMSO and PrOH give the highest values, suggesting the coefficient is also affected by other factors than polarity. HS335 and HS336 both show larger variations in their molar extinction coefficients between solvents, and they both also have higher values in most solvents than X34. HS335 and HS336 both show a clear relation between polarity and size of the molar extinction coefficient, with the most non-polar solvents giving the highest extinction coefficients, and vice versa. Anomalous solvatochromic fluorophores have been found to have increased molar extinction coefficients as well as red-shifted absorption in non-polar solvents. The opposite should be true for positive solvatochromic fluorophores, but has not been explicitly shown. [85] This fits well with the calculated extinction coefficients of HS336, which exhibited anomalous solvatochromism, but is less in

line with the spectroscopic data found for HS335, which exhibited a weak positive solvatochromism, if any.

5.1.3 Quantum Yield (QY)

For X34, there seems to be a relation between the polarity of the solvent and size of the QY, with THF and CHCl_3 giving the highest QYs and PBS the smallest. This is in line with X34 exhibiting normal solvatochromism, as the QY and fluorescence lifetime will both decrease with polarity of the solvent. The QYs of HS335 and HS336 do not seem to follow any obvious patterns with polarity.

HS335 has its highest QY in PBS, at almost three times the value of its second largest QY. This is likely a consequence of the strangely shaped absorption spectra of HS335 in PBS. Absorption of photons across the whole visible spectrum will lead to a lower maximum absorption, as the absorption is more widely spread out. Subsequently, lower values of maximum absorption will affect the linear relation between maximum absorption and total fluorescence emission, giving a higher value of QY.

5.1.4 Fluorescence Lifetime

The fluorescence lifetime of a fluorophore will be affected by the solvent. For fluorophores where the excited state is more polar than the ground state, the decay time will usually become longer in less polar solvents, as the molecules are more relaxed and not forced to be quenched or emit light. This seems true for X34, which has a substantially longer lifetime in THF and CHCl_3 , both of which are highly non-polar solvents. The lifetime then decreases for all the other solvents, with MeOH and PBS giving the shortest lifetimes, consistent with them being the two most polar solvents.

There does not seem to be any distinct relation between polarity and fluorescence lifetime for HS335 and HS336. The ligand HS335 has a much longer lifetime in PBS than in any other solvents, which could be related to its unusual absorption spectrum in PBS, likely caused by poor solubility in this solvent. Apart from the lifetime of HS335 in PBS, all the lifetimes of HS335 and HS336 are close to or below the instrument limit of 100 ps. This means that there is a higher probability that they are inaccurate, with the chance increasing for lower values of the lifetimes. Most of the lifetimes of HS335 and HS336 are thus too short to be accurately detected with the TCSPC instrument used. This is advantageous when it comes to amyloid detection if the lifetime substantially increases upon amyloid binding.

All the fluorescence lifetimes were found from fitting the decay to a single exponential function. For simple samples such as a single type of dissolved fluorophore in solution, a single exponential fit should provide accurate results as the decay will not be composed of multiple lifetime components from different types of fluorophores or fluorophores in different states. When performing more

advanced lifetime measurements, such as the later experiments measuring the lifetime of ligands bound to TTR, double exponential fits are used as they can more accurately discern whether there are multiple lifetime components in a sample due to inhomogeneities and different binding sites.

5.1.5 Photophysical Properties of X34 Bound to Insulin and ATTR Fibrils

The intensity of both the excitation and emission spectra of X34 increases significantly when bound to ATTR and insulin fibrils, with the intensity of emission increasing the most when bound to ATTR. The excitation spectrum of X34 bound to insulin is higher than when bound to ATTR, however, this is likely due to the chosen emission wavelength for the excitation scan of ATTR giving an inaccurately low excitation spectrum. The real excitation spectrum of ATTR is expected to be at a similar height to the emission spectrum.

The fluorescence lifetime of X34 increases considerably when bound to both ATTR and insulin fibrils, with a slightly larger increase when bound to ATTR. The decay of X34 bound to insulin fibrils was fitted to a double exponential expression, while the decay of X34 bound to ATTR was fitted to a single exponential expression like the previously found lifetimes of ligands in solution. This is because the decay from the insulin fibrils showed a curve that could not be fitted well with just a single exponential fit, while the decay from the ATTR fibrils fit well to the straight line of a single exponential fit. One possible explanation for the fluorescence lifetime fitting better to a double decay is that there are multiple binding sites, leading to several different lifetime components among the ligands bound to the fibrils, that cannot be well described by a single exponential fit.

5.1.6 Fluorescence Resonance Energy Transfer (FRET)

As both the intensity of emission and fluorescence lifetime of Tryptophan (Trp) decreased with the addition of X34, it can be concluded that X34 binds close enough to Trp in both WT-TTR and ATTR to induce FRET.

As the emission spectrum of Trp overlaps with the absorption spectrum of X34, energy is transferred directly between the two molecules without the release of a photon, resulting in the quenching of the emission intensity of Trp. This effect will increase with the number of X34 molecules in solution, until the TTR molecules become saturated with X34. Adding additional X34 leads to self-quenching of its emission intensity, giving a maximum fluorescence intensity of X34 at a certain concentration before it starts to decrease. This concentration was different for the WT-TTR tetramers and ATTR fibrils, reaching a maximum intensity from X34 at 0.4 μM and 3.5 μM , respectively. This difference in FRET for the WT-TTR tetramers and ATTR fibrils indicates that the fibrils remain amyloidic for experiments performed at pH 7.4 in room temperature and do not refold into native tetramers during the extension of the experiments.

The self-quenching of X34 likely occurs due to the two ligand binding sites on a WT-TTR tetramer, as discussed in section 4.1.1. X34 is hypothesized to prefer binding the first site, but will eventually start filling the second site as well, leading to self-quenching due to the proximity of the two sites. This would indicate a difference in magnitude of the two dissociation constants, $K_{d,1} < K_{d,2}$, leading to a difference in affinity for the two sites, see section 2.1.7. As it takes longer to observe self-quenching for X34 bound to ATTR, it may point to ATTR having different binding site configurations from the native tetramers.

The fluorescence lifetimes of Trp in both the ATTR fibrils and the native WT-TTR tetramers decrease with the addition of X34, with the decrease being slightly larger for WT-TTR. This decrease in lifetime occurs because quenching depopulates the excited state without fluorescence emission, leading to a shortened lifetime. Static quenching does not lead to a decrease in the fluorescence lifetime, as only the fluorescent molecules are observed, indicating that both WT-TTR and ATTR undergo dynamic quenching.

If a fluorescence quenching process is dynamic, the decrease in fluorescence intensity can be fitted to a linear function that will be equivalent to the linear decrease in fluorescence lifetime, as described in section 2.2.4. Neither of the samples could be fitted to a single linear function, however the data points of both could be split in two and fitted to two separate linear functions, giving two better fits than with a single linear function. The data fitting with two separate linear functions corroborates the two-site binding model for WT-TTR, as the first part of the concentration data corresponds to the binding of X34 to the first site, and the second part to the binding to the second site. From the Stern-Volmer plot, the rate of the quenching of Trp is accurately assessed, with a steeper linear function corresponding to a larger decrease in intensity of emission with addition of the quencher. This fits with the first part of the data having a steeper slope than the second part for both samples, as the overall decrease in intensity from Trp upon binding of X34 to the second site will be smaller if the Trp molecule has already been quenched by the binding of X34 to the first site.

The average fluorescence lifetimes of WT-TTR and ATTR alone and with two added concentrations of X34 were also added to the Stern-Volmer plot, but no linear fits were made as it was deemed less relevant due to the lack of data points. For the lifetimes, multiple binding spots for X34 with different configurations will give several different lifetime components that will need exponential functions of higher powers to be accurately described. Identifying the multiple binding sites on TTR will thus require multiple decay models, and generally be more difficult than using the intensity quenching data. More data points for the lifetimes should also be collected if this is to be attempted.

As each sample was fitted to two separate linear functions, two separate bimolecular quenching constant were also calculated for each sample. The corresponding constants for WT-TTR and ATTR are similar in value, with the

value for WT-TTR being slightly higher for lower concentrations, and the value for ATTR slightly higher for higher concentrations. All the calculated constants are significantly lower than the normal value for diffusion-controlled quenching ($1 \cdot 10^{10} \text{M}^{-1} \text{s}^{-1}$), indicating some shielding of the fluorophore or low quenching efficiency. [56]

5.2 Confocal Laser Scanning Microscopy (CLSM)

Several imaging sessions were performed on the amyloid ligands with ATTR fibrils, both in PBS and in the HEK-293 and SH-SY5Y cell models. It was aimed at finding an optimal protocol for introducing ATTR and ligands to cells, which will be discussed here. The interaction of each of the ligands with both cell models will also be compared.

5.2.1 Comparing Insulin and ATTR Fibrils

The ligand HS335 seems to have a high affinity for some small artifacts in the insulin fibrils, and have stained them intensely while the remainder of the fibril remains faintly stained. This is different from the staining of ATTR by HS335, where the whole fibril is stained efficiently. Insulin is known to exhibit polymorphism, as detailed in section 2.1.6. It is therefore possible that HS335 has an affinity for only one of these configurations of insulin fibrils, causing the uneven staining of the fibrils. Further studies would need to be performed to confirm this. The uneven staining could also be a consequence of the solubility issues of HS335 in PBS, see section 5.1.3. The ligand X34 stained both the ATTR and insulin fibrils intensely, and seems to not have higher affinity for any particular structure in either of the fibrils.

For the insulin fibrils, there seems to be some co-staining with CellMask Deep Red (CM) that is not present for ATTR fibrils. The CM has stained the exterior parts of the insulin fibrils, while X34 has stained the center of the fibrils. This is likely due to the net positive surface charge of insulin fibrils at neutral pH, and CM containing amphipathic molecules that have a lipophilic moiety and a negatively charged hydrophobic dye that work together to "anchor" the stain to the cell membrane. [30, 80]

When added to HEK-293 cells, the ATTR fibrils seem to enter the cells, while the insulin fibrils cluster onto the outside of the cell membrane. One likely reason for this is the size of the fibrils, as the insulin fibrils appear larger both in PBS and with HEK-293 cells. Hence we conclude that the insulin amyloid is of the fibril type and the TTR amyloid of a more filamentous type.

The intensity of both X34 and HS335 increases when bound to both fibril types, and HS335 is also red-shifted when bound to insulin fibrils. X34 exhibits a slight red-shift when bound to both fibril types. In the later emission measurements of

X34 in HEK-293 cells, X34 is more red-shifted with ATTR than with insulin fibrils.

The lifetime of X34 increases upon binding to both ATTR and insulin fibrils in HEK-293 cells, with a value slightly below the lifetime of X34 bound to both fibril types in PBS, found from the TCSPC measurements.

5.2.2 ATTR Incubation Time

A key concept for developing a standard protocol for introduction of ATTR into cells and staining with amyloid ligands was the health of the cells. Both the amyloid ligands and ATTR fibrils can be toxic to cells at high concentrations, and thus keeping the cells healthy was an important part of the process. Cells will show clear changes in morphology when exposed to toxic components, with typical visual changes being that the cells contract and loosen from the well plate, giving them a more spherical shape than the stretched out shape typical of healthy cells. Dead cells can typically be discerned via the commercial stains, particularly DRAQ5, as their inner morphology will be different from living cells.

From the incubation trial, some ATTR fibrils seemed to have entered the cells after 24h, but were stained to a lesser extent than fibrils incubated for 48h. The cells appeared slightly more wrinkled and clustered together after 72h incubation time, pointing to the cells possibly being negatively affected by being exposed to ATTR and ligands for a long amount of time. The incubation time was therefore chosen to be between 36 – 48h for subsequent experiments, to maximize the amount of cells containing ATTR fibrils and their staining by the ligands without compromising the health of the cells. This worked well for the remaining experiments.

However, what seemed to have an even larger impact on the health of the cells than the incubation time was the amount of time they were left to adhere to the ibidi wells before ATTR and amyloid ligands were added. Through observations from the various staining processes, it was found that the cells would generally be healthier if they were left to settle and successfully adhere to the ibidi wells for a sufficient amount of time, typically a full 24h before adding ATTR and amyloid ligands.

To ensure the cells would remain healthy for the experiments, lower concentrations of both ATTR and fluorescent ligands were attempted, which will be discussed further in the respective sections of each ligand. It was desirable to find the lowest possible concentration of fluorescent ligands for cell experiments to ensure the experiments were as non-invasive as possible, and lower concentrations of ATTR may be more diagnostically relevant with regards to how low concentrations are possible to detect in cells.

5.2.3 Comparison of X34/ATTR in Two Cell Models

The ligand X34 was able to detect the fibrils at concentrations as low as 1 μM , as long as fibril concentration was kept at 7 μM . At lower concentrations, the results were too faint to be usable. X34 also stained some specific areas in HEK-293 cells more intensely. The even distribution of these stains as well as their presence in all the HEK-293 cells indicate that this is a common cell organelle, i.e. lysosomes. However, as the same staining is not present in the SH-SY5Y cells, it could also be some specific HEK-293 morphology.

As for emission, the intensity of X34 in HEK-293 cells increased significantly when adding ATTR, and a slight red-shift in emission compared to HEK-293 cells without fibrils was also visible. For SH-SY5Y cells on the other hand, there were large discrepancies in the intensity of emission based on what ROI was selected. Thus, changes in emission seems to be a reliable marker for whether a HEK-293 cell contains ATTR, but not for the SH-SY5Y cells.

For the measured fluorescence lifetimes, the opposite was found. The lifetime of X34 with ATTR in HEK-293 cells was almost identical to that of X34 alone in HEK-293 cells, and could not be used to distinguish whether a cell contained ATTR or not. However, for the SH-SY5Y cells, the lifetime of X34 was significantly shortened when adding ATTR, and the lifetime of X34 is thus a possible marker for whether SH-SY5Y cells contain ATTR.

5.2.4 Comparison of HS335/ATTR in Two Cell Models

The ligand HS335 stained the fibrils well at concentrations as low as 1 μM , for fibril concentrations as low as 2 μM . The ligand also stained some part of the SH-SY5Y cells intensely, possibly some specific SH-SY5Y morphology as the same staining was not present in HEK-293 cells.

For HS335 in HEK-293 cells, there was a significant increase in emission intensity with addition of 7 μM ATTR fibrils compared to the emission of HS335 alone in HEK-293 cells. This increase was slightly smaller for 4.7 μM ATTR and for 3.1 μM ATTR the intensity was slightly decreased compared to the emission of HS335 alone. Thus, the change in emission intensity is likely only able to distinguish HEK-293 cells with ATTR from those without at sufficiently high concentrations of ATTR. The emission intensity of HS335 in SH-SY5Y cells was only measured at one concentration of ATTR, 7 μM , but showed the same significant increase in intensity for this concentration as was seen in the HEK-293 cells. It is thus likely that the emission at lower concentrations will follow the pattern seen in the HEK-293 cells as well, but further studies are needed to confirm this.

The average lifetime of HS335 decreases in HEK-293 cells with ATTR compared to HS335 alone in HEK-293 cells, however, this decrease is not that significant and there are large variations in the measured lifetimes for HS335 in HEK-293 cells both with and without ATTR, and thus further studies are needed to determine

whether the change in fluorescence lifetime is a reliable marker for ATTR presence. No clear pattern between the different concentrations of ATTR and the fluorescence lifetime of HS335 was found. The lifetime of HS335 in SH-SY5Y cells was only measured for one concentration of ATTR, 7 μ M, but two different types of ROIs were chosen when measuring the lifetime, a diffusely fluorescent area outside the cells and a brightly fluorescent area inside the cells. The lifetime was longer than in SH-SY5Y cells without ATTR for both ROIs, with the increase being most significant for the bright areas inside the SH-SY5Y cells. The length of fluorescence lifetime of HS335 is thus possibly a good indication for whether a SH-SY5Y cell contains ATTR or not.

5.2.5 Comparison of HS336/ATTR in Two Cell Models

The ligand HS336 showed signs of cytotoxicity for higher concentrations of ligand as the cells appeared shriveled and clustered at concentrations of 5 – 7 μ M of HS336. It was discussed whether it was a combination of the high concentrations of both the ATTR fibrils and HS336, however, none of the other ligands gave the same reaction in cells at the same fibril and ligand concentrations, so HS336 is likely to be significantly more cytotoxic than the other ligands. Fortunately, HS336 stained the fibrils intensely at lower concentrations, with concentrations as low as 1 μ M still giving good visualization of the cells and fibrils. The cells appeared to be under less stress at this concentration, and thus HS336 is still a viable amyloid ligand as long as concentrations are kept below 1 – 2 μ M. Cytotoxicity studies should be performed to confirm these results.

Like HS335, HS336 also seems to stain some parts of the SH-SY5Y cells intensely, further indicating that this is some specific SH-SY5Y morphology.

The average emission of HS336 inside both HEK-293 and SH-SY5Y cells increases significantly with addition of ATTR fibrils, indicating that it could be usable as a measure of whether the cells contain ATTR or not.

The fluorescence lifetime results from HS336 are less clear-cut for both cell lines. In HEK-293 cells, the fluorescence lifetimes measured from HS336 with 7 μ M ATTR are significantly longer than HS336 alone. However, one of the measured lifetimes of HS336 with ATTR is close in value to, and even slightly shorter than, the lifetime of HS336 in HEK-293 cells without ATTR fibrils. This could possibly indicate that this specific cell did not contain ATTR, and that the lifetime consistently increases to above 1000 ps if there is ATTR present, but further studies are needed to confirm this. For SH-SY5Y cells, two types of ROIs were chosen, a whole cell and a fibrillar structure outside of the cells. The average lifetimes found for these were almost identical, and slightly longer than the lifetime of HS336 alone in SH-SY5Y cells. However, some of the measured lifetimes for cells containing ATTR were shorter and close in value to cells without ATTR. This could imply that these cells do not contain ATTR and that the much longer values measured for some of the cells with ATTR (closer to 900 ps) are accurate. If this

is true, the fluorescence lifetime of HS336 would be a good indication of whether a SH-SY5Y cell contains ATTR, but further studies are needed.

5.3 Discussion of the TTR Two-Site Model in Relation to the Cell Model Studies

Finally, the most interesting results from the photophysics section, the corroboration of the two-site model for native TTR by the FRET and binding curve results, are here compared to the results of the cell model studies.

As discussed earlier, the second ligand binding site on native TTR likely has a higher dissociation constant than the first site, $K_{d,1} < K_{d,2}$, giving the distinct shift in quenching efficiency shown in the FRET results. The ligand binding sites on ATTR are less well characterized, but it is assumed that something similar to the binding to the native TTR is occurring. This could prove troublesome for the cell model experiments, as ATTR may "release" ligands inside the cells, due to the ligands likely having a lower dissociation constant and higher affinity for some parts of the cells than $K_{d,2}$. To avoid this, the concentration of ATTR should be kept sufficiently higher than the concentration of ligand in order to ensure binding of ligands mostly to the first ligand binding site, and thus achieving less "release" inside the cells.

Chapter 6

Conclusions and Suggested Future Studies

In previous chapters, the photophysical characteristics of the fluorescent amyloid ligands and their behavior in HEK-293 and SH-SY5Y cells with Amyloid Transthyretin (ATTR) were discussed, and the key results will be summarized here and concluded. A number of suggested future studies will also be proposed.

Conclusion

The aim of the project was to select the most promising fluorescent ligands for use with ATTR fibrils and perform a photophysical study on these ligands for comparison with a cell model study.

The probes X34, HS335 and HS336 were found to be the most promising amyloid ligands from the plate reader screening, and their photophysical properties were subsequently measured, including QY and fluorescent lifetime, in addition to a binding curve study performed on X34 and HS336 and a FRET study with X34. All three amyloid ligands had low QY in PBS, with a significant increase in intensity upon binding ATTR. HS335 and HS336 showed low QYs in all solvents, and are thus possibly more universally usable than X34. Both X34 and HS336 were found to have very low lifetimes in PBS, with significant lengthening of the lifetimes when introduced to cells and upon ATTR binding. HS335 had a much longer lifetime in PBS, giving a smaller change when binding to ATTR or added to cells.

One of the more interesting results were from the FRET study of the binding of X34 to ATTR and WT-TTR, where the quenching of the intensity of emission from Trp in the TTR molecules could be fitted to two distinct linear functions for both ATTR and WT-TTR. This corroborates the two-site model for native WT-TTR, where X34 will self-quench upon binding to the second ligand binding site on WT-TTR. The ligand binding sites are less characterized for the amyloid form, but as

ATTR seems to behave similarly, it can be assumed that the binding has similarities to ligand binding to the two sites on native WT-TTR. These results were further corroborated by the binding curve study on X34, where the intensity of emission from X34 bound to WT-TTR decreased at higher concentrations.

One of the main objectives of the cell model study was the development of a standard protocol for transfection of ATTR into human cell lines and staining with fluorescent amyloid ligands. The optimal incubation time was found to be between 36 – 48h, which maximizes staining intensity without compromising the health of the cells. Fibril concentration was mostly kept at 7 μ M, but concentrations as low as 2 μ M were also attempted and successfully visualized using HS335. Lower concentrations may have higher diagnostic relevance and should be explored further.

With regard to ligand concentration, concentrations as low as 1 μ M were able to visualize ATTR fibrils at a concentration of 7 μ M for all three ligands. Lower fibril concentrations were attempted for X34 and HS335, but only HS335 was able to visualize these. No cytotoxicity was apparent at 1 μ M for any of the ligands. As for DRAQ5, a concentration of at least 10 μ M was needed to successfully stain the nuclei of HEK-293 cells, while 5 μ M was sufficient for staining the SH-SY5Y cells.

There were large differences in the effect of addition of ATTR to cells on the emission intensity and fluorescence lifetime of the amyloid ligands. Increase in emission intensity seems to be a reliable marker for ATTR presence for all the ligands in both cell lines, except for X34 in SH-SY5Y cells, where no conclusive changes in emission were found. As for the fluorescence lifetime, significant changes were found for X34 and HS335 in SH-SY5Y cells, as well as HS336 in HEK-293 cells. HS336 also demonstrated a small increase in average lifetime for SH-SY5Y cells with ATTR, with large variations in the individual lifetimes. Some were significantly longer than in the SH-SY5Y cells without ATTR fibrils, while others were almost identical in value to the cells without fibrils, possibly due to some cells not containing ATTR, in which case the lifetime of HS336 is a highly accurate measure of ATTR entry into SH-SY5Y cells. No significant changes in lifetime were found for X34 and HS335 in HEK-293 cells.

Future Studies

This thesis lays the ground work for future studies of amyloid fibrils through the use of human cell models. The protocol developed for ATTR transfection should be improved further and tested for other types of amyloid proteins to determine if it can be considered a general procedure for transfection of amyloids into human cells.

A cytotoxicity study should be performed on each of the fluorescent amyloid ligands. It was determined that the ligands can visualize ATTR at ligand concentrations as low as 1 μ M, and the cells showed no signs of stress at

this concentration. This should be confirmed through a cytotoxicity study, particularly for HS336 as the ligand showed clear signs of cytotoxicity at higher concentrations.

Mutant forms of TTR and their amyloid forms should also be investigated, as mutant TTR amyloidosis causes diseases such as Familial Amyloid Polyneuropathy (FAP). The mutants should be characterized in the same way that native and amyloid WT-TTR were characterized in this thesis, and compared with the results found for the WT-TTR.

The FRET experiments could be improved through the use of FLIM for the lifetime measurements, as it makes selection of an ROI only containing Trp possible. A deeper investigation of the lifetimes should also be performed, in order to see if the data would be consistent with the two-site model. A FRET study of X34 bound to native and amyloid TTR in cells could also be attempted, using FLIM-FRET, as it could provide critical data for how the binding of ligands to ATTR changes inside cells compared to in solution.

The determination of presence of ATTR fibrils inside the cells was one of the more challenging tasks in this thesis, and its success is still uncertain in some instances. The considerable increase in emission intensity measured in cells with added ATTR compared to normal cells, as well as the significant changes in fluorescence lifetime measured for some, imply that the transfection protocol was successful and that the ATTR fibrils have entered the cells. However, fibrils located on the outside of the cells may also contribute to similar changes, and further cell model studies with a deeper investigation into the changes in photophysical properties of ligands in cells caused by addition of ATTR fibrils should be performed, in order to more reliably determine the presence of ATTR inside the cells. This is particularly relevant for the FLIM data for cells without ATTR, in order to get more reliable data for the variation of the fluorescence lifetime in cells with only probe. This would aid in conclusively determining whether the changes in lifetime upon addition of ATTR are actually significant or merely explained by this variation.

X34 appeared to stain some smaller bright areas in HEK-293 cells, regardless of the presence of ATTR fibrils, while HS335 and HS336 stained some brighter areas in SH-SY5Y cells. It was hypothesized that these could be lysosomes, however, the LysoTracker Deep Red (LT) used in this project stained the cells very faintly and photobleached too rapidly to be of use for investigating this. Further studies should be performed to determine what the ligands are staining to make sure this does not interfere with ATTR detection.

Bibliography

- 1 Zheng, J. C., & Chen, S. (2022). Translational neurodegeneration in the era of fast growing international brain research. *Transl Neurodegener*, 11(1), 517–527. <https://doi.org/10.1186/s40035-021-00276-9>
- 2 Koo et al., E. H. (1999). Amyloid diseases: Abnormal protein aggregation in neurodegeneration. *Proc Natl Acad Sci U S A.*, 96(18), 9989–9990. <https://doi.org/10.1073/pnas.96.18.9989>
- 3 Araki et al., K. (2019). Parkinson’s disease is a type of amyloidosis featuring accumulation of amyloid fibrils of α -synuclein. *Proceedings of the National Academy of Sciences*, 116(36), 17963–17969. <https://doi.org/10.1073/pnas.190612411>
- 4 Nisbet, M. R., & Götz, J. (2018). Amyloid- and tau in alzheimer’s disease: Novel pathomechanisms and non-pharmacological treatment strategies. *J Alzheimers Dis.*, 64(s1), 517–527. <https://doi.org/10.3233/JAD-179907>
- 5 Sun et al., F. (2021). A quinoline derived d-a-d type fluorescent probe for sensing tetrameric transthyretin. *Bioorganic & Medicinal Chemistry Letters*, 52. <https://doi.org/10.1016/j.bmcl.2021.128408>
- 6 Shirani et al., H. (2017). Synthesis of thiophene-based optical ligands that selectively detect tau pathology in alzheimer’s disease. *Chem. Eur. J.*, 23(67), 17127–17135. <https://doi.org/10.1002/chem.201703846>
- 7 Styren et al., S. D. (2000). X-34, a fluorescent derivative of congo red: A novel histochemical stain for alzheimer’s disease pathology. *J Histochem Cytochem*, 48(9), 1223–1232. <https://doi.org/10.1177/002215540004800906>
- 8 Biancalana, M., & Koide, S. (2010). Molecular mechanism of thioflavin-t binding to amyloid fibrils. *Biochim Biophys Acta.*, 1804(7), 1405–1412. <https://doi.org/10.1016/j.bbapap.2010.04.001>
- 9 Darghal et al., N. (2006). Mechanism of thioflavin t accumulation inside cells overexpressing p-glycoprotein or multidrug resistance-associated protein: Role of lipophilicity and positive charge. *Biochem Biophys Res Commun.*, 343(2), 623–629. <https://doi.org/10.1016/j.bbrc.2006.03.024>
- 10 Wood et al., N. I. (2007). Systemic administration of congo red does not improve motor or cognitive function in r6/2 mice. *Neurobiol Dis.*, 25(2), 342–353. <https://doi.org/10.1016/j.nbd.2006.09.015>

- 11 Berge, N. V. D. (2022). *Pd-pam: Early indicators of nervous system dysfunction in gut-first and brain-first animal models of parkinson's disease*. <https://www.neurodegenerationresearch.eu/wp-content/uploads/2022/06/PROJECT-PDPAM.pdf> (accessed 15.11.2022)
- 12 Fredriksson, M. (2013). *Final report summary - lupas (luminescent polymers for in vivo imaging of amyloid signatures)*. <https://cordis.europa.eu/project/id/242098/reporting> (accessed 15.11.2022)
- 13 Åslund et al., A. (2009). Novel pentameric thiophene derivatives for in vitro and in vivo optical imaging of a plethora of protein aggregates in cerebral amyloidoses. *ACS Chem. Biol.*, 4(8), 673–684. <https://doi.org/10.1021/cb900112v>
- 14 Colon, W., & Kelly, J. W. (1992). Partial denaturation of transthyretin is sufficient for amyloid fibril formation in vitro. *Frontiers in Physics*, 31(36), 8654–8660. <https://doi.org/10.1021/bi00151a036>
- 15 Sundnes, M. L. (2022). Some fluorescent ligands for studies of amyloidosis in cell models.
- 16 Thermo Fisher Scientific Inc. (n.d.[a]). *Introduction to cell culture*. <https://www.thermofisher.com/no/en/home/references/gibco-cell-culture-basics/introduction-to-cell-culture.html> (accessed: 21.04.2023)
- 17 Segeritz, C.-P., & Vallier, L. (2017). Cell culture: Growing cells as model systems in vitro. *Basic Science Methods for Clinical Researchers*, 151–172. <https://doi.org/10.1016/B978-0-12-803077-6.00009-6>
- 18 Thermo Fisher Scientific Inc. (n.d.[b]). *Adherent cell culture vs. suspension cell culture*. <https://www.thermofisher.com/no/en/home/references/gibco-cell-culture-basics/cell-lines/adherent-vs-suspension-culture.html> (accessed: 25.04.2023)
- 19 Merck. (n.d.). *Oxidative stress in cell culture*. <https://www.sigmaaldrich.com/NO/en/technical-documents/technical-article/cell-culture-and-cell-culture-analysis/mammalian-cell-culture/oxidative-stress> (accessed: 06.05.2023)
- 20 Thermo Fisher Scientific Inc. (n.d.[c]). *Brand™ Bürker counting chambers*. <https://www.fishersci.se/shop/products/buerker-counting-chambers-2/p-8003572> (accessed: 25.04.2023)
- 21 Taylor-Whiteley et al., T. R. (2019). Recapitulating parkinson's disease pathology in a three-dimensional human neural cell culture model. *Dis Model Mech*, 12(4). <https://doi.org/10.1242/dmm.038042>
- 22 Kovalevich, J., & Langford, D. (2013). Considerations for the use of sh-sy5y neuroblastoma cells in neurobiology. *Methods Mol Biol.*, 1078, 9–21. https://doi.org/10.1007/978-1-62703-640-5_2
- 23 Carruth, L., & Shahbazi, M. (2015). Chapter 2 - estrogen actions in the brain. **in** K. A. Duncan (editor), *Estrogen effects on traumatic brain injury* (pages 11–28). Academic Press. <https://doi.org/10.1016/B978-0-12-801479-0.00002-4>

- 24 Xicoy et al., H. (2017). The sh-sy5y cell line in parkinson's disease research: A systematic review. *Molecular Neurodegeneration*, 12(10). <https://doi.org/10.1186/s13024-017-0149-0>
- 25 Lopes et al., F. M. (2010). Comparison between proliferative and neuron-like sh-sy5y cells as an in vitro model for parkinson disease studies. *Brain Res.*, 14(1337), 85–94. <https://doi.org/10.1016/j.brainres.2010.03.102>
- 26 Beckman Coulter. (n.d.). *An overview of hek-239 cell line*. <https://www.beckman.com/resources/product-applications/lead-optimization/cell-line-development/human-embryonic-kidney-293> (accessed 11.04.2023)
- 27 Graham et al., F. L. (1977). Characteristics of a human cell line transformed by dna from human adenovirus type 5. *J Gen Virol*, 36(1), 59–74. <https://doi.org/10.1099/0022-1317-36-1-59>
- 28 Tan et al., E. (2021). Hek293 cell line as a platform to produce recombinant proteins and viral vectors. *Front. Bioeng. Biotechnol.*, 9. <https://doi.org/10.3389/fbioe.2021.796991>
- 29 National Human Genome Research Institute. (n.d.). *Gamete*. <https://www.genome.gov/genetics-glossary/Gamete> (accessed: 06.05.2023)
- 30 Psonka-Antonczyk et al., K. M. (2012). Nanoscopic and photonic ultrastructural characterization of two distinct insulin amyloid states. *International Journal of Molecular Sciences*, 13(2), 1461–1480. <https://doi.org/10.3390/ijms13021461>
- 31 Wetzels, R. (2013). Amyloid. *Encyclopedia of Biological Chemistry*, 100–104. <https://doi.org/10.1016/B978-0-12-378630-2.00167-5>
- 32 Ahn et al., J.-M. (2017). 6.03 - strategy and tactics for designing analogs: Biochemical characterization of the large molecules. *Comprehensive Medicinal Chemistry III*, 66–115. <https://doi.org/10.1016/B978-0-12-409547-2.12413-8>
- 33 Makin et al., O. S. (2005). Molecular basis for amyloid fibril formation and stability. *Proceedings of the National Academy of Sciences*, 102(2), 315–320. <https://doi.org/10.1073/pnas.0406847102>
- 34 Minh et al., N. N. T. (2023). *Binding of a pyrene-based fluorescent amyloid ligand to transthyretin: A combined crystallographic and molecular dynamics study* [Pre-print].
- 35 Lai et al., Z. (1996). The acid-mediated denaturation pathway of transthyretin yields a conformational intermediate that can self-assemble into amyloid. *Biochemistry*, 35(20), 6470–6482. <https://doi.org/10.1021/bi952501g>
- 36 Jesus et al., C. S. H. (2016). A new folding kinetic mechanism for human transthyretin and the influence of the amyloidogenic v30m mutation. *Int J Mol Sci*, 17(9), 1428. <https://doi.org/10.3390/ijms17091428>
- 37 Tomar et al., D. (2012). Crystallographic study of novel transthyretin ligands exhibiting negative-cooperativity between two thyroxine binding sites. *PloS one*, 7(9), 1–11. <https://doi.org/10.1371/journal.pone.0043522>
- 38 Saldaño et al., T. E. (2017). Evaluating the effect of mutations and ligand binding on transthyretin homotetramer dynamics. *PloS one*, 12, 1–20. <https://doi.org/10.1371/journal.pone.0181019>

- 39 Corazza et al., A. (2019). Binding of monovalent and bivalent ligands by transthyretin causes different short- and long-distance conformational changes. *J. Med. Chem.*, *62*(17), 8274–8273. <https://doi.org/10.1021/acs.jmedchem.9b01037>
- 40 Miroy et al., G. J. (1996). Inhibiting transthyretin amyloid fibril formation via protein stabilization. *Proc Natl Acad Sci U S A.*, *93*(26), 15051–15056. <https://doi.org/10.1073/pnas.93.26.15051>
- 41 Palaninathan et al., S. K. (2008). Structural insight into pH-induced conformational changes within the native human transthyretin tetramer. *Journal of Molecular Biology*, *382*(5), 1157–1167. <https://doi.org/10.1016/j.jmb.2008.07.029>
- 42 Jesus et al., C. S. H. (2012). The v30m amyloidogenic mutation decreases the rate of refolding kinetics of the tetrameric protein transthyretin. *Journal of Spectroscopy*, *27*. <https://doi.org/10.1155/2012/502497>
- 43 Sindrewicz et al., P. (2019). Intrinsic tryptophan fluorescence spectroscopy reliably determines galectin-ligand interactions. *Sci Rep*, *9*, 11851. <https://doi.org/10.1038/s41598-019-47658-8>
- 44 Fanny et al., B.-D. (1990). Failure of tryptophan deficiency to reduce specifically serum levels of transthyretin or albumin in rats. *The Journal of Nutrition*, *120*(12), 1610–1616. <https://doi.org/10.1093/jn/120.12.1610>
- 45 Sun et al., X. (2017). Fluorotryptophan incorporation modulates the structure and stability of transthyretin in a site-specific manner. *Biochemistry.*, *56*(41), 5570–5581. <https://doi.org/10.1021/acs.biochem.7b00815>
- 46 Sörgjerd et al., K. (2008). Prefibrillar transthyretin oligomers and cold stored native tetrameric transthyretin are cytotoxic in cell culture. *Biochem Biophys Res Commun.*, *377*(4), 1072–1078. <https://doi.org/10.1016/j.bbrc.2008.10.121>
- 47 Malmos et al., K. (2017). Tht 101: A primer on the use of thioflavin t to investigate amyloid formation. *Amyloid : the international journal of experimental and clinical investigation : the official journal of the International Society of Amyloidosis*, *24*, 1–16. <https://doi.org/10.1080/13506129.2017.1304905>
- 48 AAT Bioquest. (n.d.). *Spectrum [thioflavin t]*. https://www.aatbio.com/fluorescence-excitation-emission-spectrum-graph-viewer/thioflavin_t (accessed: 01.06.2023)
- 49 Mori et al., W. (2021). Degradation of insulin amyloid by antibiotic minocycline and formation of toxic intermediates. *Sci Rep*, *11*, 6857. <https://doi.org/https://doi.org/10.1038/s41598-021-86001-y>
- 50 Yuzu et al., K. (2020). Insulin amyloid polymorphs: Implications for iatrogenic cytotoxicity. (Paper) *RSC Adv.*, *10*, 37721–37727. <https://doi.org/10.1039/D0RA07742A>
- 51 Zako et al., T. (2012). Cell interaction study of amyloid by using luminescent conjugated polythiophene: Implication that amyloid cytotoxicity is correlated with prolonged cellular binding. *ChemBioChem*, *13*(3), 358–363. <https://doi.org/10.1002/cbic.201100467>

- 52 Corzo, J. (2006). Time, the forgotten dimension of ligand binding teaching. *Biochemistry and Molecular Biology Education*, 34(6), 413–416. <https://doi.org/10.1002/bmb.2006.494034062678>
- 53 Neubig et al., R. R. (2003). International union of pharmacology committee on receptor nomenclature and drug classification. xxxviii. update on terms and symbols in quantitative pharmacology. *The American Society for Pharmacology and Experimental Therapeutics*, 55(4), 597–606. <https://doi.org/10.1124/pr.55.4.4>
- 54 Cleaves, H. J. (2011). Affinity constant. in M. Gargaud et al. (editor), *Encyclopedia of astrobiology* (pages 23–24). Springer Berlin Heidelberg. https://doi.org/10.1007/978-3-642-11274-4_40
- 55 Hargrove et al., A. E. (2010). Algorithms for the determination of binding constants and enantiomeric excess in complex host: Guest equilibria using optical measurements. *New journal of chemistry*, 34(2), 348–354. <https://doi.org/10.1039/b9nj00498j>
- 56 Lakowicz, J. R. (1999). *Principles of fluorescence spectroscopy*. Springer.
- 57 ChemTalk. (n.d.). *Beer-lambert law*. <https://chemistrytalk.org/beer-lambert-law/#:~:text=The%5C%20molar%5C%20extinction%5C%20coefficient%5C%20is,absorption%5C%20coefficient%5C%20or%5C%20molar%5C%20absorptivity.> (accessed: 19.06.2023)
- 58 Lindgren, M. (2023). *Solvent effects and lifetimes* [University Lecture], NTNU.
- 59 BMG LABTECH. (n.d.). *Microplate reader*. <https://www.bmglabtech.com/en/microplate-reader/> (accessed: 20.04.2023)
- 60 Sekar, R. B., & Periasamy, A. (2003). Fluorescence resonance energy transfer (fret) microscopy imaging of live cell protein localizations. *J Cell Biol.*, 160(5), 629–633. <https://doi.org/10.1083/jcb.200210140>
- 61 Hoffman, R. (2013). Cell markers: Green fluorescent protein. in S. Maloy & K. Hughes (editors), *Brenner's encyclopedia of genetics (second edition)* (Second Edition, pages 483–487). Academic Press. <https://doi.org/10.1016/B978-0-12-374984-0.00213-8>
- 62 Hirvonen, L. M., & Suhling, K. (2020). Fast timing techniques in flim applications. *Frontiers in Physics*, 8. <https://doi.org/10.3389/fphy.2020.00161>
- 63 Zickus et al., V. (2020a). Fluorescence lifetime imaging with a megapixel spad camera and neural network lifetime estimation. *Scientific Reports*, 10. <https://doi.org/10.1038/s41598-020-77737-0>
- 64 Datta et al., R. (2020). Fluorescence lifetime imaging microscopy: Fundamentals and advances in instrumentation, analysis, and applications. *Journal of Biomedical Optics*, 25(7). <https://doi.org/10.1117/1.JBO.25.7.071203>
- 65 Picoquant. (n.d.). *Fluorescence lifetime imaging (flim)*. <https://www.picoquant.com/applications/category/life-science/fluorescence-lifetime-imaging-flim> (accessed 19.11.2022)
- 66 Leica Microsystems. (2022). *What is fret with flim (flim-fret)?* <https://www.leica-microsystems.com/science-lab/life-science/what-is-fret-with-flim-flim-fret/> (accessed: 24.05.2023)

- 67 Elprocus. (n.d.). *What is avalanche photodiode : Working & its applications*. <https://www.elprocus.com/avalanche-photodiode/> (accessed: 06.05.2023)
- 68 Zickus et al., V. (2020b). Fluorescence lifetime imaging with a megapixel spad camera and neural network lifetime estimation. *Sci Rep*, 10(20986). <https://doi.org/10.1038/s41598-020-77737-0>
- 69 Yakupova et al., E. I. (2019). Congo red and amyloids: History and relationship. *Biosci Rep.*, 39(1). <https://doi.org/10.1042/BSR20181415>
- 70 Britannica, T. E. o. E. (2017). Azo dye. *in* *Encyclopaedia of everything*. <https://www.britannica.com/science/azo-dye>. (accessed: 10.05.2023)
- 71 Klunk et al., W. E. (1994). Development of small molecule probes for the beta-amyloid protein of alzheimer's disease. *Neurobiology of Aging*, 15(6), 691–698. [https://doi.org/10.1016/0197-4580\(94\)90050-7](https://doi.org/10.1016/0197-4580(94)90050-7)
- 72 Zhang et al., J. (2019). Phenolic bis-styrylbenzo[c]-1,2,5-thiadiazoles as probes for fluorescence microscopy mapping of a plaque heterogeneity. *J. Med. Chem.*, 62(4), 2038–2048. <https://doi.org/10.1021/acs.jmedchem.8b01681>
- 73 Wegenast-Braun et al., B. M. (2012). Spectral discrimination of cerebral amyloid lesions after peripheral application of luminescent conjugated oligothiophenes. *The American Journal of Pathology*, 181(6), 1953–1960. <https://doi.org/10.1016/j.ajpath.2012.08.031>
- 74 Liu et al., H. (2021). Distinct conformers of amyloid beta accumulate in the neocortex of patients with rapidly progressive alzheimer's disease. *Journal of Biological Chemistry*, 297(5), 101267. <https://doi.org/10.1016/j.jbc.2021.101267>
- 75 Björk et al., L. (nodate). *Distinct heterocyclic moieties govern the selectivity of thiophene-vinylene-based ligands towards ab or tau pathology in alzheimer's disease*. [Submitted to European Journal of Organic Chemistry May 2023].
- 76 Rurack, K., & Spieles, M. (2011). Fluorescence quantum yields of a series of red and near-infrared dyes emitting at 600-1000 nm. *Analytical Chemistry*, 83(4), 1232–1242. <https://doi.org/10.1021/ac101329h>
- 77 Orge et al., B. (1999). Variation of densities, refractive indices, and speeds of sound with temperature of methanol or ethanol with hexane, heptane, and octane. *J. Chem. Eng. Data*, 44(5), 1041–1047. <https://doi.org/10.1021/je9900676>
- 78 Stupar et al., D. (2012). Remote monitoring of water salinity by using side-polished fiber-optic u-shaped sensor. *2012 15th International Power Electronics and Motion Control Conference (EPE/PEMC)*, LS4c.4-1–LS4c.4-5. <https://doi.org/10.1109/EPEPEMC.2012.6397458>
- 79 *Instructions for use for infinite m1000 pro* [Rev. No. 1.0]. (2011). Tecan.
- 80 LifeTechnologies. (2014). *Cellmask plasma membrane stains*. https://www.thermofisher.com/document-connect/document-connect.html?url=https://assets.thermofisher.com/TFS-Assets%5C%2FMSG%5C%2Fmanuals%5C%2FCellMask_Plasma_Membrane_Stains_PI.pdf (accessed: 08.12.2022)

- 81 Thermo Fisher Scientific Inc. (n.d.[d]). *Draq5 fluorescent probe solution (5 mm)*. <https://www.thermofisher.com/order/catalog/product/62254?SID=srch-srp-62254> (accessed: 08.12.2022)
- 82 LifeTechnologies. (2013). *Lysotracker and lysosensor probes*. <https://www.thermofisher.com/document-connect/document-connect.html?url=https://assets.thermofisher.com/TFS-Assets%5C%2FSLSG%5C%2Fmanuals%5C%2Fmp07525.pdf> (accessed: 08.12.2022)
- 83 ibidi. (n.d.). *μ-slide 8 well*. https://ibidi.com/chambered-coverslips/13--slide-8-well-ibitreat.html#/25-surface_modification-ibitreat_15_polymer_coverslip_tissue_culture_treated_sterilized/33-pcs_box-15_individually_packed (accessed: 15.12.2022)
- 84 Todarwal et al., Y. (2021). Tau protein binding modes in alzheimer's disease for cationic luminescent ligands. *The Journal of Physical Chemistry B*, 125(42), 11628–11636. <https://doi.org/10.1021/acs.jpcc.1c06019>
- 85 Spange, S., & Mayerhöfer, T. G. (2022). The negative solvatochromism of reichardt's dye b30 – a complementary study. *ChemPhysChem*, 23(14), e202200100. <https://doi.org/https://doi.org/10.1002/cphc.202200100>
- 86 Klingstedt et al., T. (2011). Synthesis of a library of oligothiophenes and their utilization as fluorescent ligands for spectral assignment of protein aggregates. *Organic & biomolecular chemistry*, 9(62), 8356–8370. <https://doi.org/10.1039/c1ob05637a>
- 87 Xue et al., C. (2017). Thioflavin t as an amyloid dye: Fibril quantification, optimal concentration and effect on aggregation. *R. Soc. open sci.*, 4(1). <https://doi.org/10.1098/rsos.160696>
- 88 Neto et al., B. A. D. (2013). 2,1,3-benzothiadiazole and derivatives: Synthesis, properties, reactions, and applications in light technology of small molecules. *Eur. J. Org. Chem*, 2013(2), 228–255. <https://doi.org/10.1002/ejoc.201201161>
- 89 Neto et al., B. A. D. (2015). Benzothiadiazole derivatives as fluorescence imaging probes: Beyond classical scaffolds. *Acc. Chem. Res.*, 48(6), 1560–1569. <https://doi.org/10.1021/ar500468p>
- 90 Arora et al., H. (2020). Molecular tools to detect alloforms of a and tau: Implications for multiplexing and multimodal diagnosis of alzheimer's disease. *Bulletin of the Chemical Society of Japan*, 93(4), 507–546. <https://doi.org/10.1246/bcsj.20190356>
- 91 Björk et al., L. (2022). Proteophenes – amino acid functionalized thiophene-based fluorescent ligands for visualization of protein deposits in tissue sections with alzheimer's disease pathology. *Chemistry*, 28(62). <https://doi.org/10.1002/chem.202201557>

Appendix A

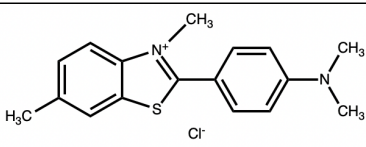
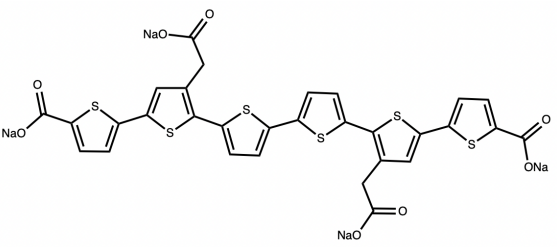
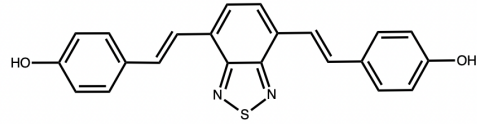
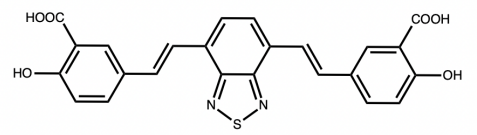
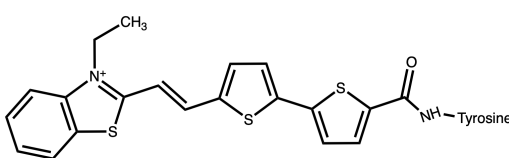
Additional Ligands Screened as Potential Amyloid Probes

The excitation wavelength giving the highest emission was chosen for each probe, however some of the probes also had multiple suitable excitation wavelengths. The structures of the amyloid probes are tabulated in table A.1.

Thioflavin-T (ThT) is a fluorescent dye that is widely considered to be among the "gold standards" for selectively staining and identifying amyloid fibrils both *in vivo* and *in vitro*. ThT exhibits a large increase in fluorescent emission upon binding to amyloid fibrils, making it a powerful tool for amyloid detection. The probe also has high solubility in water. [8] ThT fluorescence has been found to only originate from the dye bound to the amyloid fibrils, and the maximum fluorescence intensity when staining with ThT is mostly decided by the total ThT concentration, rather than the amyloid to ThT ratio. [8, 87] ThT has also been demonstrated to display a dramatic red-shift in excitation and emission maxima upon amyloid binding, from 385 nm to 450 nm for excitation, and from 445 nm to 482 nm for emission. [8]

Since ThT is a standard amyloid ligand, it is useful for comparison with novel amyloid ligands. These should either have an increase in fluorescence intensity when bound to amyloids akin to that of ThT, or a shift in excitation or emission maxima comparable to that of ThT in order to be considered usable probes for detection of amyloid fibrils. Co-staining with ThT is also a commonly used technique to see if novel amyloid probes can detect the same aggregates as ThT or even discern areas not stained by ThT. The emission spectra of ThT in solution and bound to ATTR amyloid fibrils are shown in figure A.1. ThT shows no increase in fluorescence intensity when bound to fibrils at pH 2, but a small increase on day 1 in pH 7.4 and a relatively large increase in pH 7.4 on day 2. This could suggest that ThT takes longer to bind to the amyloid fibrils.

Table A.1: Structure of the various amyloid ligands tested with the Tecan platereader, drawn using ChemDraw. Structures of ThT, BTD-2, BTDSB and bTVBT-Tyr were provided by Linköping University (LiU).

Name	Structure	Ref
ThT		LiU
hx-FTAA		[86]
BTD-2		LiU
BTDSB		LiU
bTVBT-Tyr		LiU

Hexamer Formyl Thiophene Acetic Acid (hx-FTAA) is a Luminescent Conjugated Oligothiophene (LCO), with a backbone comprised of six thiophene rings. hx-FTAA is a non-specific ligand, but has been shown to display selective binding towards protein aggregates and even bind to $A\beta$ species not detected by ThT. It could potentially be highly useful for studying the underlying molecular events of protein aggregation diseases and be utilized for the development of novel diagnostic tools for these diseases. However, the staining of AD pathology by hx-FTAA has only been demonstrated in *ex vivo* tissue. [86]

The emission of hx-FTAA in solution and bound to ATTR fibrils is presented in figure A.2. As the spectra of the ligand with and without fibril were too close to

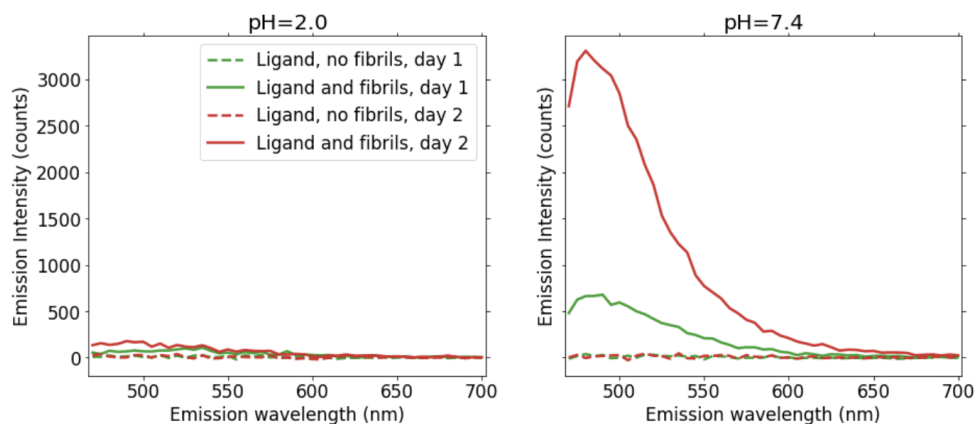


Figure A.1: Emission spectra of Thioflavin-T (ThT) at pH 2 and 7.4, excited at 450 nm and measured using a Tecan microplate reader immediately after sample preparation and once again 24 h later. ($\lambda_{\text{ex}} = 450 \text{ nm}$) 405 nm was also a suitable excitation wavelength for ThT. See section 3.3.3 for sample composition.

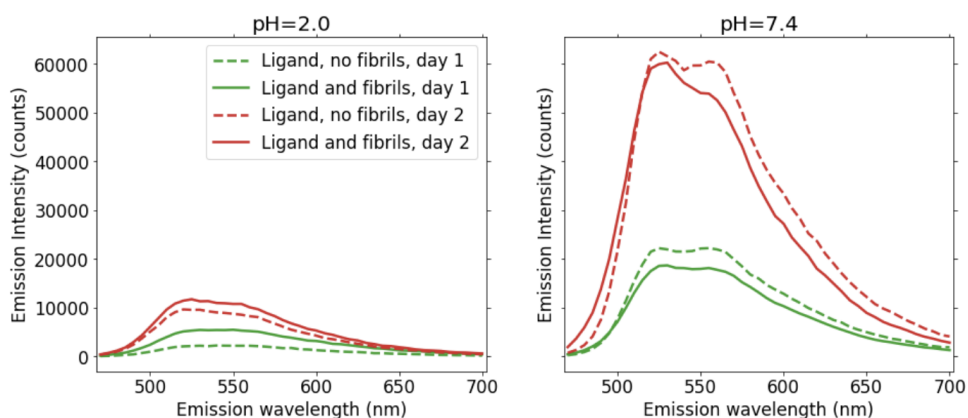


Figure A.2: Emission spectra of hx-FTAA at pH 2 and 7.4, measured using a Tecan microplate reader immediately after sample preparation and once again 24 h later. ($\lambda_{\text{ex}} = 450 \text{ nm}$) All spectra were baseline corrected by data with buffer only. See section 3.3.3 for sample composition.

be clearly distinguishable, it was found to not be usable as an ATTR probe and thus rejected. hx-FTAA showed a very high intensity of emission when bound to fibrils, however, at pH 7.4, the intensity of the ligand without fibrils were actually slightly higher than when bound to fibrils, making it unsuitable for fibril detection at this pH.

2,1,3-Benzothiadiazole (BTD) probes have only been in use for biological analysis for a few years, but show promise for use as fluorescent probes in a number of biological applications. [88, 89] They have several beneficial photophysical characteristics, i.e. large Stokes shifts, high quantum yields, excitation wavelengths

generally within the visible-light region and low levels of photobleaching even after long periods of irradiation. BTD probes also exhibit high stability when stored in solution or as pure solids. [89] **BTD-2** is a BTD derivative, and a non-specific ligand like hx-FTAA.

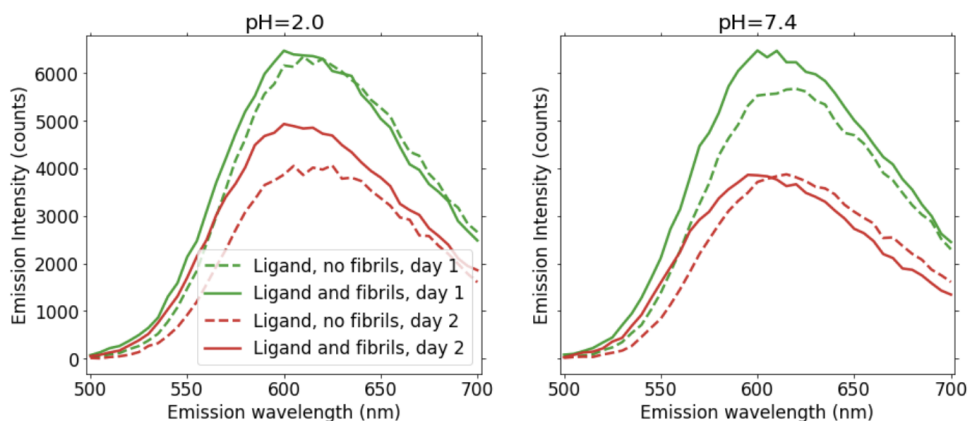


Figure A.3: Emission spectra of BTD-2 at pH 2 and 7.4, measured using a Tecan microplate reader immediately after sample preparation and once again 24 h later. ($\lambda_{\text{ex}} = 480 \text{ nm}$) All spectra were baseline corrected by data with buffer only. See section 3.3.3 for sample composition.

The emission of BTD-2 in solution and bound to ATTR fibrils is shown in figure A.3. Like, hx-FTAA, BTD-2 also shows high fluorescence intensity for pH 7.4, but too small of a difference in intensity between ligand and ligand bound to fibril to be able to reliably distinguish them. However, BTD-2 is also interesting in that it gives a high intensity in pH 2. There also seems to be a slight blue-shift in emission when bound to fibrils, but it was ultimately decided that other probes were of more interest and BTD-2 was rejected.

BTDSB is a Benzothiadiazole Stilbene derivative of X34. Like hx-FTAA and BTD-2, it is a non-specific ligand, but has been shown to have high binding affinity for $A\beta$ fibrils and will intensely stain both $A\beta$ plaques and NFTs in AD brain tissue sections. [72]

The emission of BTDSB in solution and bound to ATTR fibrils is shown in figure A.4. The intensity of emission from probe bound to fibrils is too close to that of probe in solution for BTDSB to be a suitable probe for TTR fibrils. In half the measurements, the intensity of emission from probe in solution is even slightly higher than that from probe bound to fibrils. There seems to possibly be a slight blue-shift in emission when bound to fibrils, although not large enough to reliably distinguish the spectra and BTDSB was rejected.

bTVBT-Tyr is a Bi-Thiophene-Vinyl-Benzothiazole (bTVBT) derivative, which is a novel class of stains that selectively identify different forms of Tau aggregates in AD brains, without significant staining of the $A\beta$ aggregates. [6, 90] bTVBTs are

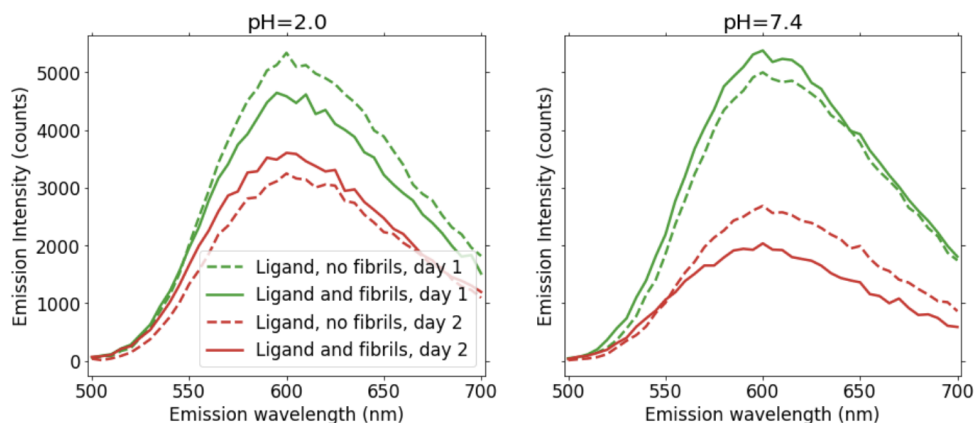


Figure A.4: Emission spectra of BTDSB at pH 2 and 7.4, measured using a Tecan microplate reader immediately after sample preparation and once again 24 h later. ($\lambda_{\text{ex}} = 480 \text{ nm}$) 450 nm was also a suitable excitation wavelength for BTDSB. All spectra were baseline corrected by data with buffer only. See section 3.3.3 for sample composition.

most likely interacting with the repetitive β -sheet structure of the Tau protein, and they function as a molecular scaffold for development of fluorescent ligands that selectively detect Tau deposits in brain sections with AD pathology. [6] Amino acids can be coupled to amyloid ligands to achieve side functionalities with different characteristics, such as polarity, hydrophobicity and charge. Ligands coupled with Tyrosine (Tyr) have shown strong staining towards NFTs and other AD pathologies, verifying that amino acid functionalities have a major impact on the ligand-protein aggregate interaction. [91]

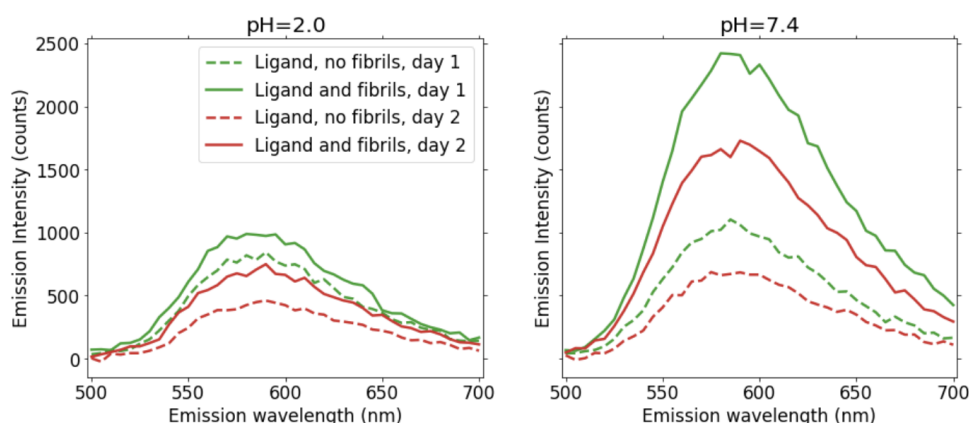


Figure A.5: Emission spectra of bTVBT-Tyr at pH 2 and 7.4, measured using a Tecan microplate reader immediately after sample preparation and once again 24 h later. ($\lambda_{\text{ex}} = 480 \text{ nm}$) All spectra were baseline corrected by data with buffer only. See section 3.3.3 for sample composition.

The emission of bTVBT-Tyr in solution and bound to ATTR fibrils is shown in figure A.5. The difference between unbound probe and probe bound to fibrils is not particularly significant at pH 2, but the probe bound to fibrils shows a much higher intensity of emission at pH 7.4. bTVBT-Tyr could thus be a potential TTR probe at pH 7.4, however it was ultimately decided to move forward with only three probes, X34, HS335 and HS336, with bTVBT-Tyr as a potential alternative if any of these turned out to be unsuitable.

Appendix B

Spectra for Quantum Yield (QY) Calculations

The absorption and emission spectra of Coumarin 153 (C-153) in EtOH, the reference used in the QY calculations, and of X34 in MeOH are shown in figure B.1. The concentrations were chosen to be evenly spaced with the highest being 19 μM for C-153 and 5 μM for X34.

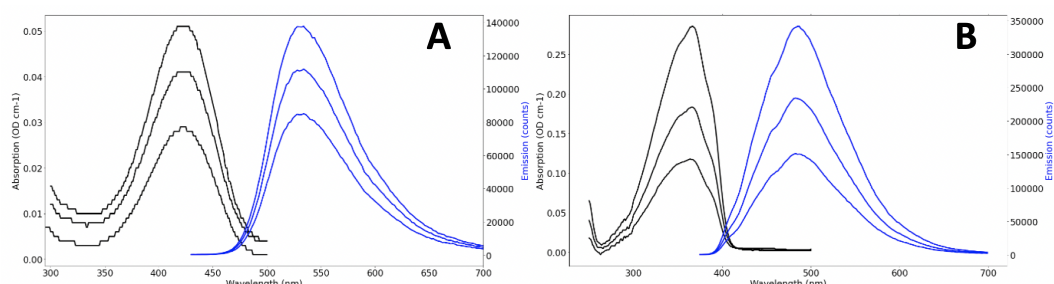


Figure B.1: Absorption and emission spectra of (A) C-153 in EtOH and (B) X34 in MeOH. The spectra were collected at three evenly spaced concentrations. C-153 has a known QY in EtOH, $54.4\% \pm 2.8\%$, and was used as a reference in the QY calculations. [76]

Total emission plotted against maximum absorption for each of the concentrations of C-153 and X34 are displayed in figure B.2, with linear fits in corresponding colors. The highest concentration of X34 (5 μM) yielded a maximum absorption of 0.285 OD cm^{-1} , which is high enough for possible re-absorption effects that may lead to measuring a too low emission, see section 3.3.1 for details. Looking at the data points, the emission is slightly lower than the expected linear increase for the measured absorption at this concentration, however, not significant enough for this data point to be discarded. The slopes found from the linear fitting of these data points were used to calculate the QY of X34 in MeOH, with correction for the difference in solvent. This process was repeated for X34 in all other solvents,

as well as for HS335 and HS336, all with C-153 in EtOH as a reference.

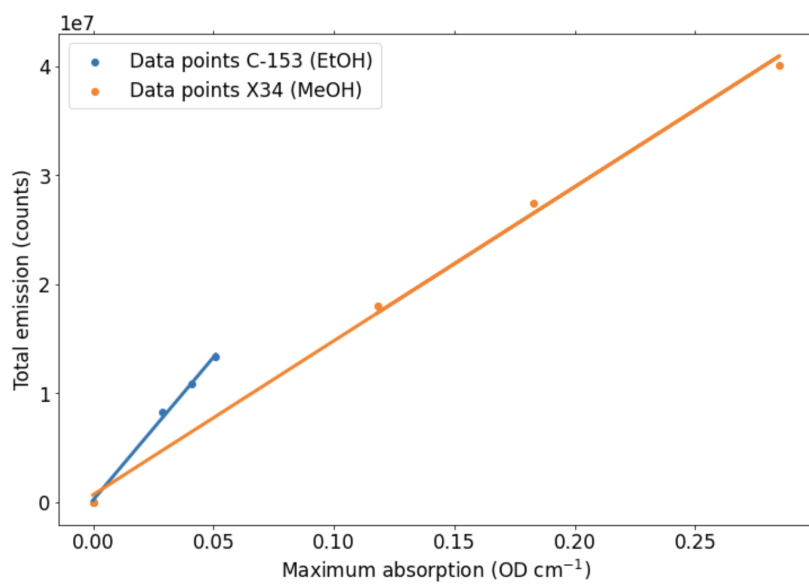


Figure B.2: Total emission plotted against maximum absorption for the three concentrations of C-153 in EtOH and X34 in MeOH, with linear fits in corresponding colors. ($r^2 = 0.9967$ for C-153, $r^2 = 0.9972$ for X34)

Appendix C

Additional lifetime decays from TCSPC

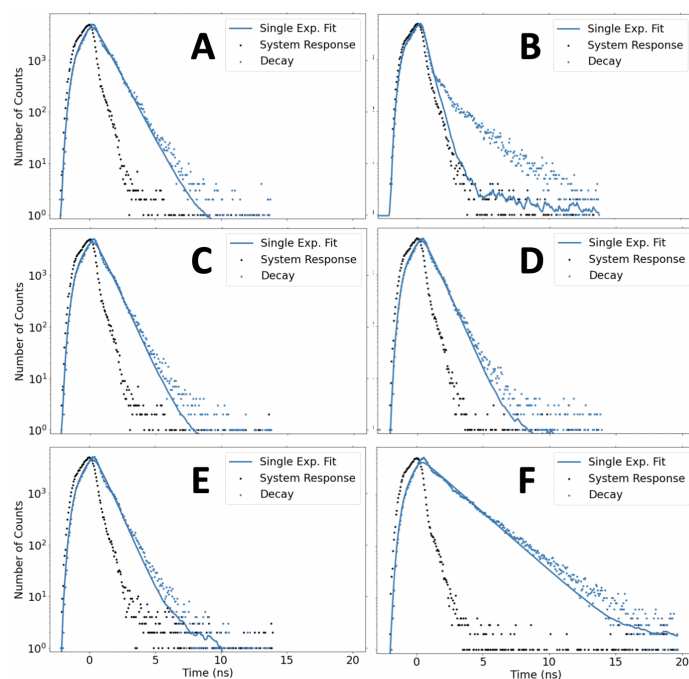


Figure C.1: Fluorescence lifetime decays of X34 in (A) DMSO, (B) PBS, (C) PrOH, (D) MeCN, (E) EtOH, and (F) THF. All decays were fitted to a single exponential equation. ($\lambda_{\text{ex}} = 373\text{nm}$, $\lambda_{\text{em}} = 432\text{nm}$)

Fluorescence lifetime decays of X34 not included in the main text are displayed in figure C.1. THF gives X34 a much longer lifetime than the other solvents. All decays have been well fitted to a single exponential equation, except for X34 in PBS, which is likely to fit better to a double exponential equation.

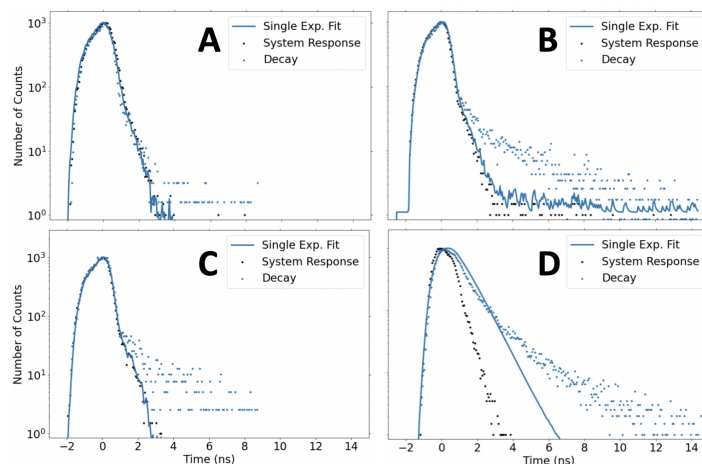


Figure C.2: Fluorescence lifetime decays of HS335 in (A) CHCl_3 , (B) DMSO, (C) MeOH, and (D) PBS. All decays were fitted to a single exponential equation. ($\lambda_{\text{ex}} = 373\text{nm}$, $\lambda_{\text{em}} = 500\text{nm}$ for all solvents, except PBS with $\lambda_{\text{ex}} = 455\text{nm}$, $\lambda_{\text{em}} = 550\text{nm}$.)

Fluorescence lifetime decays of HS335 are shown in figure C.2. Except for in PBS, the lifetimes are all much shorter than the lifetimes of X34 and below the instrument limit of 100 ns. The lifetimes of HS335 in DMSO and PBS could likely be more accurately fitted to a double exponential equation.

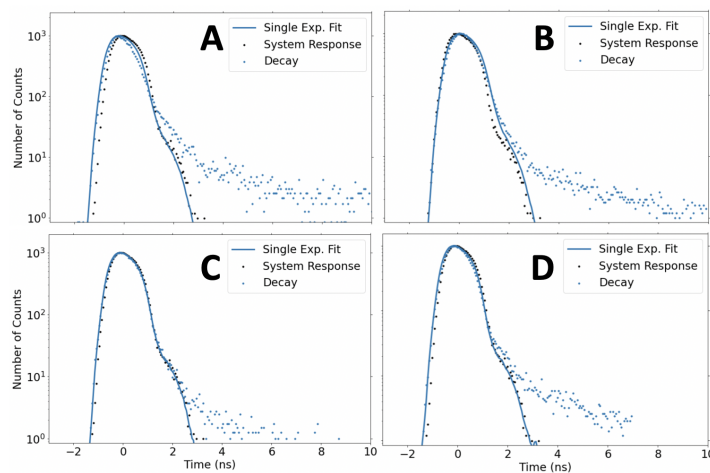


Figure C.3: Fluorescence lifetime decays of HS336 in (A) CHCl_3 , (B) DMSO, (C) MeOH, and (D) PBS. All decays were fitted to a single exponential equation. ($\lambda_{\text{ex}} = 455\text{nm}$, $\lambda_{\text{em}} = 600\text{nm}$)

Fluorescence lifetime decays of HS336 are presented in figure C.3. The lifetimes are all much shorter than the lifetimes of X34 and very close to the instrument limit of 100 ns.

Appendix D

Deciding Regions of Interest (ROI) for CLSM and FLIM

For both CLSM and FLIM image acquisition, deciding on suitable regions of interest (ROIs) proved to be difficult. ROIs were used both when collecting emission spectra of the ligands in cells, and when measuring the fluorescence lifetime. A CLSM image with two different ROIs and their corresponding emission spectra are displayed in figure D.1. (SH-SY5Y, 7 μ M X34, 7 μ M ATTR, 36h incubation) Two ROIs are highlighted, a diffuse area (green) and a more highly fluorescent area (red). These were common elements in most of the CLSM images, with the diffuse areas often being found outside of or between the cells and the highly fluorescent artifacts inside the cells. Both could potentially be fibril structures.

A FLIM image of the same sample with two different ROIs, a diffuse area (green) and an ambiguous artifact (red), as well as the lifetime decays and fitted decays of the respective ROIs are shown in figure D.2. There was a significant difference in the lifetimes measured for these ROIs, at $1000\text{ps} \pm 15$ and $690\text{ps} \pm 16$, respectively.

Both the CLSM and FLIM examples show the impact the choice of ROI has on the obtained results. Unless otherwise specified, the emission intensity scans and fluorescence lifetime decays in cells found in this thesis were measured from an ROI of a whole, single cell. For cells with many different structures, particularly seen for the SH-SY5Y cells with several of the ligands, different ROIs were often chosen for comparison and will be specified with the results.

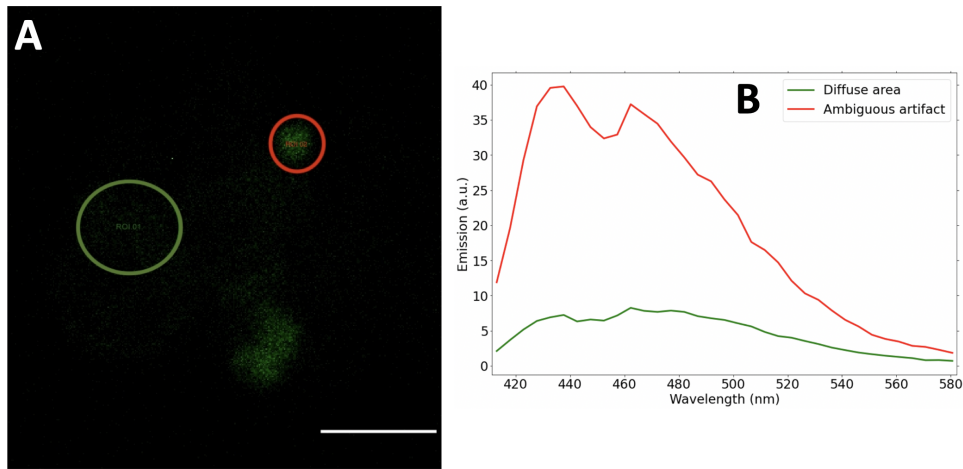


Figure D.1: (A) CLSM image of SH-SY5Y cells with two defined ROIs, a highly fluorescent ambiguous artifact (red) and a more diffusely fluorescent area (red), and (B) emission intensity from the ROIs in corresponding colors. The cells were incubated with ATTR (7 μ M) and X34 (7 μ M) for 36 h, and also stained using DRAQ5 (10 μ M). The emission intensity of the ambiguous artifact is much higher than the diffuse area. Scale bar is 7.5 μ M.

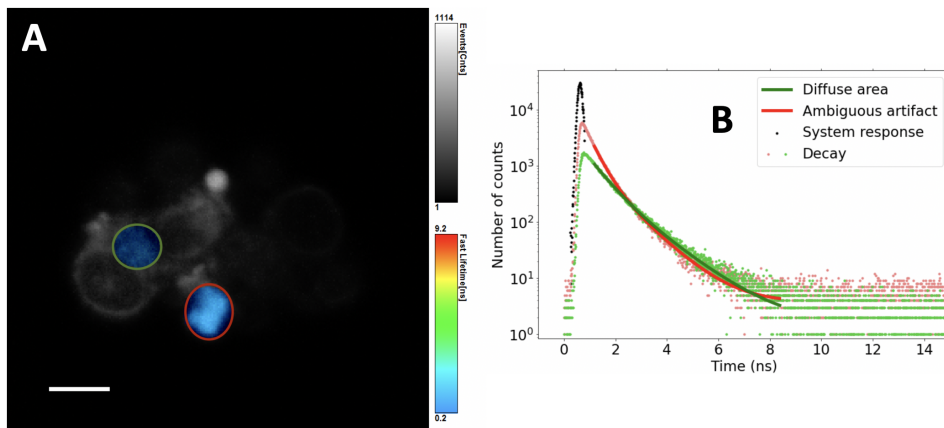
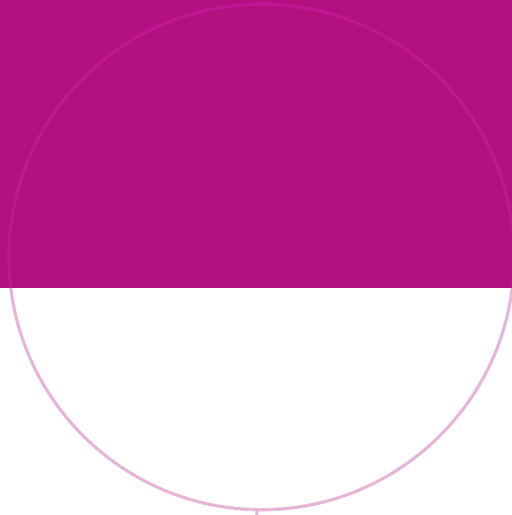


Figure D.2: (A) FLIM image of SH-SY5Y cells, showing two chosen ROIs; a diffuse area (green) and an ambiguous artifact (red), and (B) decays and double exponential fits for the two ROIs in corresponding colors. The cells were incubated with X34 (7 μ M) and ATTR (7 μ M) for 36 h, and stained with DRAQ5 (10 μ M). Scale bar is 8 μ M. See text for details.



Norwegian University of
Science and Technology